論文 / 著書情報
Article / Book Information

題目(和文)	
Title(English)	Metallization and Functionalization of Flexible Silk Textile by Supercritical CO2 Promoted Electrochemical Techniques
著者(和文)	Chiu Wan-Ting
Author(English)	Wan-Ting Chiu
出典(和文)	学位:博士(工学), 学位授与機関:東京工業大学, 報告番号:甲第10980号, 授与年月日:2018年9月20日, 学位の種別:課程博士, 審査員:曽根 正人,寺田 芳弘,木村 好里,細田 秀樹,三宮 工
Citation(English)	Degree:Doctor (Engineering), Conferring organization: Tokyo Institute of Technology, Report number:甲第10980号, Conferred date:2018/9/20, Degree Type:Course doctor, Examiner:,,,,
学位種別(和文)	博士論文
Type(English)	Doctoral Thesis

Metallization and Functionalization of Flexible Silk Textile by Supercritical CO_2 Promoted Electrochemical Techniques

Doctor of Engineering

Department of Materials Science and Engineering

Tokyo Institute of Technology

Wan–Ting Chiu

September, 2018

Table of content

Table of content

Table of content

Figure captions

Figure captions

Figure captions

Figure captions

Figure captions

Table captions

Chapter 1 General introduction

1.1 Wearable electronic and medical device applications

Wearable electronic devices and medical devices were predicted to blossoming in the near future [1, 2]. Wearable devices are the devices such as smart clothing and solar bag which integrate electronic devices or functional materials and textile together to facilitate the convenience of our daily life. Wearable medical devices are the gears that can detect or support out health condition such as biosensor patch and peace maker. Figure 1- 1 shows various applications of wearable electronic and medical devices. There are some wearable devices which are commercially available nowadays; however, most of the devices are composed of rigid materials. Even small annoyance can irritate the active users such as athlete. Therefore, a flexible, electronically conductive, and functional wearable devices are now urgently demanded. This study focused on the exploitation of the materials and the enhancement of reliabilities of the wearable devices.

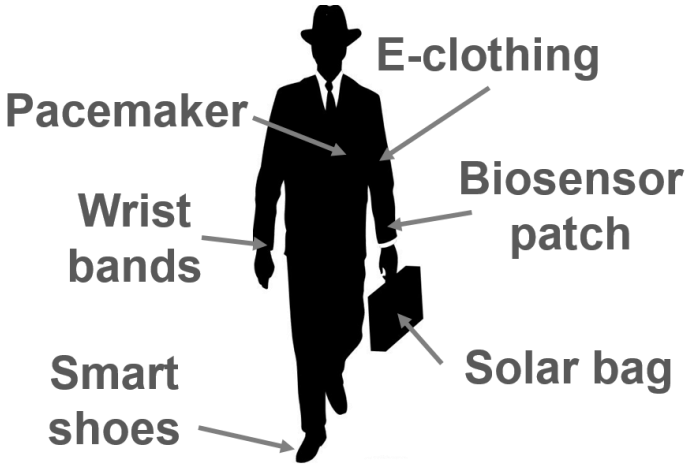

Figure 1- 1 Various applications of wearable devices

1.2 Methodology for the integration of materials for the applications

1.2.1 Electroless plating

Due to the demands of flexibility and electrical conductivity of wearable devices, combining the flexible and electrical conductive materials together are the greatest challenge. Electroless plating is a promising method to integrate these two instinct materials. Electroless plating is also known as chemical or autocatalytic plating [3]. Unlike conventional electroplating, no electrical current is required to carry out the deposition. It is a technique which can be accomplished by simple procedures and facile equipment. Processing temperature is relatively lower (<90 ^{o}C) than other deposition techniques. The greatest difference between electroless plating and immersion plating is whether it can be autocatalytic or not.

Electroless plating consists of three fundamental procedures, pretreatment is the first step for cleaning and roughening the substrate's surface, catalyzation is the second step to inlay the catalyst into the substrates, and deposition is the last step to deposit the materials on the substrate (Figure 1- 2). The basic component of deposition solution includes (1) metal ions (i.e. Ni, Pt, and Au ion complexes), (2) reducing agent (i.e. hydrazine, and hypophosphite), (3) complexing agent (i.e. ethylenediaminetetraacetic acid (EDTA)), and (4) bath stabilizer (i.e. tungstate, sulphate, nitrate and chloride). Complexing agent acts as buffer to help control pH and maintain control over the free metal salt ions available to the solution, thus allowing solution stability. Stabilizer acts as a catalytic inhibitor, retarding potential spontaneous decomposition of the deposition bath. The complexing agent and stabilizer determine the composition and brightness of the deposit. Excessive use of stabilization materials can result in a depletion of plating rate and bath life including poor metallurgical deposit properties. In the deposition step, the

deposition properties can be controlled by many parameters such as (1) deposition temperature, (2) solution pH, (3) metal ion concentration, and (4) reducing agent concentration in the bath. Table 1- 1 show the typical plating bath components and operating parameters [4].

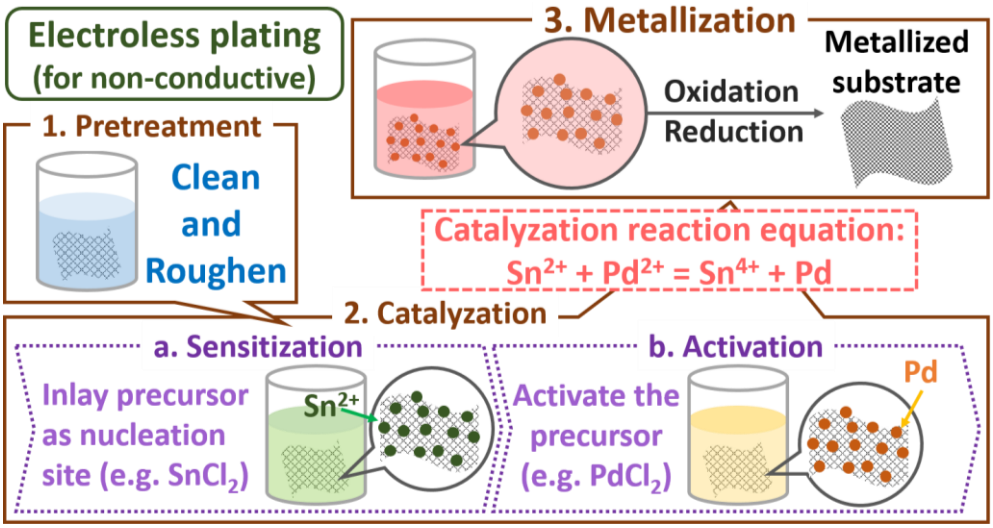

Figure 1- 2 Electroless plating procedures for non–conductive substrates

It is widely accepted that electroless plating proceeds along the electrochemical mechanism as the simultaneous reaction of cathodic metal deposition and anodic oxidation of reductant [5]. The electrochemical conditions for electroless plating taking place are, first, the oxidation potential of the reductant's being less noble to the reversible potential of the metal to be deposited. This would be the thermodynamic consideration. Second, the metal is having enough catalytic activity for the anodic oxidation take place with reasonable rate. While, this responses to the requirement of kinetics.

A reductant used in electroless plating have a special feature. A limited variety of reductants is used in an electroless plating, i.e. hypophosphite, formaldehyde, borohydride, dialkylamine borane, and hydrazine, which have been also shown in Table

1- 1. Electroless plating usually accompanies hydrogen evolution, the rate of which is not directly related to that of metal deposition. It was found that the hydrogen evolved during electroless plating was originated mainly from the reducing agent [6, 7]. Electroless plating proceeds mostly on certain metals that are known to be hydrogenation–dehydrogenation catalysts (i.e. Pt, Pd, and Ni). It was reported that the position for hydrogenation catalysts such as thioura and mercaptobenzothiazole functions as stabilizer in an electroless plating solution [8]. Usually the kinetic requirement is that the catalyst has the ability to dissociate chemisorption to form adsorbed atomic hydrogen and an adsorbed anion radical. It is also proposed that the catalytic aspect in electroless plating is originated from the catalytic property of the metal for of the metal [9].

Table 1- 1 Typical electroless plating bath components and operating parameters [4]

Electroless Bath	*Temperature*	*pH*	*Deposition Rate/hr*	*Metal Salt(s)*	*Reducing Agent(s)*	*Complexing Agent(s) or Chelators*	*Stabilizer(s)*	*pH Adjustment*
Acid nickel	77–93°C (170–200°F)	4.4–5.2 (medium P) (high P) 6 0–6.5 (low P)	12.7–25 4 μm (0.5–1 mil)	Nickel sulfate Nickel chloride	Sodium hypophosphite Sodium borohydride Dimethylamine borane (DMAB)	Citric acid Sodium citrate Succinic acid Proprionic acid Glycolic acid Sodium acetate	Fluoride compounds Heavy metal salts Thiourea Thioorganic compounds (i.e., 2-mercaptobenzothiazole, MBT) Oxy anions (i e., iodates)	Ammonium hydroxide Sulfuric acid
Alkaline nickel	26–95°C (79–205°F)	8.5–14.0	10–12.7 μm (0.4–0.5 mil)	Nickel sulfate Nickel chloride	Sodium borohydride Sodium hypophosphite DMAB Hydrazine	Citric acid Sodium citrate Lactic acid Glycolic acid Sodium acetate Sodium pyrophosphate	Thiourea Heavy metal salts Thioorganic compounds Triethanolamine Thallium salts Selenium salts	Ammonium hydroxide Sulfuric acid Sodium hydroxide
Copper	26–70°C (79–158°F)	9.0–13.0	1.7–5 μm (0.04–0.3 mil)	Copper sulfate Copper acetate Copper carbonate Copper formate Copper nitrate	Formate Formaldehyde DMAB Sodium hypophosphite	Rochelle salt EDTA Ammonium hydroxide Pyridium-3-sulfonic acid Potassium tartrate Quadrol	Thiodiglycolic MBT Thiourea Sodium cyanide Vanadium pentoxide Potassium ferrocyanide	Hydrochloric acid Sulfuric acid Sodium hydroxide Potassium hydroxide
Gold	65–88°C (149–190°F)	10.0–13.0	2–5 μm (0.08–0.2 mil)	Gold cyanide Gold chloride Potassium aurate	DMAB Sodium hypophosphite Potassium borohydride Potassium cyanoborohydride	Sodium phosphate Potassium citrate Sodium borate Potassium tartrate EDTA	Alkali metal cyanide Alkali hydrogen fluoride Acetylacetone	Potassium hydroxide Phosphoric acid Sulfuric acid
Palladium	45–73°C (113–165°F)	8.0–12.0	2–5 μm (0 08–0.2 mil)	Palladium chloride Palladium bromide	Sodium hypophosphite DMAB Triethylamine borane	Ammonia Methylamine EDTA	Thioorganic compounds Organic cyanides Thiourea Thiocyanates	Ammonium hydroxide Hydrochloric acid
Cobalt	85–95°C (185–203°F)	9.0–11.0	2.5–10 μm (0 1–0.4 mil)	Cobalt chloride Cobalt sulfate	DMAB Sodium hypophosphite	Sodium citrate Citric acid Ammonium chloride Succinic acid	Urea Thioorganic compounds	Ammonium hydroxide Sodium hydroxide

As mentioned in the previous paragraph, the second step of electroless plating is catalyzation, which is a critical step for the metallization. Whether metallization can

happen spontaneously depends on both thermo–dynamic and kinetic. The first fundamental requirement is thermal dynamic (eq. (1. 1))

$$\Delta \boldsymbol{G} = -\boldsymbol{n} \times \boldsymbol{F} \times \Delta \boldsymbol{U_{eq}} = -\boldsymbol{n} \times \boldsymbol{F} \times \left(\boldsymbol{V_{M/M^{+}}} - \boldsymbol{V_{Re/Re^{*}}}\right) = -\boldsymbol{n} \times \boldsymbol{F} \times \Delta \boldsymbol{V} \qquad (1.\ 1)$$

Where ΔG is Gibbs free energy change per mole of reaction, n is number of moles of electrons transferred in the reaction, F is Faraday constant = 96485 C/mol (charge per mole of electrons), V is reduction potential of each species, M is metal, M^{+} is metal ion, Re is reducing agent, and Re* is oxidized reducing agent. Reactions happen spontaneously when ΔG is negative (ΔG < 0). Thus, negative ΔV (ΔV < 0) is a critical requirement of a spontaneous reaction. An example is shown in the following:

$$Ni^{2+} + 2e^{-} = Ni \ldots V_{Ni^{2+}/Ni} \qquad (1.\ 2)$$

$$Re = Re^{2+} + 2e^{-} \ldots V_{Re/Re^{2+}} \qquad (1.\ 3)$$

Total reaction:

$$Ni^{2+} + Re = Ni + Re^{2+} \ldots \Delta V \qquad (1.\ 4)$$

Where ε_{total}:

$$\Delta V = V_{Ni^{2+}/Ni} + V_{Re/Re^{2+}} \qquad (1.\ 5)$$

While ΔV < 0 is a requirement for the spontaneous reaction, $V_{Ni^{2+}/Ni} + V_{Re/Re^{2+}}$ should be negative. Thus, the math relationship of $V_{Ni^{2+}/Ni} < -V_{Re/Re^{2+}}$ is established. Or the equation can be written as $V_{Ni^{2+}/Ni} < V_{Re^{2+}/Re}$. In the chemical aspect of view, it means Ni^{2+} has higher ability to get the electrons than reducing agent. Therefore, Ni^{2+} is reduced and reducing agent is oxidized in the solution. This is in accordance with the statement that have been mentioned in the previous paragraph. This is the basic requirement in the view of thermodynamics. The requirement of kinetics will be discussed in the next paragraph.

Most of the literature claim that whether the catalyst is a proper catalyst for the deposition system depends on the nature of the catalyst. To be specific, as mentioned previously, deposition proceeds mostly on certain metals that are known to be hydrogenation–dehydrogenation catalysts (i.e. Pt, Pd, and Ni). Whether the catalyst can go on hydrogenation–dehydrogenation reaction or not is one of the kinetic requirements. It has been reported that hydrogenation–dehydrogenation is the first and crucial step to start the deposition [10, 11]. Without dehydrogenation reducing agents do provide electrons to metal ions in the solution. The mechanisms of different reducing agents are shown in Table 1- 2 [11]. The catalytic of various metals are shown in Figure 1- 3 [10].

Table 1- 2 Mechanism of catalyst works on various reducing agents [11]

	BOROHYDRIDE	DIALKYLAMINE BORANE	HYDRAZINE	FORMALDEHYDE	HYPOPHOSPHITE
1	$BH_4^- \xrightarrow{M} \dot{B}H_3^- + \dot{H}$				
2	$\dot{B}H_3^- + OH^- \longrightarrow BH_3OH^- + e$				
1	$BH_3OH^- \xrightarrow{M} \dot{B}H_2OH^- + \dot{H}$	$R_2NHBH_3 + OH^- \xrightarrow{M} R_2NH + \dot{B}H_2OH^- + \dot{H}$			
2	$\dot{B}H_2OH^- + OH^- \longrightarrow BH_2(OH)_2^- + e$	$\dot{B}H_2OH^- + OH^- \longrightarrow BH_2(OH)_2^- + e$			
1	$BH_2(OH)_2^- \xrightarrow{M} \dot{B}H(OH)_2^- + \dot{H}$	$BH_2(OH)_2^- \xrightarrow{M} \dot{B}H(OH)_2^- + \dot{H}$	$N_2H_4 \xrightarrow{M} \dot{N}_2H_3 + \dot{H}$		
2	$\dot{B}H(OH)_2^- + OH^- \longrightarrow BH(OH)_3^- + e$	$\dot{B}H(OH)_2^- + OH^- \longrightarrow BH(OH)_3^- + e$	$\dot{N}_2H_3 + OH^- \longrightarrow N_2H_3OH + e$		
				$HCHO + H_2O \rightleftharpoons CH_2(OH)_2$	
				$CH_2(OH)_2 + OH^- \rightleftharpoons CH_2OHO^- + H_2O$	
1	$BH(OH)_3^- \xrightarrow{M} \dot{B}(OH)_3^- + \dot{H}$	$BH(OH)_3^- \xrightarrow{M} \dot{B}(OH)_3^- + \dot{H}$	$N_2H_3OH \xrightarrow{M} \dot{N}_2H_2OH + \dot{H}$	$CH_2OHO^- \xrightarrow{M} \dot{C}HOHO^- + \dot{H}$	$H_2PO_2^- \xrightarrow{M} H\dot{P}O_2^- + \dot{H}$
2	$\dot{B}(OH)_3^- + OH^- \longrightarrow B(OH)_4^- + e$ $\Downarrow$ $BO_2^- + 2H_2O$	$\dot{B}(OH)_3^- + OH^- \longrightarrow B(OH)_4^- + e$ $\Downarrow$ $BO_2^- + 2H_2O$	$\dot{N}_2H_2OH + OH^- \longrightarrow N_2H_2(OH)_2^- + e$ $\downarrow$ $N_2\uparrow + 2H_2O$	$\dot{C}HOHO^- + OH^- \longrightarrow CH(OH)_2O^- + e$ $\downarrow$ $HCOO^- + H_2O$	$H\dot{P}O_2^- + OH^- \longrightarrow H_2PO_3^- + e$
3	$\dot{H} + \dot{H} \longrightarrow H_2\uparrow$				
4	$\dot{H} + OH^- \longrightarrow H_2O + e$				
1+2+3	$BH_4^- + 4OH^- \longrightarrow BO_2^- + 2H_2O + 2H_2\uparrow + 4e$	$2R_2NHBH_3 + 8OH^- \longrightarrow 2R_2NH + 2BO_2^- + 4H_2O + 3H_2\uparrow + 6e$	$N_2H_4 + 2OH^- \longrightarrow N_2\uparrow + 2H_2O + H_2\uparrow + 2e$	$2HCHO + 4OH^- \longrightarrow 2HCOO^- + 2H_2O + H_2\uparrow + 2e$	$2H_2PO_2^- + 2OH^- \longrightarrow 2H_2PO_3^- + H_2\uparrow + 2e$
1+2+4	$BH_4^- + 8OH^- \longrightarrow BO_2^- + 6H_2O + 8e$	$R_2NHBH_3 + 7OH^- \longrightarrow R_2NH + BO_2^- + 5H_2O + 6e$	$N_2H_4 + 4OH^- \longrightarrow N_2\uparrow + 4H_2O + 4e$	$HCHO + 3OH^- \longrightarrow HCOO^- + 2H_2O + 2e$	$H_2PO_2^- + 2OH^- \longrightarrow H_2PO_3^- + H_2O + 2e$

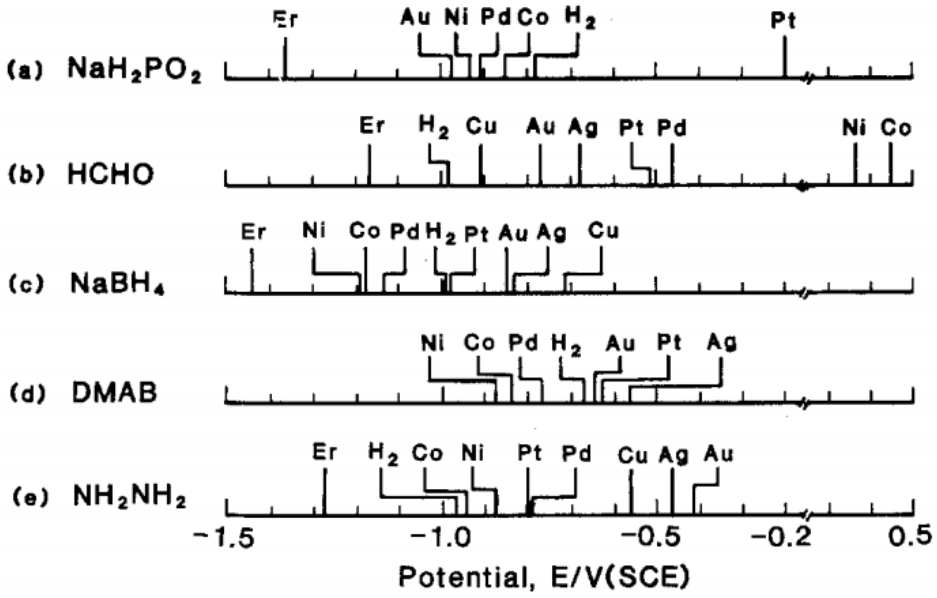

Figure 1- 3 Catalytic activity of various metals (active sites) in different reducing agent solution: (a)NaH_2PO_2, (b) HCHO, (c) $NaBH_4$, (d) DMAB, and (e) NH_2NH_2 [10]

Since electroless plating is less limited by the experimental apparatus, the substrate can be non–electrical conductive and the shape of the substrate can be sophisticated. Electroless plating provides a deposit that follows all contours of the substrate exactly, without building up at the edges and corners. A sharp edge receives the same thickness of deposit as dose a blind hole. The advantages of electroless plating makes the integration of textile and conductive material applicable. This study thus combined these two distinct materials by electroless plating to fulfill the applications of wearable devices.

1.2.2 Supercritical carbon dioxide promoted method

1.2.2.1 Supercritical carbon dioxide promoted catalyzation

Supercritical carbon dioxide (sc–CO_2) was introduced into the electroless plating in this study for enhancing the characters of electroless plating. In the conventional (CONV) catalyzation, $SnCl_2$ and $PdCl_2$ solutions were used as catalyzation solutions for inlaying

Pd metals on the substrate [12-14]. By the treatments of immersion into $SnCl_2$ followed by $PdCl_2$ solutions, the following reaction takes place:

$$\boldsymbol{Sn^{2+} + Pd^{2+} = Sn^{4+} + Pd} \quad (1.\ 6)$$

Pd metal can act as a catalyst in the next deposition step to activate the chemical reaction. However, $SnCl_2$ and $PdCl_2$ are dissolved into HCl solvent, which is strongly acidic solution. Textile substrate has high risk to be damaged by the CONV catalyzation [15]. In addition, Pd catalysts are only inlaid on the substrate surface and finally leads to poor adhesion between textile substrate and conductive material layer.

Sc–CO_2 was introduced into the catalyzation step to solve the CONV problems [16]. Carbon dioxide (CO_2) turns into sc–CO_2 when the pressure and temperature go beyond its critical point (304 K and 7.4 MPa) [17, 18] (Figure 1- 4). Sc–CO_2 owns the properties between liquid and gas phases showing low viscosity, low surface tension, high self–diffusivity, non–erosive to most of the polymers, and non–polarity [19]. Due to the aforementioned advantages, sc–CO_2 can bring catalyst into the substrate since textile has the affinity to non–polarity materials (Figure 1- 5). Materials in the following deposition step can be deposited into the substrate showing the anchoring effect [20, 21] and enhance the adhesive property between substrate and deposited material. In addition, due to the properties of low viscosity and non–erosive to most of the polymers, textile remains undamaged after the sc–CO_2 catalyzation treatment. Moreover, chemical solutions can be completely excluded in the sc–CO_2 catalyzation, which can leads to environmental friendly process. This study introduced sc–CO_2 into the catalyzation step to solve the traditional difficulties and enhance the adhesive property between textile substrate and deposited materials.

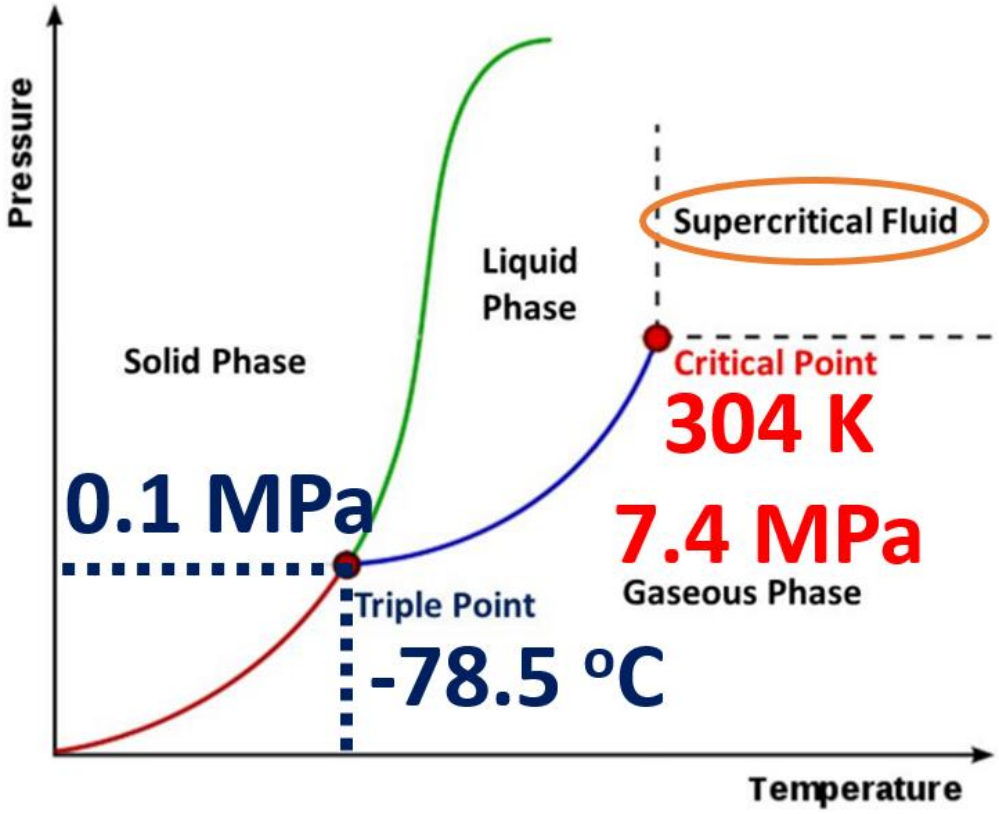

Figure 1- 4 Pressure–Temperature phase diagram of carbon dioxide

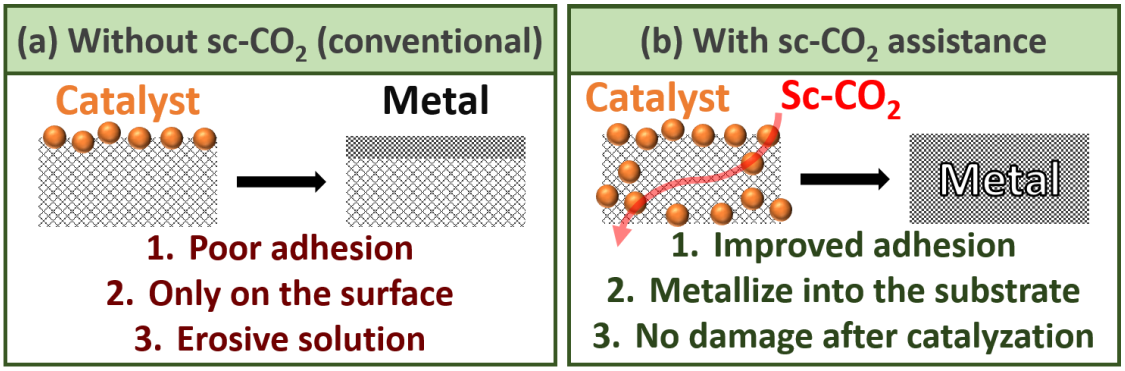

Figure 1- 5 Comparison between (a) CONV catalyzation (without sc–CO_2) and (b) sc–CO_2 catalyzation and their characteristics

1.2.2.2 Supercritical carbon dioxide promoted metallization

Since metal was deposited on the textile substrate in this study, here we use the term of metallization for the last step of electroless plating instead of deposition. Sc–CO_2 was

not only introduced into catalyzation but also introduced into the metallization step to enhance the metallization properties. Hydrogen evolution takes place during most of the metallization steps, and the hydrogen bubbles leads to defects in the metallization layer and finally results in poor properties such as low electrical conductivity and low compactness of metallization layer. The introduction of sc–CO_2 can solve this difficulty, which is brought from the evolution of hydrogen. With accompany of surfactant, sc–CO_2 and surfactant form the micelles in the aqueous solution since one side of the surfactant is hydrophilic and the other side is hydrophobic [22]. Due to the aforementioned advantages of sc–CO_2 such as non–polarity and high self–diffusivity, it can dissolves hydrogen bubbles and take hydrogen bubbles away from the substrate surface. This finally results in defect–free metallization layer. The comparison between CONV metallization and sc–CO_2 metallization was shown in Figure 1- 6. This study introduced sc–CO_2 into the metallization step to enhance the properties of metallization layer.

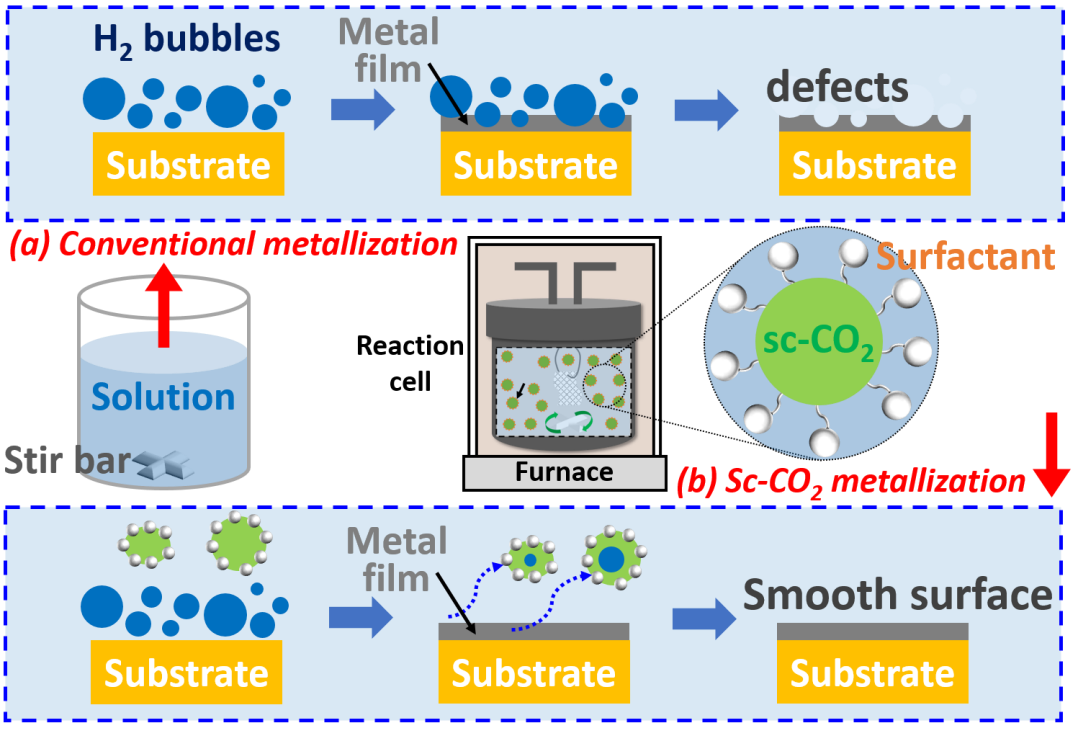

Figure 1- 6 Comparison between CONV metallization and sc–CO_2 metallization

1.2.3 Cathodic deposition

Wearable devises are not only limited in electronic devices but also has been diversified into many applications such as combining photocatalyst into the composite material. There are various synthetic methods to deposit photocatalytic metal oxides, which include high–temperature vapor deposition [23], polymer–mediated chemical reaction [24], hydrothermal–annealing process [25], and one–pot solution–based methods [26]. Cathodic deposition was used in this study due to its advantages such as relatively low operation temperature (<90 ºC), simple operation procedures, low cost, unnecessary of evacuation system. In addition, patterning of the deposition can be carried out in the cathodic deposition while combing with lithography.

Typical cathodic deposition apparatus consist three electrodes (constant voltage method), which are working electrode, counter electrode, and reference electrode. However, two electrode method (constant current method) is widely used in industry due to its simplicity. A two electrode cathodic deposition was thus used in this study to fabricate the metal oxide (i.e. ZnO) on the metallized textile (Figure 1- 7).

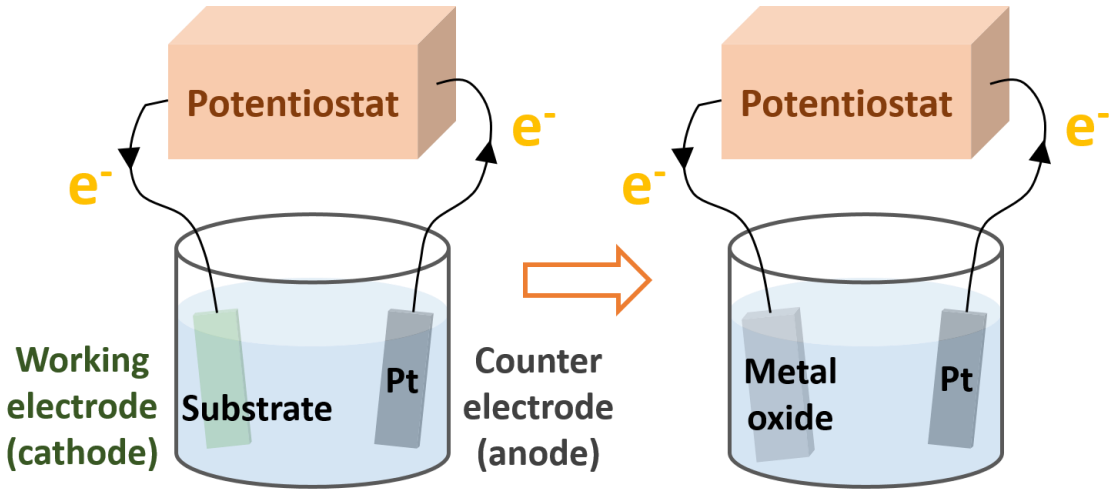

Figure 1- 7 Equipment setting of two electrode cathodic deposition

1.3 Integration of textile, electrically conductive materials, and functional materials

In the materials point of view, flexibility, electrical conductivity, biocompatibility, and stitchability are basic requirements. It also should be a common cloth material. Based on the aforementioned requirements, silk textile was chosen in this study to fulfill the requirements of flexibility, biocompatibility, and stitchability. In addition, silk is a common cloth material. On the other hand, Ni–P, Pt, and Au were chosen as the metallization layer for achieving electrical conductivity. Ni–P was chosen for its low cost, suitable electrical conductivity, and high corrosion resistance. Pt and Au were further chosen due to the biocompatibility and high electrical conductivity. In the function point of view, ZnO was chosen for the functionality, ZnO plays a role of photocatalyst in the wearable devices. In addition, ZnO is also biocompatible material. Figure 1- 8 shows the summary of the materials.

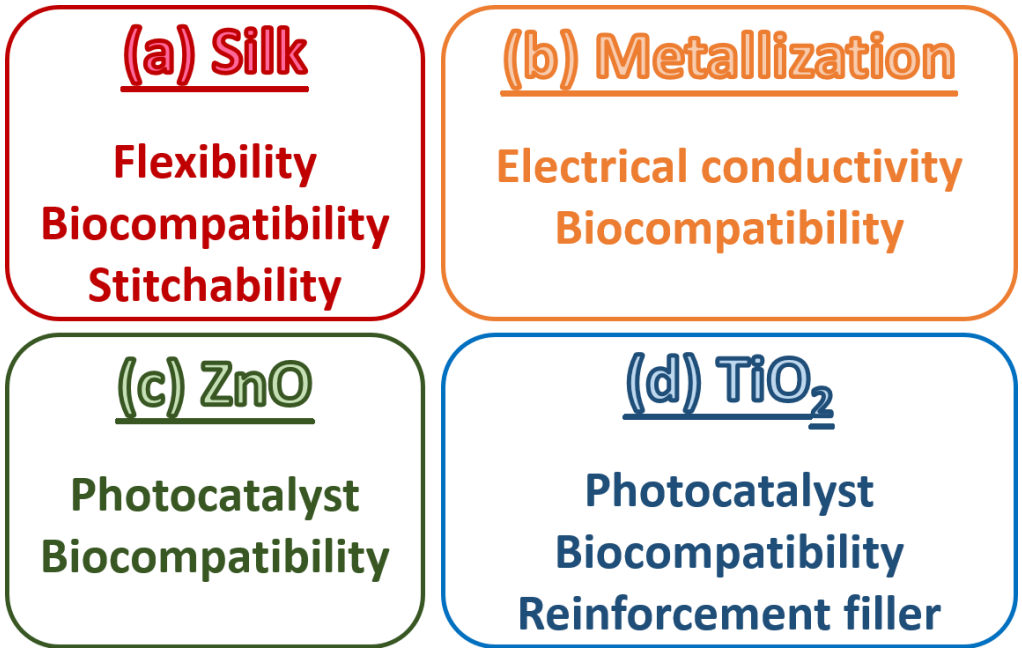

Figure 1- 8 Summary of the advantages and reasons of the chosen materials: (a) silk, (b) Metallization layer, (c) ZnO, and (d) TiO_2

1.3.1 Metal thin film on silk textile

1.3.1.1 Ni–P metallization

Catalytic surface is basic requirement for the metallization, in other word, metallization only occurs on specific surfaces. Almost all metals of Group VIII (Fe, Co, Ni, Rh, Pd, and Pt) is active for the reduction reaction. These metal are well known as hydrogenation–dehydrogenation catalyst. On the other hand, those metals, which are more electropositive than Ni such as Al, are replaced by Ni firstly and Ni acts as an active catalyst afterward (eq. (1. 7)).

$$2Al + 3Ni^{2+} = 2Al^{3+} + 3Ni \quad (1.\ 7)$$

The very first step in the Al substrate is the displacement and the substrate shows catalytic property after the displacement.

The most widely used engineering form of electroless plating is, by far, electroless nickel plating [27]. Electroless nickel plating offers unique deposit properties including uniformity of deposition in deep recesses, bores, and blind holes. Most commercial deposition is done with an acid phosphorus bath owing to its unique physical characteristics, including excellent corrosion, wear, and abrasion resistance, ductility, lubricity, solderability, electrical properties, and high hardness. The chemical reducing agent most commonly used is sodium hypophosphite (NaH_2PO_2), sodium borohydride ($NaBH_4$), or aminoborane such as n–dimethylamine borane (DMBA; $(CH_3)_2NHBH_3$).

Acid nickel–phosphorus deposits normally consist of 87–94% Ni and 6–13% P, operating at 77–93 ºC with a pH of 4.4–5.2. Low phosphorus electroless Ni baths contain 1–3% P and normally operate at 80–82 ºC with a pH of 6.0–6.5. According to the concentration of P in the Ni–P deposition, it can be classified into three classifications. 1–

3%P is low phosphorus, 6–10%P is medium phosphorus, and 11–13%P is high phosphorus. The pH of the solution is the controlling factor affecting the phosphorus content of the deposit. The higher the pH, the lower the phosphorus content, resulting in deposit property changes. Lower phosphorus containing deposits typically have less corrosion resistance than 10% alloys. Deposits containing phosphorus in excess of 8% are typically nonmagnetic.

The reducing agent is commonly NaH_2PO_2. Nickel deposition by hypophosphite was firstly thought to be the following equations:

$$Ni^{2+} + H_2PO_2^- + H_2O = Ni + H_2PO_3^- + 2H^+ \quad (1.\ 8)$$

$$H_2PO_2^- + H_2O \xrightarrow{cat} H_2PO_3^- + H_2 \quad (1.\ 9)$$

Overall:

$$Ni^{2+} + 2H_2PO_2^- + 2H_2O = Ni + 2H_2PO_3^- + 2H^+ + H_2 \quad (1.\ 10)$$

However, eq. (1. 8), (1. 9), and (1. 10) failed to account for the co–deposition of Ni and phosphorus. More mechanisms, which will be shown in the following, were proposed after the discovering of the Ni–P chemical metallization.

(1) Atomic hydrogen mechanism

Brenner and Riddell [28, 29] proposed the first mechanism of Ni–P metallization. They postulated that the actual Ni reductant is atomic hydrogen which is generated by the reaction of water with hypophosphite:

$$H_2PO_2^- + H_2O = H_2PO_3^- + 2H_{ad} \quad (1.\ 11)$$

$$Ni^{2+} + 2H_{ad} \rightarrow Ni + 2H^+ \quad (1.\ 12)$$

The evolution of H_2 gas, which always accompanies Ni–P metallization, was due to the

recombination of two hydrogen atoms.

$$2H_{ad} \rightarrow H_2 \quad (1.\ 13)$$

However, atomic hydrogen mechanism failed to account for the simultaneous reduction of Ni and H_2, nor does it explain why the stoichiometric utilization of hypophosphite is always less than 50%.

(2) Hydride transfer mechanism

Hersch [30] is the first one proposed the hydride transfer mechanism.

In acidic solution:

$$2H_2PO_2^- + 2H_2O \xrightarrow{\text{cat}} 2H_2PO_3^- + 2H^+ + 2H^- \quad (1.\ 14)$$

In alkaline solution:

$$2H_2PO_2^- + 2OH^- \xrightarrow{\text{cat}} 2H_2PO_3^- + 2H^- \quad (1.\ 15)$$

The reduction of nickel ion in this mechanism proceeds as follows:

$$Ni^{2+} + 2H^- \rightarrow Ni + H_2 \quad (1.\ 16)$$

Phosphorus co–deposition can be explain by:

$$H_2PO_2^- + H = P + OH^- + H_2O \quad (1.\ 17)$$

The hydride transfer mechanism presents a satisfactory explanation for the coupled reduction of Ni and H_2.

(3) Electrochemical mechanism

This mechanism was firstly proposed by Brenner and Riddell and modified by others afterward.

$$H_2PO_2^- + H_2O = H_2PO_3^- + 2H^+ + 2e^- \quad (1.\ 18)$$

$$Ni^{2+} + 2e^- \rightarrow Ni \quad (1.\ 19)$$

$$2H^+ + 2e^- \rightarrow H_2 \quad (1.\ 20)$$

$$H_2PO_2^- + 2H^+ + e^- = P + 2H_2O \quad (1.\ 21)$$

According to the above equations, Ni ion should have a significant effect on the rate of reduction; however, it is widely known that the rate has a zero order dependence on Ni ion concentration.

(4) Coordination of hydroxyl ions

This mechanism was proposed by Cavallotti and Salvago [31, 32] and was supported by Radin and Hintermann [33]. Ni firstly acts as a catalyst and results in the ionization of water:

$$H_2O \xrightarrow{cat} H^+ + OH^- \quad (1.\ 22)$$

$$Ni(H_2O)_6^{2+} + 2OH^- = (OH) - Ni_{aq} - (OH) + 6H_2O \quad (1.\ 23)$$

$$(OH) - Ni_{aq} - (OH) + H_2PO_2^- = NiOH_{ads} + H_2PO_3^- + H \quad (1.\ 24)$$

$$NiOH_{ads} + H_2PO_2^- = Ni + H_2PO_3^- + H \quad (1.\ 25)$$

Where $NiOH_{ads}$ represents a hydrolyzed Ni^+ species adsorbed at the catalytic surface. The two hydrogen atoms can react and evolve as hydrogen gas:

$$H + H = H_2 \quad (1.\ 26)$$

The direct interaction of the catalytic Ni surface with $H_2PO_2^-$ to give P co–deposition:

$$Ni_{cat} + H_2PO_2^- = P + NiOH_{ad} + OH^- \quad (1.\ 27)$$

The hydrolyzed Ni can react with water as follow:

$$NiOH_{ads} + H_2O = [Ni(OH)_2]_{aq} + H \quad (1.\ 28)$$

Eq. (1. 25) and (1. 28) are seen to be competing reactions.

The reaction of hypophosphite ions with water must be included in the reaction scheme:

$$H_2PO_2^- + H_2O = H_2PO_3^- + H_2 \quad (1.\ 29)$$

Then the overall reaction would be:

$$Ni^{2+} + 4H_2PO_2^- + H_2O = Ni + 3H_2PO_3^- + H^+ + P + 3/2H_2 \quad (1.\ 30)$$

The mole ratio $[Ni^{2+}]/[H_2PO_2^-]$ in eq. (1. 30) is observed to be 0.25.

1.3.1.2 Pt metallization

On the contrary of Ni–P electroless plating, it is known that the greatest challenge of Pt electoless plating is to control the deposition [34-36]. Therefore, there are only limited literature concerning the Pt electroless plating [36, 37] . Since Pt owns the advantages such as high biocompatibility [38], high electrical conductivity [39], high corrosion resistance [40], and high thermal stability, Pt electroless was chosen in this study. Electroless Pt plating has been plated mostly using hydrazine (N_2H_4) or borohydride as the reducing agent. Among them, N_2H_4 is the most used reducing agent for Pt electroless plating since there are no co–deposition in the Pt metallization film. $(NH_3)_2Pt(NO_2)_2$ has been widely used as Pt ion source in the metallization solution. The reaction equation is shown in eq. (1. 31):

$$2(NH_3)_2Pt(NO_2)_2 + N_2H_4 \cdot H_2O = 2Pt + 5N_2 + 9H_2O \quad (1.\ 31)$$

1.3.1.3 Au metallization

Gold is currently irreplaceable for the electronics industry, in spite of its high price, because of its unique physical properties such as highly electrical conductivity [41], high corrosion resistance [42], and high thermal stability [43]. Although substitute materials such as Pd and its alloys are now being used in certain applications, it is believed that Au cannot be completely replaced by the other materials. In spite of the applicability of Au, the present state of development of electroless Au plating is still far from being

comparable to that of well–established methods of electroless Ni and Cu plating technique. The mostly used Au ion source is Potassium dicyanoaurate(I) ($KAu(CN)_2$) along with the reducing agent alkali metal borides (i.e. $NaBH_4$, and KBH_4) or an amine borane to make the metallization solution an autocatalytic bath [44]. Most commercially available electroless Au deposits are produced first by plating a thin deposit of immersion Au, followed by electroless Au plating. There are a few true autocatalytic Au processes available with 99.99% purity. Electroless Au can be successfully applied to Kovar, Ni, Ni alloys, Cu, Cu alloys, and metallized ceramics. Electroless Au can be deposited onto already present thin electrodeposited Au to give added strength [27]. The chemical reactions involved in the borohydride process are rather unique because the reducing agent that actually reacts with $Au(CN)_2^-$ is not BH_4^- itself but the species with the formula BH_3OH^-, which is an intermediate formed during the stepwise hydrolysis of BH_4^-:

$$BH_4^- + H_2O = BH_3OH^- + H_2 \quad (1.32)$$

$$BH_3OH^- + H_2O = BO_2^- + 3H_2 \quad (1.33)$$

$$6Au(CN)_2^- + BH_3OH^- + 6OH^- = 6Au + BO_2^- + 12CN^- + 5H_2O \quad (1.34)$$

All hydrogen gas produced during the metallization results from the hydrolysis reactions. The metallization in the bath was shown to be very low because of the second step of hydrolysis reaction proceed much more rapidly than the metallization reaction. Most of the borohydride is lost by hydrolysis. Electroless Au plating in the borohydride system takes place on noble metals (i.e. Pd, Rh, Ag, and Au itself). It also takes place on Cu, Ni, Co, Fe, and their alloys. Initial reactions on these two classes of metals are different. On noble metals the reaction is catalytic from the very beginning, on the other hand, the gold metallization on the other group is initiated by galvanic displacement.

Hydrazine is also a promising reducing agent in the Au metallization. The reactions take place on Ni substrate are shown in the following:

$$2Au(CN)_2^- + Ni = 2Au + Ni^{2+} + 4CN^- \quad (1.35)$$

$$RCOOH + N_2H_4 = RCONHNH_2 + H_2O \quad (1.36)$$

$$RCONHNH_2 + 2Au(CN)_2^- = 2Au + 4CN^- + N_2 + RCOH + 2H^+ \quad (1.37)$$

$$2Au(CN)_2^- + N_2H_5^+ + 2H_2O = 2Au + 2NH_3OH^+ + H^+ + 4CN^- \quad (1.38)$$

However, $KAu(CN)_2$ was gradually replaced by non–cyanide bath such as Au(III) chloride complex, due to its toxicity to human body. Au(III) chloride complex (i.e. $KAuCl_4$) is very easily reducible to Au metal along with the ether–substituted tertiary amine boranes reducing agent. This bath also shows autocatalytic property. On the other hand, Au(I) sulfite is also another choice for replacing toxic $KAu(CN)_2$ bath. This Au ion source is accompany with various reducing agents including hypophosphite, formaldehyde (HCHO), hydrazine, borohydride, and dimethylamine borane ($(CH_3)_2NH \cdot BH_3$). All the bath shows autocatalytic property. These baths, which are without cyanide species, even show better efficiency of Au metallization. Evidently, the catalytic activity of Au is poisoned by $Au(CN)^{2-}$ and/or CN^- ions. Using hydrazine borane is also a choice of the reducing agent for the cyanide–free baths. It is claimed that this bath containing hydrazine borane as a reducing agent can be operated under relatively low temperature (58–60 °C). For avoiding the toxic metallization bath, an Au(III) chloride complex metallization bath was used in this study.

1.3.2 Photocatalyst on metallized silk textile

Photocatalysis is a reaction of employing catalyst that is utilized for accelerating chemical reactions, which requires or engages light. A photocatalyst is defined as a

material that is able to absorb light, produce electron/hole pair (e^-/h^+), which facilitate chemical reactions of the reactants and regenerate its chemical composition after each cycle of such interactions [45-47]. There are two types of photocatalytic reactions (i.e. homogeneous and heterogeneous photocatalysis).

The crucial features of the photocatalyst are the appropriate band gap, suitable morphology, high surface area, stability and reusability [47, 48]. Metal oxides such as oxides of vanadium, chromium, titanium, zinc, tin, and cerium having these characteristics go through similar primary photocatalytic processes, which induces light absorption and an electron–hole pair separation process with the generation of positively charged holes that are able to oxidize reactants [47, 48]. In this process, a metal oxide is illuminated by either UV light, visible light, or a combination of both light sources, and photo–excited electrons are excited from the valence band to the conduction band, forming e^-/h^+. The photo–generated e^-/h^+ pair is capable of reducing and/or oxidizing a reactant adsorbed on the photocatalyst surface. The photocatalytic activity of metal oxide can be indicated by two sources in cathodic and anodic electrodes. The first one is the generation of OH radicals (OH•) by oxidation of OH^-, and the second one is the formation of O_2 radicals (O_2•) by reduction of O_2. The radicals can react with pollutants to degrade or transform them to less harmful products [48].

There are many catalysts reported in the literature for photocatalysis process. These metal oxides (TiO_2, ZnO, SnO_2 and CeO_2) have been widely used as photocatalysts, especially as heterogeneous photocatalyst [47, 49]. This is due to their biocompatibility, high stability in a variety of conditions, and capability to generate e^-/h^+ pairs when illuminated by enough amount of light source. The proper characteristics of electronic

configuration, light absorption properties, charge transport properties, and excited lifetimes of metal oxides has made it applicable for photocatalyst [45-48, 50].

Heterogeneous photocatalysis utilizing metal oxides such as TiO_2, ZnO, SnO_2 and, CeO_2 has proved its efficiency in degrading a wide range of pollutants into harmless CO_2 and water [51-56]. Many research has also indicated that metal oxides can be used as a photocatalyst, photovoltaics, preventing fogging of glass, and splitting water into hydrogen and oxygen [45-48]. Hence, they are of great interests in fields of environmental remediation, energy production and storage, and electronic industries [46-48]. Moreover, the heterogeneous photocatalysis has also been indicated as a promising self–cleaning, antibacterial, and deodorization system [46-48].

The physicochemical properties of the metal oxides are crucial for the performance of photocatalytic activity, which basically depends on size, shape, morphology, and composition [45-48]. The synthetic technique employed for the preparation of materials that can control the size, shape, composition, and morphology of the materials, which can contribute to the development of certain properties of the photoactive materials. This can facilitate the formation of metal oxides with the required characteristics that improve the performance of the photocatalytic activity [55, 57]. Cathodic deposition has been point out that it is able to control the morphology, size, and shape of metal oxide by tuning electrolyte and/or controlling the potential and current density. Thus cathodic deposition was chosen in this study for the formation of metal oxide and it is discussed in the 1.2.3 Cathodic deposition section.

1.3.2.1 ZnO Cathodic deposition

ZnO, which is a promising material for wearable devices, is a photocatalytic and

biocompatible material. There are many synthesis technique that have been mentioned in the previous section. Cathodic deposition was chosen in this study for its low cost, simple operation procedures, no need of vacuum system, mass–scale production, and relatively low temperature (< 90 ºC). Crystallinity is a critical requirement for photocatalyst [58, 59], since the excited electrons might consumed by the defects. ZnO can show crystallinity without annealing after synthesized by cathodic deposition. ZnO was thus chosen in this study for wearable devices as a functional material.

In typical cathodic deposition, oxygen, nitrate, or hydrogen peroxide are used as the source of oxygen. The reaction of nitrate reduction produces nitrite and ammonia, which progressively accumulate in the deposition bath during the synthesis and leads to deposition instabilities. On the other hand, the use of dissolved oxygen does not produce undesired reaction products, but its solubility is limited to a value lower than 10^{-3} M in hot water, and consequently ZnO electrodeposition cannot be performed rapidly with this precursor. H_2O_2 doesn't give rise to undesired reaction products and its solubility in water is high (up to 10 M). Thus, the cathodic deposition of ZnO usually combines three different oxygen sources to reach the optimized deposition.

On the other hand, zinc chloride ($ZnCl_2$) and zinc nitrate ($Zn(NO_3)_2$) are most used Zn^{2+} sources. Similarly, NO^{3-} in $Zn(NO_3)_2$ results in undesired products and the effect of chloride ion (Cl^-) from $ZnCl_2$ will be discussed in the following. Potassium chloride (KCl) and sodium chloride (NaCl) are used as supporting electrolyte for enhancing the electrical conductivity. However, it was found that Cl^- has influence on the morphology of ZnO. Because of strong adhesion of Cl^- , Cl^- may play as a capping agent blocking the grain growth on <0001> direction. In another word, the preferential adsorption of Cl^- ions onto

(0001) ZnO surfaces as one of the responsible mechanism for the formation of platelet–like ZnO nanocrystals. Chloride adsorption may result in the stabilization of (0001) ZnO surface, therefore, hindering the growth along the corresponding direction (c axis) [60]. The mechanism is shown in Figure 1- 9.

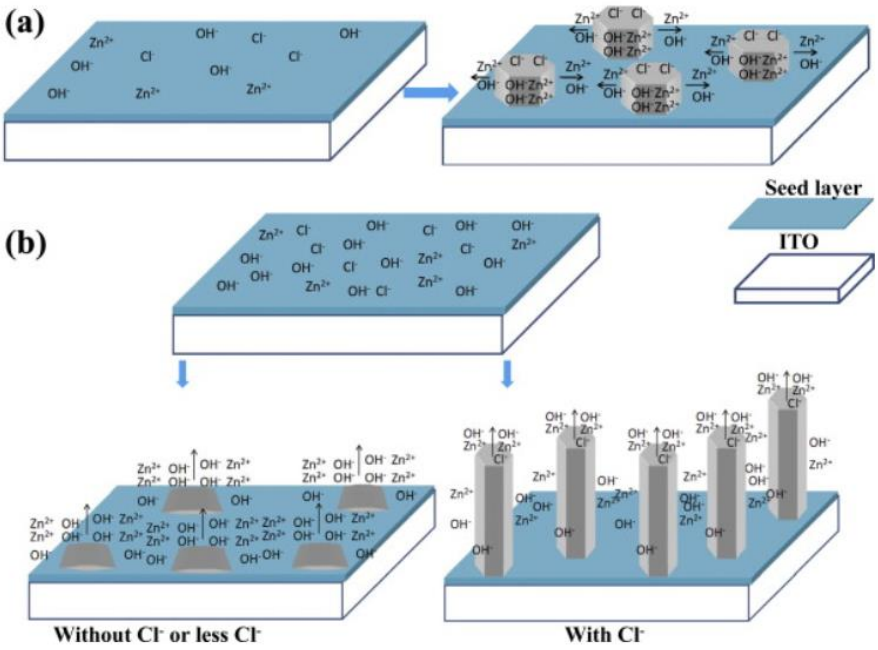

Figure 1- 9 Schematic graphs of the effect of Cl^- ions on the morphology of ZnO nanostructures under (a) low [OH^-] and (b) high [OH^-] [61]

Electrons go through the working electrode reacting with either the oxygen source and generate hydroxide (OH^-). OH^- reacts with Zn^{2+} in the solution and form zinc hydroxide ($Zn(OH)_2$). $Zn(OH)_2$ decomposes into ZnO and water eventually due to the instability of $Zn(OH)_2$. An example of ZnO formation in the cathodic deposition was shown in the eq. (1. 39), (1. 40), and (1. 41):

$$NO_3^- + H_2O + 2e^- = NO_2^- + 2OH^- \quad (1.\ 39)$$

$$H_2O_2 + 2e^- = 2OH^- \quad (1.\ 40)$$

$$Zn^{2+} + 2OH^{-} = ZnO + H_2O \quad (1.41)$$

The method consists in generating hydrogen ions at the surface of an electrode by cathodically reducing an oxygen precursor. The process leads to a pH increase in the vicinity of the electrode and to a local supersaturation for ZnO precipitation which provoke the formation of a ZnO thin film on the electrode surface. As shown in Figure 1-10, only dose ZnO precipitate when the solution is alkaline.

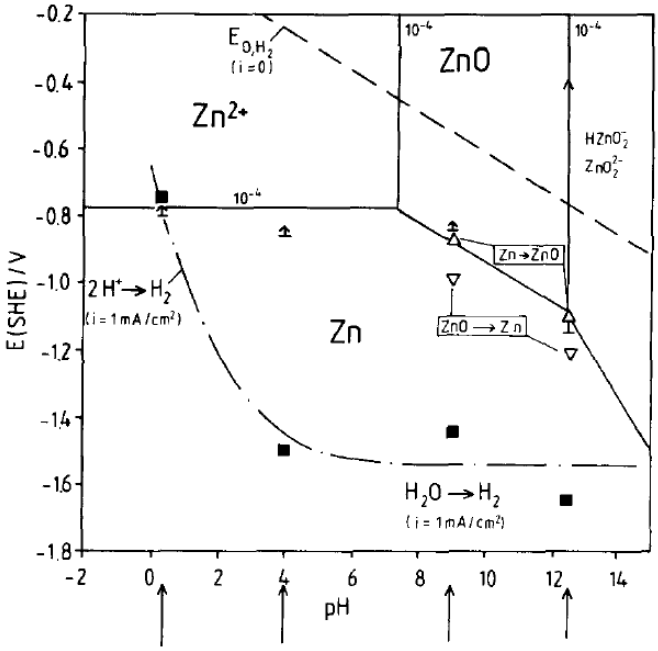

Figure 1- 10 Pourbaix diagram of the system Zn/H_2O, 10^{-4} M Zn^{2+} considering ZnO as solid substance [62]

Owing to the demands of functional materials on the wearable devices and the aforementioned merits of cathodic deposition and ZnO, cathodic deposition was used in this study to fabricate ZnO for functionalizing the textile.

1.3.2.2 Inclusion of TiO_2 (P25) into Ni–P metallization

High corrosion resistance, better surface properties [63, 64], and functional

characteristics of metallic materials are required for the development of modern technology. Composites made up of fine particles of pure metals, ceramics, and polymers in a metallic matrix have been the objective of investigation for some decades in academic and industry to improve the aforementioned properties. The composites consist of metallic matrix exhibit a broad range of enhanced properties, which satisfy the particular requirements such as improved mechanical properties, optical characteristics, high resistance to oxidation, corrosion resistance, high wear resistance, and showing functional characteristics. These materials are particularly useful for engineering and for technological utilizations in aerospace, automobile, photocatalyst, and photovoltaic industries [65].

Several preparation techniques such as plasma spraying [66], chemical and physical vapor deposition [67, 68], electro–codeposition and electroless–codeposition [65, 69], powder metallurgy [70], and sol–gel [71] have been investigated for developing composites materials with metallic matrix. Among which, the electro–codeposition and electroless–codeposition method, which consist of electrolyte and particles, has the advantages of uniform deposition on complexly shaped substrates, low cost, good reproducibility, homogeneous distribution of particles, the reduction of waste, and low processing temperature [69].

The advantages of Ni–P was mentioned in the 1.3.1.1 Ni–P metallization section. In order to improve the surface properties, electro–codeposition of metallic matrix with various types of ceramics particles such as TiO_2 [72], SiC [73], ZrO_2 [74], CeO_2 [75], and Al_2O_3 [76, 77] were studied. Among these supporting materials, TiO_2 is one of the most promising metal oxides used for the material improvement and functionalization. TiO_2

performs a variety of applications such as self–cleaning device, wastewater treatment, pollutant degradation, production of hydrogen fuel, dye–sensitized solar cell, monitoring of air contaminated by gases, and photocatalyst.

Eltoum et al. [78] synthesized Ni–TiO_2 composite from gluconate electrolyte. It is shown that the inclusion of TiO_2 nanoparticles (with mean diameter size of 50 nm TiO_2) has influence on the structure of Ni–matrix and improves the hardness and corrosion resistance of the substrate. Thiemig et al. [69] fabricated Ni–TiO_2 (with mean diameter size of 25 nm TiO_2) composite materials by electro–codeposition from two different types of Ni deposition baths: an acidic sulfamate bath and an alkaline pyrophosphate electrolyte. It was reported that the mechanical properties of the Ni–TiO_2 composite materials were enhanced while comparing to pure Ni metallization. Parida et al. [72] investigated the Ni–TiO_2 composite films by direct current deposition technique on steel substrate from Watt′s bath. The TiO_2 incorporation (with mean diameter size around 30 nm TiO_2) in the films resulted in a high micro–hardness and wear resistance compared to pure Ni metallization. Benea et al. [63] worked in the electro–codeposition of Ni and TiO_2. The results showed high hardness and wear resistance. Momenzadeh et al. [64] studied the effect of TiO_2 concentration in the electrolyte to the mechanical properties. They further introduced sodium dodecyl sulfate (SDS) surfactant into the electrolyte to increase the TiO_2 inclusion amount.

There are many studies working on the investigation of corrosion resistance, mechanical properties, or wear resistance; however, there are only very limited literature working on the photocatalytic activity of the composite materials of metal/oxide, and is especially limited in the flexible substrates. This study thus worked on the improvement

of both corrosion resistance and photocatalytic activity by the inclusion of TiO_2. Moreover, the adhesion of oxides to metallic matrix can be enhanced by the electroless–codeposition and thus the reliability can be improved comparing to cathodic deposition, which was mentioned in 1.2.3 Cathodic deposition sections.

1.4 Evaluations of fundamental properties

Electrical conductivity is an essential property for the applications in wearable devices. Hence electrical resistance of the silk/metal and silk/metal/oxide composite were evaluated by an in–line four–point probe measurement in this study. On the other hand, wearable devices are subjected to the external disturbance frequently while being employed, assessments for the reliability thus is also a fundamental prerequisite. An adhesive test to evaluate the adhesive firmness between the metallized layer and the silk substrate was conducted in this study.

Corrosion resistance is a critical property for the application due to the exposure to liquids during the employment. Polarization tests were carried out in two different solutions to evaluate the corrosion resistances of the silk/metal and silk/metal/oxide composite materials in vivo and in vitro.

Furthermore, a critical issue concerning biocompatibility assessment must be addressed for the targeting application in wearable and medical devises. According to J.C. Wataha [79], allergy reactions would be triggered when there is metal ion released from the environment and enters human body. The metal ion released from the silk/metal composite becomes a criteria for evaluating the biocompatibility. For this reason, metal ion–releasing rate was examined by immersing the silk/metal composite in a simulated body fluid (SBF) (r–type) [80] for three months in body temperature (37ºC) to assess the

biocompatibility. Since the oxides composited materials are fabricated for the functional materials such as photocatalytic and photovoltaic devices.

Photocurrent density, which is excited by the white light source is one of the most important criteria for evaluating the photocatalytic activity. Photocatalytic activity evaluations of the composite of silk/metal/oxide hybrid structure are demonstrated by measuring the photocurrent density in this study.

Chapter 2 Methodology

2.1 Catalyzation for embedding the catalysts as active sites

2.1.1 Conventional catalyzation

A $SnCl_2/PdCl_2$ solution consisted of $SnCl_2$ (10 mg/L), $PdCl_2$ (100 mg/L), and HCl (87.5 g/L) (Okuno Chemical Industries Co., Ltd., Japan) was used for the CONV catalyzation. Silk textile was immersed into the solution at room temperature and 1 atm for 10 sec to activate the silk textile. An illustration of the CONV catalyzation is shown in Figure 2- 1.

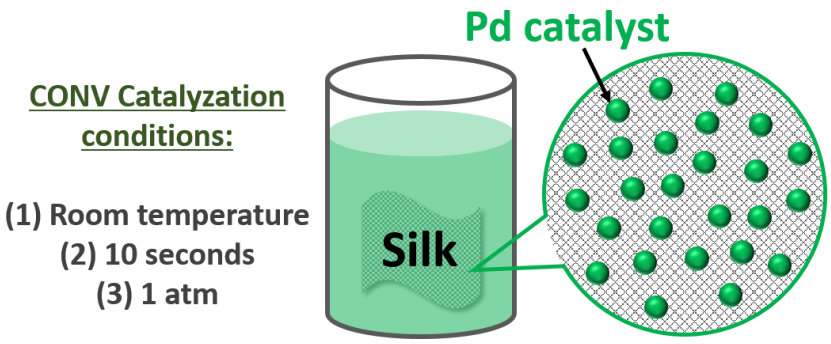

Figure 2- 1 Illustration of CONV catalyzation in $SnCl_2/PdCl_2$ (HCl) solution

2.1.2 Sc–CO_2 catalyzation

The as–received silk textile was hooked from top of the reaction cell. No pretreatment was carried out before catalyzation. Twenty–five mg of Palladium(II) acetylacetonate ($Pd(acac)_2$; 99%, Sigma–Aldrich, USA)) or Platinum(II) acetylacetonate ($Pt(acac)_2$; >99.98%, Sigma–Aldrich, USA)) was introduced into the cell to maintain the catalyst concentration at the saturation point throughout the catalyzation process. A magnetic stir bar was enclosed into the reaction cell to provide the agitation. CO_2 (99.99%, Nippon

Tansan Gas Co. Ltd., Japan) was introduced into the enclosed reaction cell. The catalyzation conditions were set at 80 ± 1 ºC and 15 ± 0.1 MPa in the reaction cell with agitation for 2 hours. No post treatment was carried out after the catalyzation. An illustration of catalyzation details is shown in Figure 2- 2. High pressure system (Japan Spectra Company, Japan) used in the catalyzation step was shown in Figure 2- 3.

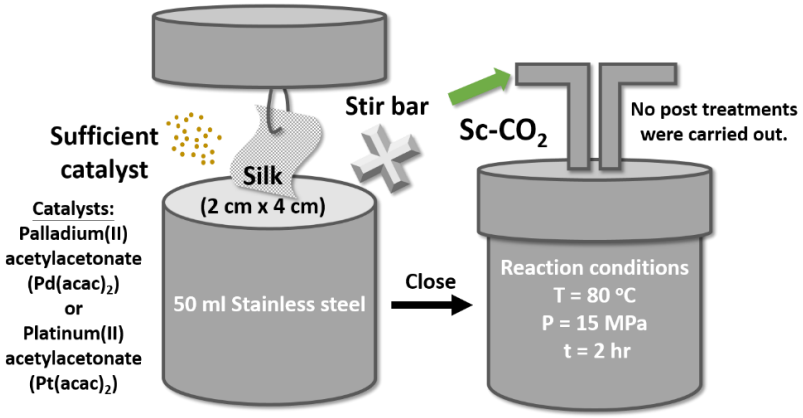

Figure 2- 2 Setup of sc–CO_2 catalyzation reaction cell

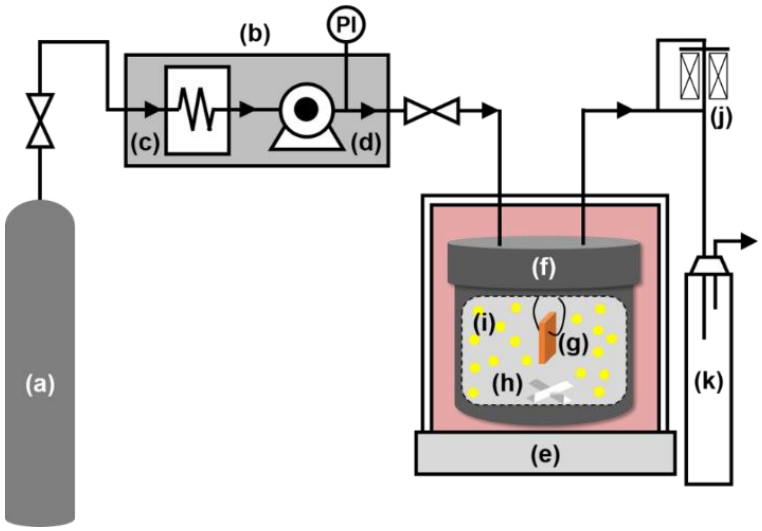

Figure 2- 3 High pressure system used to generate and inject sc–CO_2 into the reaction cell. (a) CO_2 gas tank, (b) CO_2 liquidization unit, (c) liquidization unit, (d) high pressure pump, (e) thermal bath, (f) reaction–cell (PEEK–lined SUS316L), (g) substrate, (h) cross stirrer, (i) catalyst, (j) back pressure regulator, and (k) trap

2.2 Metallization to equip silk textile with electrical conductivity

2.2.1 Conventional metallization

2.2.1.1 Ni–P conventional metallization

A commercially available acidic Ni–P electrolyte (Okuno Chemical Industries Co., Ltd., Japan) consisted of nickel chloride (1.8 wt.%), sodium hypophosphite (2.4 wt.%), complexing agent (2.4 wt.%), and ion–exchanged water (93.4 wt.%) was used in this study. The metallization was executed at an isothermal environment controlled at 70 ± 1 ºC under ambient pressure with agitation. Various Ni–P metallization times (t = 0.5, 1, 2, 3, 4, 5, 10, and 20 min) were performed to examine the relationship between the Ni–P metallization time and the metallization characteristics. No post treatment was conducted after the Ni–P metallization. An illustration of CONV Ni–P metallization was shown in Figure 2- 4.

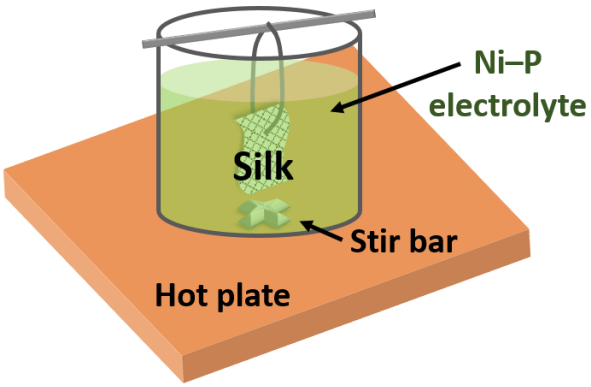

Figure 2- 4 Illustration of CONV Ni–P metallization

2.2.1.2 Pt conventional metallization

The Pt metallization electrolyte consisted of 50 vol.% of a basic Pt solution (Pt1505281, Matex·Japan Co. Ltd., Japan), 2 vol.% of a N_2H_4 reducing agent solution (Pt1505282, Matex·Japan Co. Ltd., Japan). The pH value was tuned to 12 by ammonia solution (01266–00, Kanto Chemical Co. Inc., Japan).The Pt metallization was carried

out at 70 ± 1 ºC under ambient pressure with agitation. Various Pt metallization times were performed to examine the relationship between the metallization time and the silk/Pt characteristics. No post–treatment was conducted after the metallization. Identical experimental setup was used as Figure 2- 4.

2.2.1.3 Au conventional metallization

The Au metallization electrolyte used in this study was a commercially available electrolyte (MATEX JAPAN Co. Ltd., Japan) The Au electroless plating electrolyte was composed of ammonium gold sulfite (0.2 wt.%), reducing agent (0.3 wt.%), complexing agent (0.3 wt.%), and ion–exchanged water (99.2 wt.%). A layer composed of a less noble metal is needed to initiate metallization of the Au layer. Hence, Ni–P metallization was conducted on the catalyzed silks at 70 ºC and atmospheric pressure using the Ni–P electroless plating electrolyte. Ni–P metallization time at 4 min was conducted to ensure the full coverage. Likewise, Au metallization process was executed on the Ni–P metallized silk for various lengths of metallization times (t = 3, 5, 10, 20, 40, 60, and 80 min). The Au metallization bath was set at 70 ºC and atmospheric pressure. Identical experimental setup was used as Figure 2- 4. Specimens showing a full Au coverage were selected to proceed with deposition of the ZnO layer (1.3.2 Photocatalyst on metallized silk textile section).

2.2.1.4 Ni–P/TiO_2 conventional metallization

A commercially available acidic Ni–P electrolyte (Okuno Chemical Industries Co., Ltd., Japan) consisted of nickel chloride (9.0 wt.%), sodium hypophosphite (12.0 wt.%), complexing agent (12.0 wt.%), and ion–exchanged water (67.0 wt.%) was used as Ni–P metallization solution in this study. A commercially available TiO_2 (Degussa, Evonik

Industries, Germany) was used as included particles in the Ni–P metallization layer. Different TiO_2 amounts were introduced into 100 ml Ni–P metallization individually. The concentrations of TiO_2 in the Ni–P electrolyte were from 0, 10, 20, 30, 40, and 50 (g TiO_2/L Ni–P electrolyte). Metallization time was at 10 min and the metallization was conducted at 1 atm and 70 ºC, which was controlled under water bath. TiO_2 particles were mixed tempestuously in the electrolyte for 10 min before the metallization was carried out. Electrolyte was agitated throughout the metallization process to establish suspended TiO_2 and well–mixed solution. A flow chart of pre–agitation is shown in Figure 2- 5.

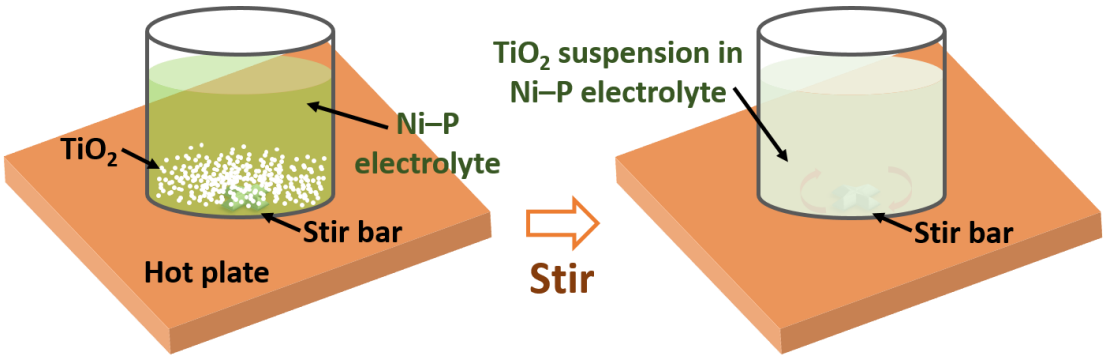

Figure 2- 5 Flow chart of the pre–agitation of Ni–P/TiO_2 deposition

2.2.2 Sc–CO_2 metallization

2.2.2.1 Pt sc–CO_2 metallization

Fifty ml of an acidic platinum–metallization electrolyte consisted of 0.06 M chloroplatinic acid hexahydrate (≥37.50% Pt basis, Sigma–Aldrich, USA), 0.15 M N_2H_4 reducing agent (24–26%, Sigma–Aldrich, USA), and 0.2 vol.% non–ionic surfactant (polyoxyethylene lauryl ether, $C_{12}H_{25}(OCH_2CH_2)_{15}OH$, 25%; Toshin Yuka Kogyo, Japan) was added into the 50 ml reaction cell. CO_2 was injected into the tightly sealed reaction cell. Pt metallization was carried out in an isothermal furnace controlled at T = 70 ± 1 ºC

and P = 15 ± 0.1 MPa with agitation. Various metallization time periods were performed to examine the relationship between lengths of the metallization time and silk/Pt characteristics. No post treatment was conducted after the metallization. An illustration of the sc–CO_2 metallization method is shown in Figure 2- 6. Same high pressure system (Figure 2- 3) was used in Pt sc–CO_2 metallization.

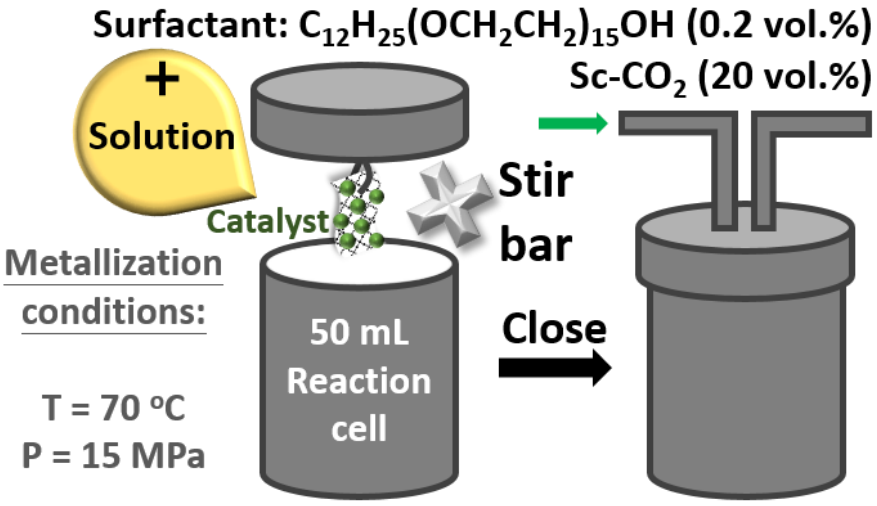

Figure 2- 6 Illustration of sc–CO_2 assisted Pt metallization

2.3 ZnO cathodic deposition to functionalize metallized silk textile

ZnO was deposited on the Au metallized silk (1.3.2 Photocatalyst on metallized silk textile section). The cathodic deposition was run at a constant current density of 0.010 A/cm^2 at 70 °C for 2 hours without agitation. Surface area of the working electrode, that is the contact area between the Au layer and the electrolyte, was estimated to be 10 cm^2, which was calculated by estimating surface area of every bundle of the Au metallized silk in a piece of the specimen. A piece of Pt foil was used as the counter electrode. The cathodic depositions were performed by using a Potentiostat/Galvanostat (1287A, Solartron Analytical, UK) (Figure 2- 7). No post treatment was conducted after the ZnO cathodic deposition step.

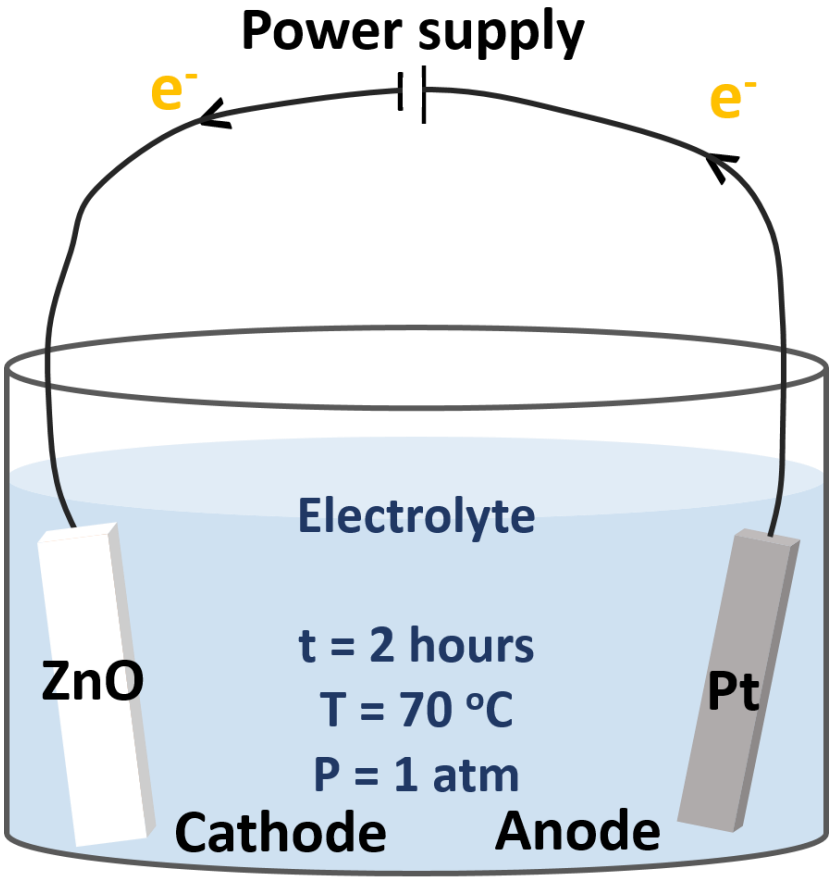

Figure 2- 7 Setup of cathodic ZnO deposition (deposition time: 2 hours, deposition temperature: 70°C, deposition pressure: 1 atm)

2.4 Evaluations of the composite materials

2.4.1 Surface morphology and crystal structure

An optical microscope (OM; VHV–5000, KEYENCE, Japan) and a scanning electron microscope (SEM; JSM–7500, JEOL, Japan) were used to observe morphologies of the composite materials. Thicknesses of the metallized layer were estimated by observing the cross–sections of metallized silks via SEM and were analyzed and calculated by ImageJ (National Institutes of Health, USA). Metallized silks were cut into two pieces to unclose the cross–section of composite materials. One piece of the composite material was fixed perpendicularly to the SEM holder surface by carbon tape

showing the cross–section to the electron beam. The composition and coverage of the metal layer were measured by energy–dispersive X–ray spectroscopy (EDX; EMAX Evolution, HORIBA, Japan) and the inbuilt elemental mapping function. The phases and crystal structures were identified by an X–ray diffractometer (XRD; Ultima IV, Rigaku, Japan) with Cu k_{α} radiation.

2.4.2 Electrical conductivity

An in–line four–point probe with 1.5 mm distance between each probes (MCP–T370, Mitsubishi Chemical Analytech Co. Ltd., Japan) was carried out to evaluate the electrical resistance with the samples dimension in 1 cm x 0.5 cm (length x width) at room temperature. Ten times of the electrical resistance measurement were carried out to ensure reliability of the values reported and build up the error bar. An illustration of electrical resistance measurement is shown Figure 2- 8.

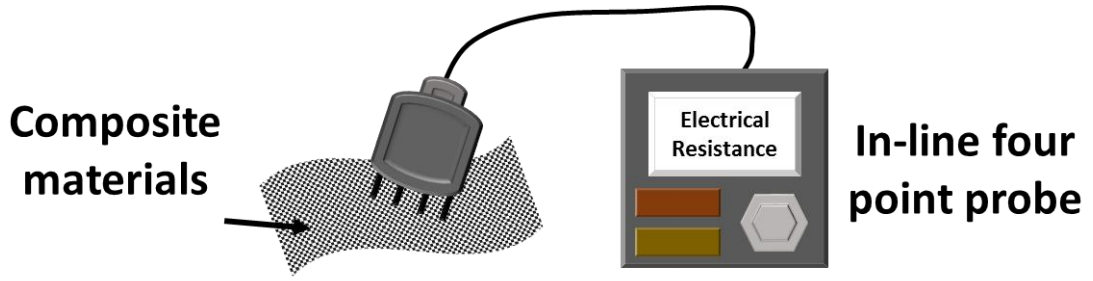

Figure 2- 8 Illustration of electrical resistance measurement of silk/metal composites

2.4.3 Adhesive firmness

An adhesive test was conducted to evaluate reliability of the silk/metal composite (Figure 2- 9). For the adhesive test, a piece of 3M tape (810 Scotch® Magic™ Tape, 3M, USA) was firmly stuck to the sample surface by applying a 1–kg load and peeled off repeatedly. The adhesive test with one and two cycles of the sticking–peeling procedure are named first adhesive test and second adhesive test. The electrical resistance was

measured before and after the adhesive test to evaluate the durability and firmness of the metallized layer. Similarly, ten times of the electrical resistance measurements were carried out to ensure reliability of the values reported and construct the error bar.

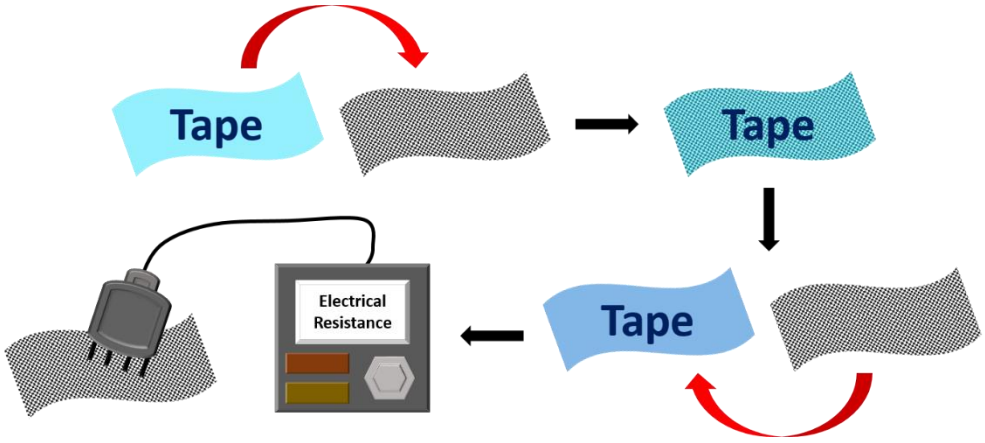

Figure 2- 9 Procedures of adhesive test for the composite materials

2.4.4 Corrosion resistance

The corrosion resistance was measured by polarization measurements in 3.5 wt.% NaCl or a SBF solutions (r–type) (Figure 2- 10). The 3.5 wt.% NaCl solution was used to simulate the human sweat [81] and the SBF solution was used to simulate human body fluid. These two solutions were thus chosen for the in vitro and in vivo simulation, respectively. The potentiodynamic polarization curves were measured by using a Potentiostat/Galvanostat (1287A, Solartron Analytical, UK). The silk/metal composite with lowest electrical resistance, a Pt plate, and an Ag/AgCl reference electrode were used as the working electrode, the counter electrode, and the reference electrode, respectively. Total surface area of the working electrode , which is a piece of the 1 x 1 cm^2 silk/metal composite, was calculated by considering surface area of every bundle of the metallized silk textile, and the value was 9.5 cm^2. The Pt counter electrode was cleaned ultrasonically in ethanol and pure water for 1 min, respectively, before the polarization measurements.

The scan range started from –0.8 to + 0.4 V (for Ni–P), from –0.4 to + 0.6 V (for Pt) vs Ag/AgCl, or from –0.8 to + 0.2 V (for Ni–P/TiO_2) at a scan rate at 1 mV/s. Prior to the potentiodynamic test, the three electrodes were immersed into the solution for 25 min to certify the stability.

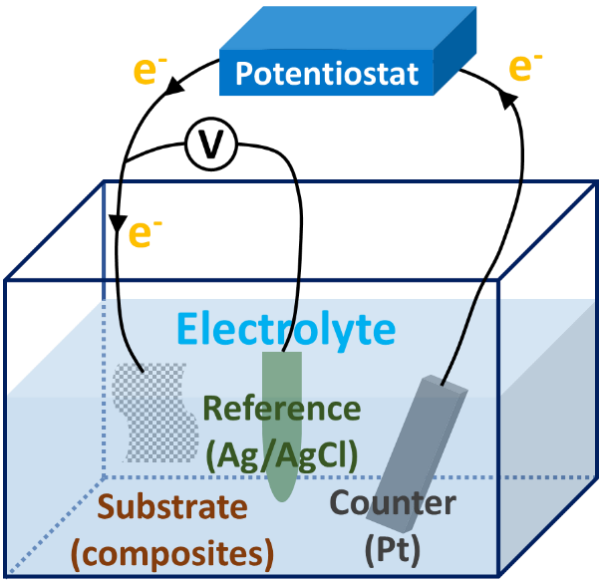

Figure 2- 10 Experimental setup of corrosion resistance measurement

2.4.5 Immersion test for evaluating biocompatibility

The metal ion releasing rate was evaluated by an immersion test (Figure 2- 11). In the immersion test, a piece of the sample was immersed in the SBF in a 30 ml container at 37 ºC (body temperature) for three months. Then, ~15 ml of the SBF solution was drawn out and centrifuged for 2 hours to remove undesired particles from the solution. Released metal ion concentration was measured by inductively coupled plasma atomic emission spectroscopy (ICP–AES; ICPS–8100, Shimadzu Co. Ltd., Japan). Ten times of the ICP measurement were carried out to ensure reliability of the values reported.

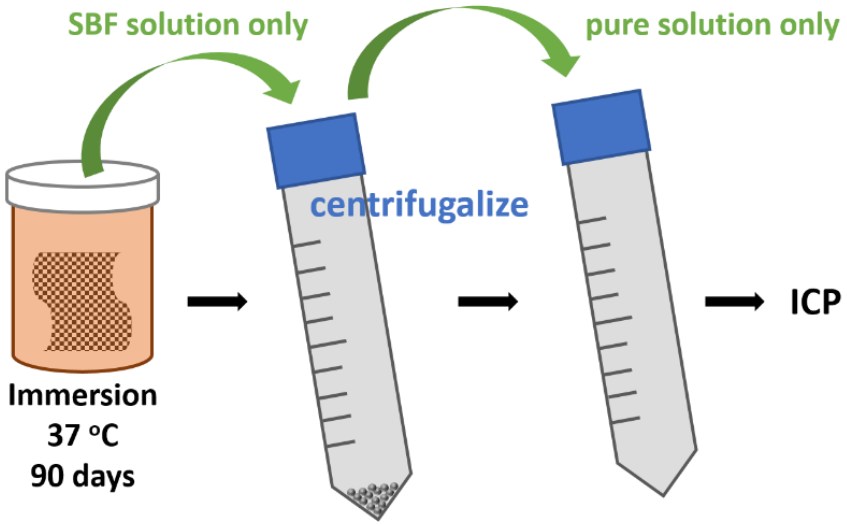

Figure 2- 11 Flow chart of immersion test for evaluation of ion releasing rate

2.4.6 Photoelectrochemical measurement

The silk/metal/oxide composite (i.e. silk/Au/ZnO and silk/Ni–P/TiO_2), a Pt plate, and an Ag/AgCl reference electrode were used as the working electrode, the counter electrode, and the reference electrode, respectively. The chronoamperometric I−t curves were recorded at 0 V vs Ag/AgCl using the Potentiostat/Galvanostat under white light illumination (500 W xenon lamp, with a light intensity of 100 mW/cm^2) at room temperature. A Na_2SO_4 (0.5 M) solution was used as the electrolyte. Since the composite materials show cross–linked and sophisticated surface, the surface area of metal oxides were processed and calculated by a built–in software of the OM. Similarly, ZnO coverage on the Au layer was also processed and calculated by a built–in software of the OM. The setting for the photoelectrochemical measurement was illustrated by Figure 2- 12.

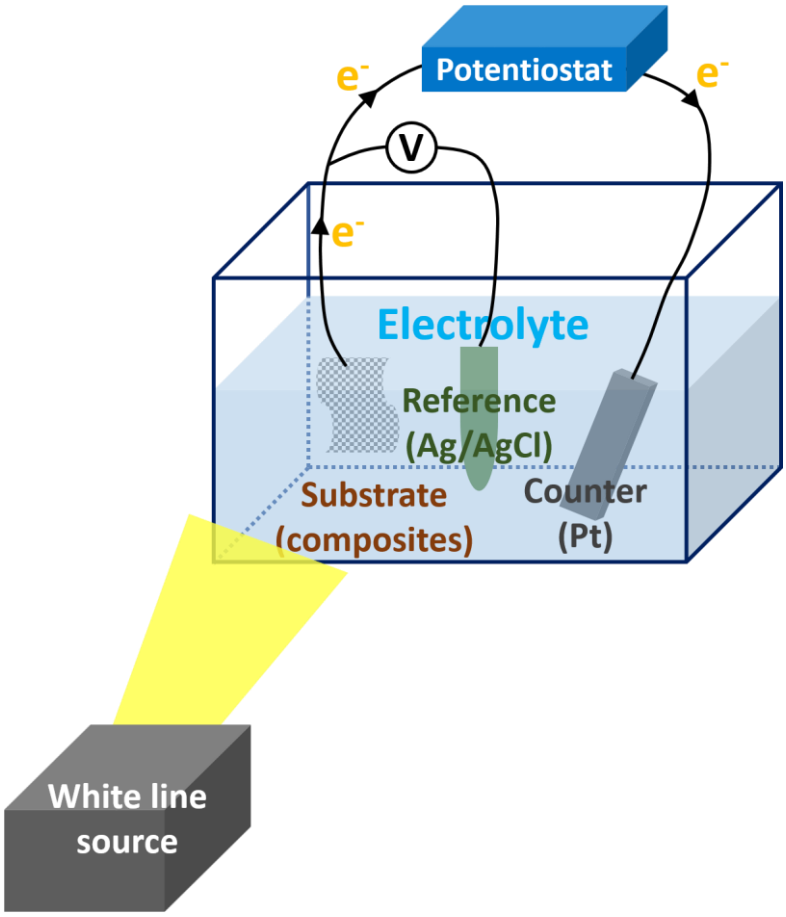

Figure 2- 12 Experimental setup of photocurrent density measurement (evaluation temperature: room temperature, electrolyte: 500 mL Na_2SO_4, evaluation pressure: 1 atm, without agitation)

Chapter 3 Ni–P metallized silk textile via sc–CO_2 promoted electroless plating to practice electrically conductive silk textile

3.1 Introduction

Ni-P is consider as a promising material toward the applications of wearable devices due to the well–developed Ni–P electroless plating technique, low cost, and tunable crystallinity. Ni–P was thus chosen in this study to practice the electrically conductive textile for the applications of wearable devices.

3.2 Activation of silk textile via sc–CO_2 $Pd(acac)_2$ catalyzation

Figure 3- 1 shows OM images and X–ray diffraction patterns of the as–received silks and the sc–CO_2 catalyzed silks. The interwoven transparent bundles shown in Figure 3- 1(a) indicate the silk textile and Figure 3- 1(b) shows a broad peak around $2\theta = 20^{o}$, this broad peak reveals an amorphous structure of the silk textile. The light yellow flakes around the silk bundles in Figure 3- 1(c) specify the sc–CO_2 deposited $Pd(acac)_2$ catalysts and the diffraction peaks in Figure 3- 1(d) labelled by triangle symbols can be indexed to $Pd(acac)_2$ very well [82, 83], indicating the $Pd(acac)_2$ catalysts were successfully deposited on the silk substrates. As demonstrated in the Figure 3- 1(a) and (c), the silk textile remained undamaged after the 2 hours sc–CO_2 catalyzation treatment due to the low surface tension, low viscosity, and non–corrosive properties to most of polymers of sc–CO_2 [15, 21, 84]. Deposited $Pd(acac)_2$ catalysts were reduced to Pd metal particles by

reducing agent (N_2H_4 in this study) in the succeeding metallization electrolyte and act as active sites for triggering the Ni–P metallization reactions.

The sc–CO_2 catalyzation practiced a significant advancement when it is compared to the CONV catalyzation process [15]. In the CONV catalyzation, on the contrary, silk substrate was damaged by the acidic catalyzation solution (Figure 3- 2). CONV catalyzation consists of $SnCl_2$ and $PdCl_2$ in the HCl electrolyte. However, HCl solution is erosive to most of the polymers (i.e. silk). In addition, the catalysts were only deposited on the substrate surface. Although it was considered that increasing the immersion time in the catalyzation solution is helpful for the deposition of catalysts, silk substrate is also damaged severely in the same time.

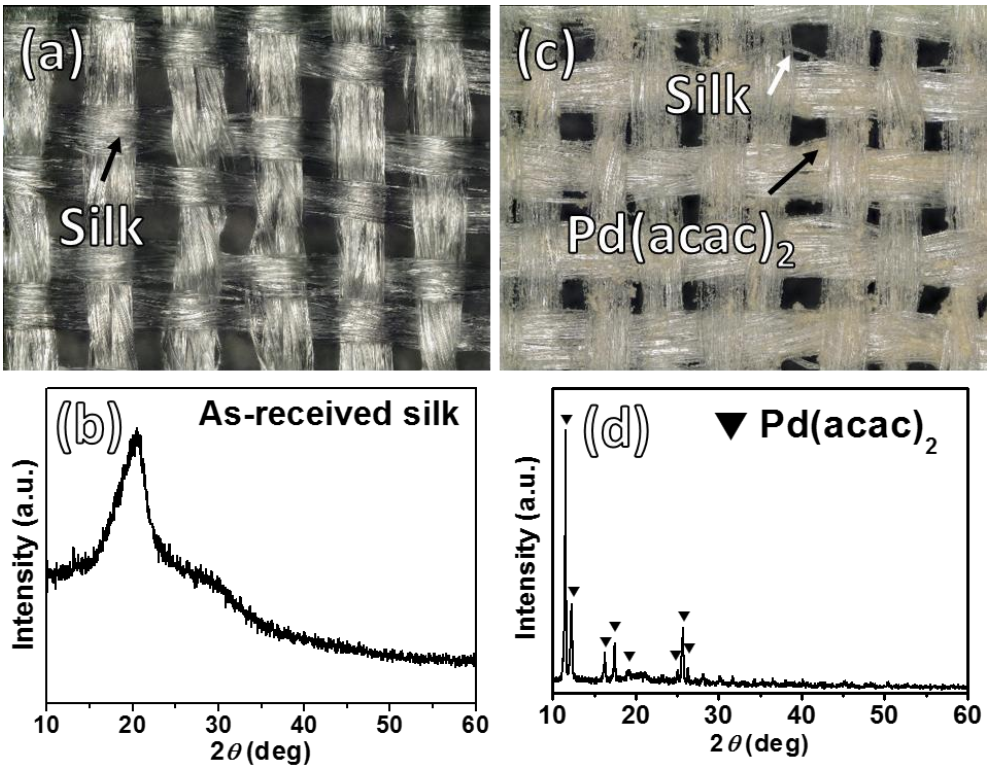

Figure 3- 1 (a) OM image and (b) X–ray diffraction pattern of the as–received silk, and (c) OM image and (d) X–ray diffraction pattern of the sc–CO_2 catalyzed silk (triangle symbols: $Pd(acac)_2$ catalysts)

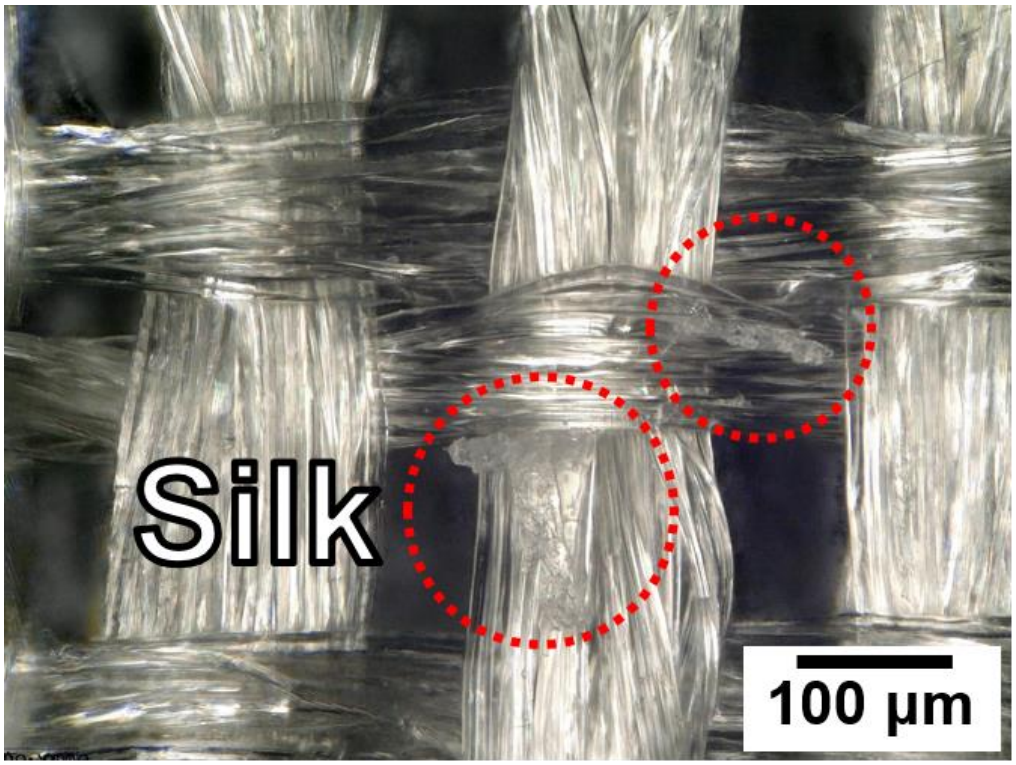

Figure 3- 2 OM image of conventionally catalyzed silk at room temperature without agitation (red dashed circles: damaged silk substrate)

Figure 3- 3 shows the cross–sections of backscattered electron SEM images treated by sc–CO_2 catalyzation process at (a) 1 hour and (b) 2 hours. Dark gray phase indicates epoxy, light gray phase suggests the cross–section of silk substrate, and the bright spots in nano–size are reduced $Pd(acac)_2$ catalysts. In Figure 3- 3(a), $Pd(acac)_2$ catalysts were embedded into the silk substrate around 190 nm. On the contrary, a great amount of $Pd(acac)_2$ catalysts were embedded into the silk substrate after 2 hours sc–CO_2 catalyzation treatment (Figure 3- 3(b)). The catalysts were successfully embedded into the substrate around 330 nm in the depth due to the non–polarity among sc–CO_2, $Pd(acac)_2$ catalysts, and silk substrate and low surface tension of sc–CO_2 [15, 16, 84, 85]. Structure of silk substrate still remained intact after the sc–CO_2 catalyzation treatment.

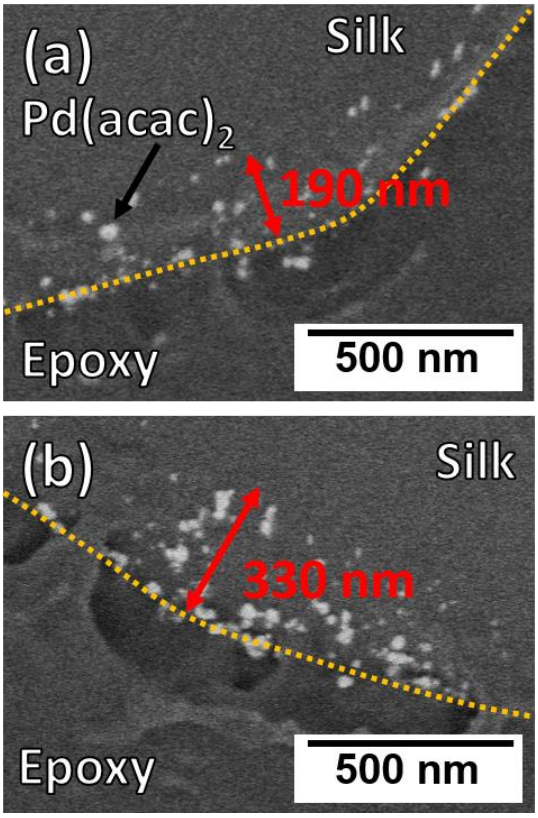

Figure 3- 3 Cross–section of backscattered electron SEM images of catalyzed silk at (a) 1 hour and (b) 2 hours at 80 ºC and 15 MPa

3.3 Morphology, composition and structure of silk/Ni–P

X–ray diffraction patterns of (a) the as–received silk, (b) the sc–CO_2 catalyzed silk, (c) the catalyzed/reducing agent treated silk, and (d) the catalyzed/Ni–P electrolyte treated silk are shown in Figure 3- 4. In Figure 3- 4(a), a board peak at around $2\theta = 20^{o}$ indicates amorphous structure of the silk. The characteristic peaks in the Figure 3- 4(b) correspond to the $Pd(acac)_2$ well indicating the catalysts were successfully settled on the substrate. Due to the high intensity from $Pd(acac)_2$ catalysts, no silk characteristic peaks were observed in Figure 3- 4(b). shows the reduced catalysts on the silk substrate, $Pd(acac)_2$ catalysts were reduced to metallic palladium particles after immersing the catalyzed silk in a solution containing the reducing agent for 15 min at 70 ºC. According

to Y.S. Cheng et al. [86] and C.R. Bhattacharjee et al. [87] the reduction reaction of $Pd(acac)_2$ is believed to be the eq. (3. 1) :

$$2Pd(acac)_2 + 2H_2PO_2^- + 2H_2 = 2Pd + 2H(acac) + 2HPO_3^{2-} + H_2 + 2H^+ \quad (3.\ 1)$$

After the reduction, the catalyst–contained silk surface became active and allowed initiation of the Ni–P metallization [88]. No $Pd(acac)_2$ was found in Figure 3- 4(c) indicating that $Pd(acac)_2$ was fully reduced to Pd metallic particles. Four diffraction peaks, locate at 2θ = 40.1°, 46.6°, 68.1°, and 82.1° can be indexed to (111), (200), (220), and (311) planes of the FCC structure for palladium (JCPDS #89–4897). In Figure 3- 4(d), a broad peak locates at 2θ = 20° can be indexed to the silk substrate, while the other broad peak shows around 40–50° representing the amorphous Ni–P metallized layer. No Pd or $Pd(acac)_2$ characteristic peaks can be observed after the metallization indicating that the small amount of Pd metallic particles were thoroughly covered by the deposited Ni–P. No impurities were found in the detection limitation.

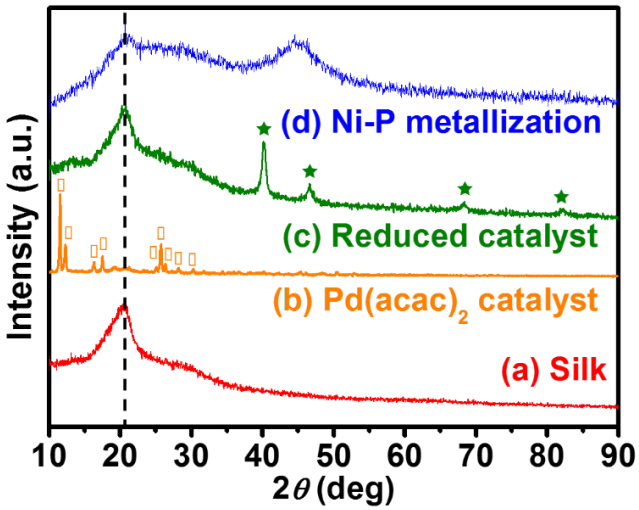

Figure 3- 4 X–ray diffraction patterns of (a) non–catalyzed pure silk, (b) $Pd(acac)_2$ catalyzed silk, (c) catalyzed/reduced silk, and (d) Ni–P metallized silk, respectively

Morphologies of the metallized silks with various metallization times are shown in Figure 3- 5. Figure 3- 5(a) and (b) show the OM and SEM images of the Ni–P metallized silk deposited for 30 sec and 1 min, respectively. As shown in Figure 3- 5(a), small amounts of the catalysts were still un–reduced (circled) and part of the silk was still un–metallized showing the transparent color after 30 sec of the metallization time. No SEM image is shown here due to the poor electrical conductivity of the specimen. Similarly, in Figure 3- 5(b), the bright color in the inserted SEM image indicates silk surfaces are still not fully covered by the Ni–P layer (pointed by arrows), and the Ni–P layer is still not continuous resulting a high electrical resistance (results shown in the 3.4 Electrical property and adhesive test of silk/Ni–P section). Results obtained in this study are classified into three stages according to the surface morphology and electrical conductivity. The specimens with non–continuous Ni–P are classified into the first stage, which are specimens metallized at 30 sec and 1 min. On the other hand, in Figure 3- 5(c), Ni–P layer shows a continuous and a complete coverage at 3 min of the metallization time. The least time needed to construct full coverage is defined as the minimum time. Silk substrate metallized for 4 min is shown in Figure 3- 5(d) demonstrates the full coverage and a consecutive growth of the Ni–P thickness. Silks metallized for 3 and 4 min of the metallization time both having a full coverage and smooth surface are classified into the second stage. Beyond 5 min of the Ni–P metallization time, rough surface were formed, which resulted deteriorated electrically conductive properties (discussed in the 3.4 Electrical property and adhesive test of silk/Ni–P section). Meanwhile, redundant Ni–P clusters (pointed by arrows) accumulated on the surface with an increase in the Ni–P metallization time (Figure 3- 5(e) and (f)). The specimens with the metallization time longer than 5 min are classified into the third stage.

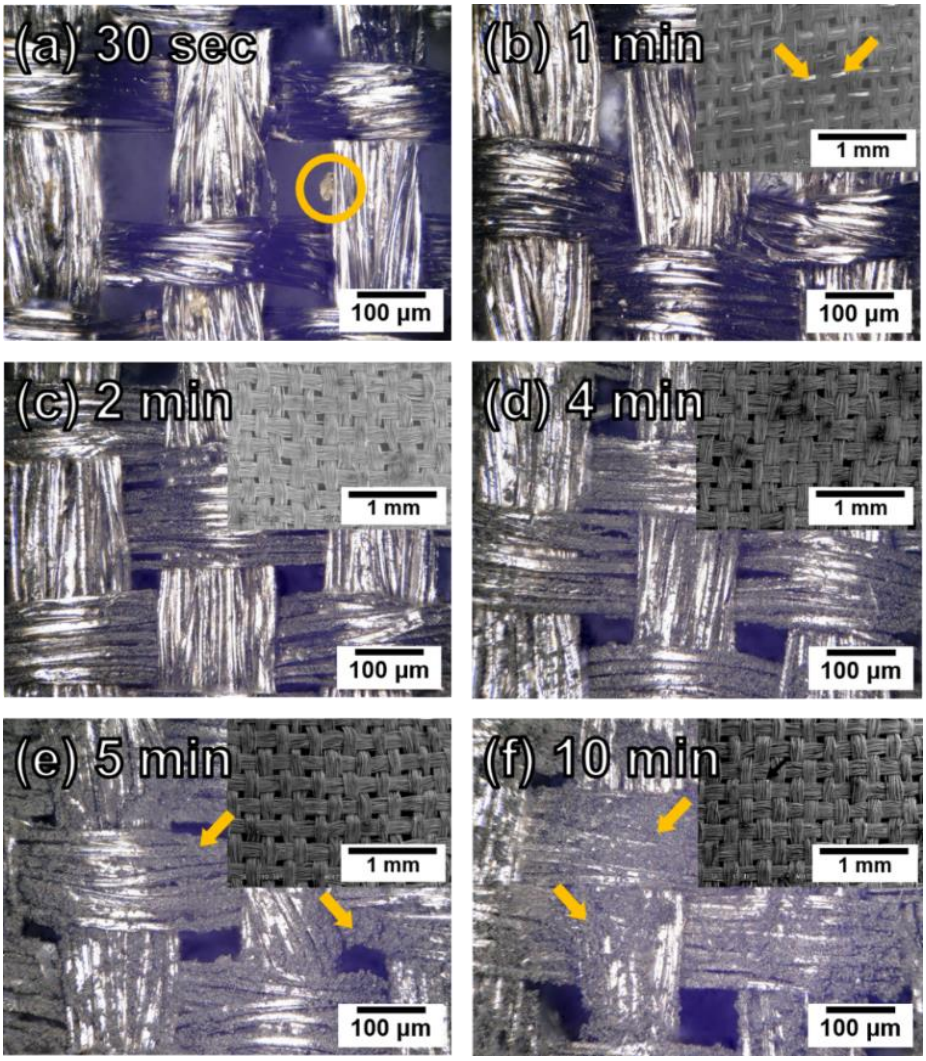

Figure 3- 5 OM images of the Ni–P metallized silk composites prepared by (a) 30 sec, (b) 1 min, (c) 2 min, (d) 4 min, (e) 5 min, and (f) 10 min of the metallization time

Elemental mapping results from the 4 min Ni–P metallization time are presented in Figure 3- 6. Ni and P were homogeneously metallized on the silk substrate. All compositions of Ni–P layer in various metallization times were revealed in Table 3- 1. Although carbon signal was found in the elemental mapping (Figure 3- 6). It is considered that the carbon signal was from silk substrate and contamination on the surface of the composite materials. Compositions in Table 3- 1 was not considered, only Ni and P concentration are shown.

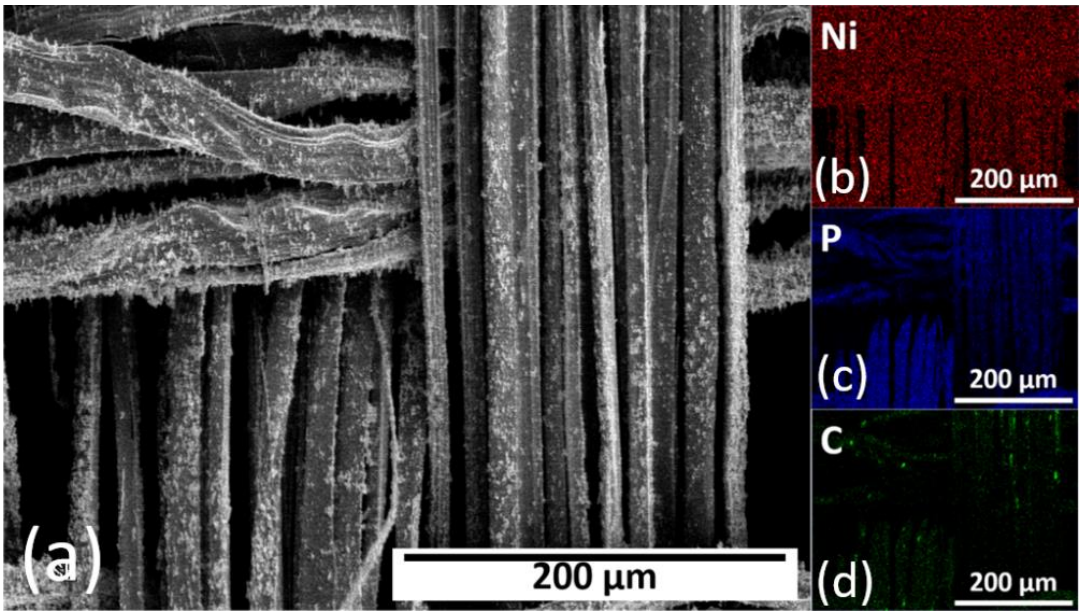

Figure 3- 6 Elemental mapping of the silk/Ni–P composite prepared by 2 min of the Ni–P metallization time at 70°C and 1 atm with agitation, (a) SEM image, (b) nickel, (c) phosphorus, (d) carbon

Table 3- 1 Ni–P compositions in various metallization times

Comp.	1 min	2 min	3 min	4 min	5 min	10 min	20 min
Ni (at.%)	83.8	83.8	83.9	82.2	82.1	82.5	82.4
P (at.%)	16.2	16.2	16.1	17.8	17.9	17.5	17.6

The metallization time dependence of the Ni–P layer thickness is presented in Figure 3- 7. Positive correlation in the metallization time and the thickness is demonstrated. Thickness of the Ni–P layer with the longest metallization time (20 min) was 0.7 µm. A decelerated growth rate can be observed when the metallization time is longer than 5 min, which can be attributed to the lowered Ni ion and reducing agent concentrations in the bulk metallization solution. Ni ions and reducing agent in the solution were consumed rapidly in the metallization step. At the beginning of the metallization, the concentrations were high and gave a Ni–P layer growth rate at

approximately 0.08 μm/min in the initial 5 min of the metallization time. On the other hand, the Ni ion and the reductant concentrations continued to drop and caused the growth rate to slow down to approximately 0.005 μm/min after 5 min of the metallization time.

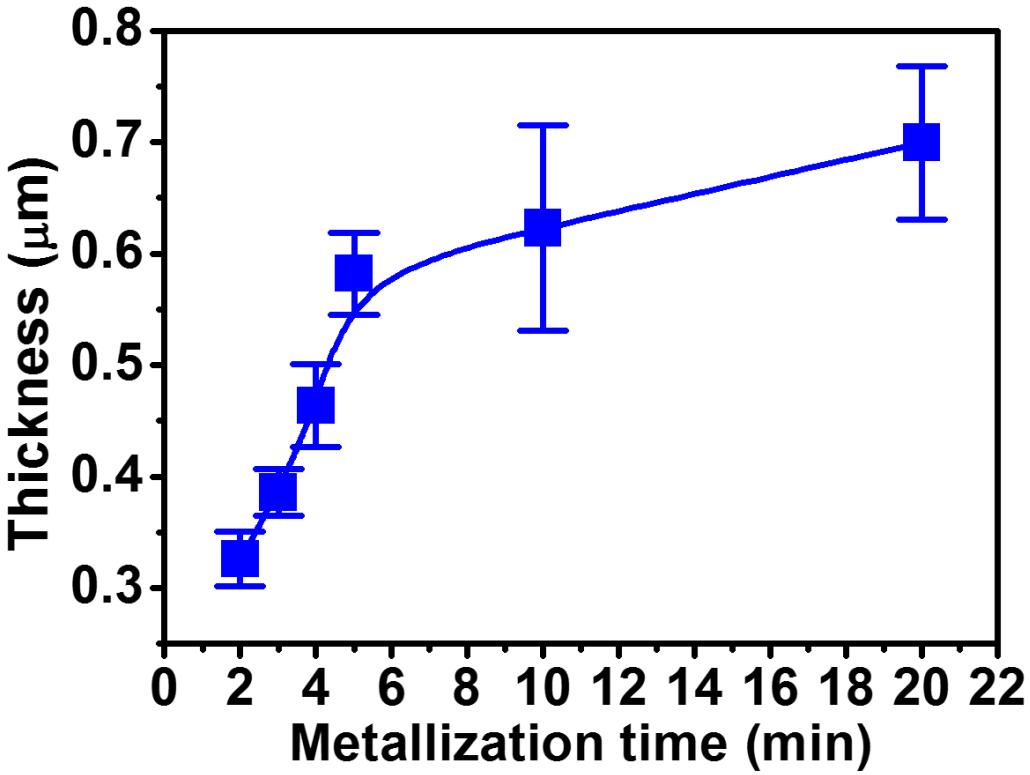

Figure 3- 7 The Ni–P metallization layer thickness metallized on silk substrate as a function of the metallization time

3.4 Electrical property and adhesive test of silk/Ni–P

Figure 3- 8 illustrates the electrical resistance as a function of the Ni–P metallization time before and after the adhesive tests. The silk/Ni–P composites showed high electrical resistance since the electrically conductive Ni–P metal layer was discontinuous when the Ni–P metallization time was less than 2 min, which is referred as the first stage (Figure 3- 5(a) and (b)).

The lowest electrical resistance at 1.02 Ω was achieved as the Ni–P metallization time was extended to 4 min. The metallization to reach the lowest electrical conductivity is defined as optimized time. This result is in line with the coverage shown in Figure 3- 5 indicating that the coverage is one of the critical factors affecting the electrical property of the Ni–P composite materials. Time duration between the beginning of the full coverage and the time required to reach the minimum resistance is corresponded as the second stage.

Metallization time beyond 5 min is classified into the third stage, which the electrical resistance is offset by the roughened Ni–P surface. In the third stage (Figure 3- 5(e) and (f)), the growth of rough and loose Ni–P particles on the silk substrate surface would bring unnecessary Joule heating and more electron scattering, which are the main reasons for the deteriorated electrical resistance to the Ni–P composite materials [89]. In addition, a direct evidence indicating the increase of the roughness with respect to the metallization time is revealed in Figure 3- 9. Figure 3- 9(a) shows surface morphology of the silk/Ni–P composite with 1 min of the metallization time. The surface metallized by the Ni–P layer is smooth and charging effect is observed at the region, which was not covered by the Ni–P layer. On the other hand, Figure 3- 9(b) and (c) demonstrate the surface roughness increased when the Ni–P metallization time is increased to 2 and 5 min. A proportional relationship between the electrical resistance and the roughness has been indicated in a previous study [90].

Standard deviation of the electrical resistance decreases with the metallization time indicating that the inhomogeneity can be mitigated as the metallization time extends in the first two stages. However, the standard deviation increases after the second stage

due to the increased surface roughness. A reliable electrical resistance cannot be obtained owing to the poor conductivity when the metallization time is less than 2 min. Specimen prepared by the CONV catalyzation and metallization at 4 min is also shown in Figure 3-8. Specimens fabricated by the CONV catalyzation show higher electrical resistance than those catalyzed by sc–CO_2 method due to the deteriorated substrate surface. Rough substrate surface results in the coarse deposition of Ni–P and finally leads to the high electrical resistance. Moreover, since the catalysts are only attach to the substrate surface, electrical resistance changed significantly after adhesive tests.

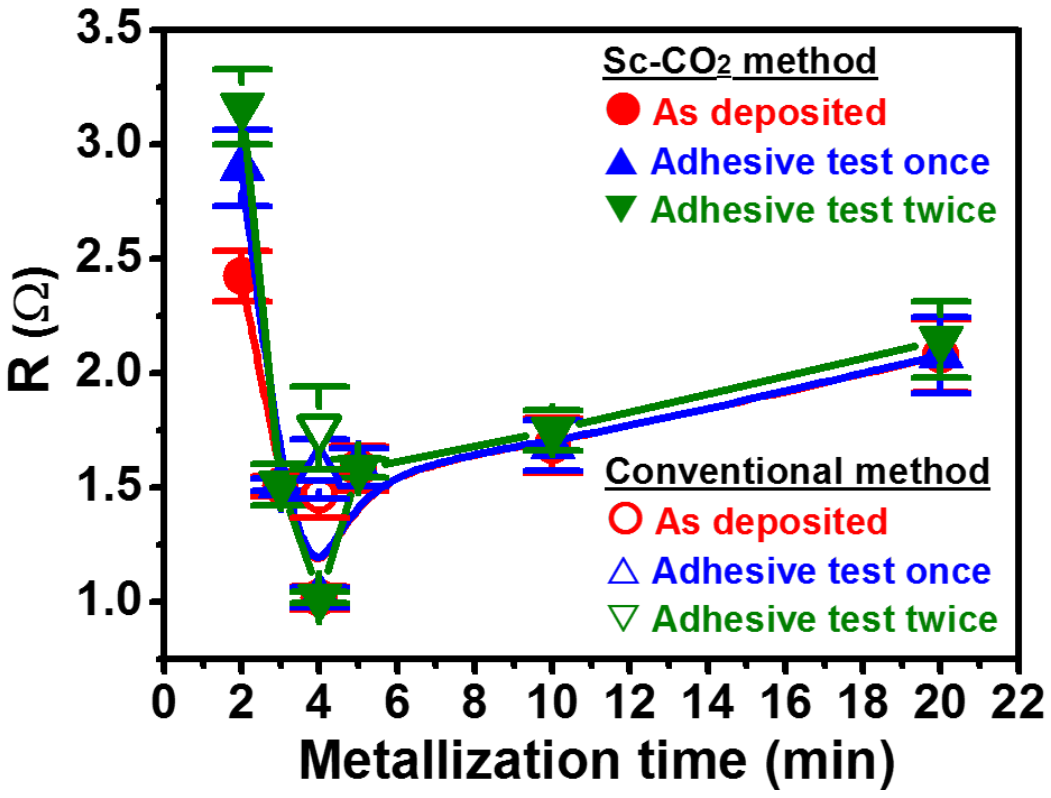

Figure 3- 8 Electrical resistance curves of the Ni–P metallized silk composites before and after the adhesive test at room temperature and 1 atm (red circle: as–deposited; blue upward triangle: first adhesive test; and green downward triangle: second adhesive test) (solid symbols: sc–CO_2 method; hollow symbols: CONV method)

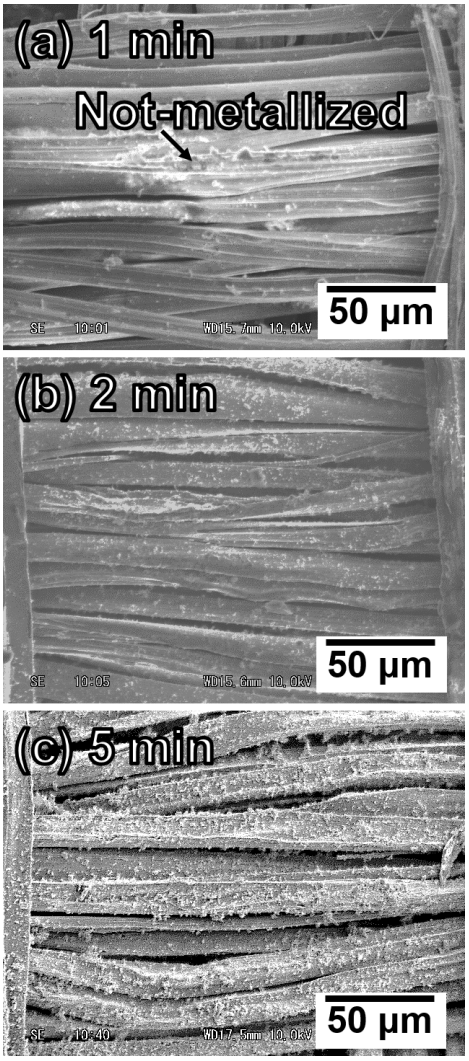

Figure 3- 9 SEM images showing surface condition of the silk/Ni–P composite prepared by (a) 1 min, (b) 2 min, and (c) 5 min of the metallization time

A summary of the influence of the morphology on the electrical resistance in different stages is illustrated in Figure 3- 10. In the first stage, the Ni–P layer is non–continuous resulting in poor electrical conductivity. When the metallization time is extended to the second stage, a continuous Ni–P layer is constructed, in other words, the silk is fully covered. A full coverage, a smooth surface, and a sufficient Ni–P layer thickness result in the lowest electrical resistance. In the last stage, the electrical conductivity is offset by the increased roughness.

The electrical resistances after the adhesive tests are shown in Figure 3- 8. The electrical resistances persist in the second and third stages even after second adhesive test. In addition, there is no distinct change among these three measurements. However, the adhesive tests show serious impact on the samples in the first stage. Since the joint of the non–metallized silk surface and the Ni–P layer can be the weak points of the composite materials, thus, it was destructed more severely than the Ni–P fully covered samples. The silk/Ni–P composite metallized with the optimized time shows perseverance in the adhesive tests indicating its feasibility in the practice of wearable devices even under adverse conditions.

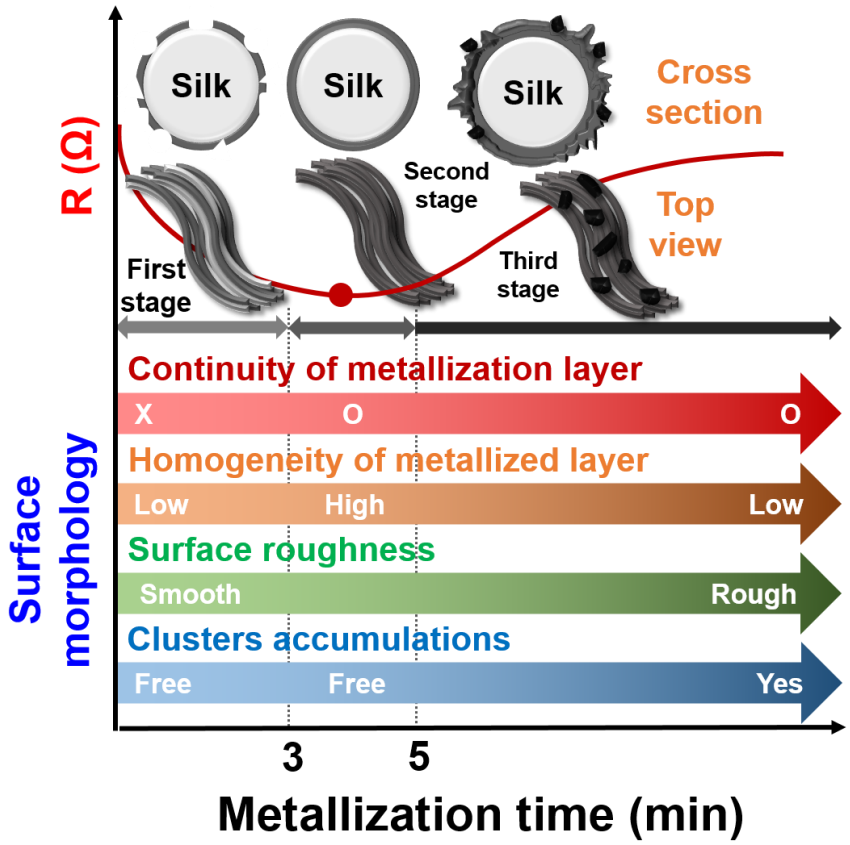

Figure 3- 10 A summary of morphology and electrical resistance of the Ni–P metallized silk as well as the correlations between each properties

3.5 Corrosion resistance of silk/Ni–P

Corrosion behaviors of the silk/Ni–P composites in 3.5 wt.% NaCl are shown in Figure 3- 11. Figure 3- 11(a) shows the Tafel plots of the as–deposited silk/Ni–P composite and the silk/Ni–P composite after the adhesive tests. The silk/Ni–P composite prepared by 4 min of the metallization time was chosen for the corrosion resistance evaluations. No significant difference was found among the three curves indicating excellent reliability of the Ni–P layer on the silk surface even after second adhesive test. The corrosion potential (E_{corr}) and the corrosion current density (I_{corr}) are summarized in Table 3- 2. The corrosion current densities are comparable to those of Ni–P layer on metal substrate reported in other studies [91-94], which indicate the high corrosion resistance of the Ni–P layer retained even when it is metallized on a non–metallic substrate. Moreover, Figure 3- 11(b) shows the morphology after second adhesive tests and the corrosion test, no obvious corrosion attack can be observed after the testing. The low corrosion rate in a solution simulating the human sweat before and after the adhesive test demonstrates the silk/Ni–P is practical in wearable devices.

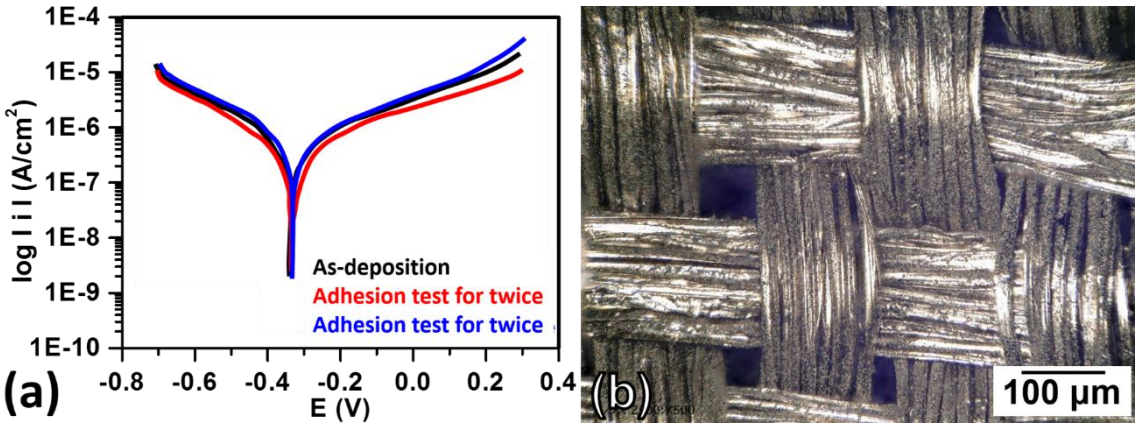

Figure 3- 11 (a) Tafel plots of the silk/Ni–P composite prepared with 4 min of the metallization time before and after the adhesive tests and (b) an OM image of the silk/Ni–P composite after second adhesive test and the corrosion test

Table 3- 2 Corrosion potentials and corrosion current densities of the silk/Ni–P composite materials

Samples	E_{corr} (V)	I_{corr} (A/cm^2)
(a) As–deposited	-0.32	5.89 x 10^{-7}
(b) First adhesive test	-0.33	6.00 x 10^{-7}
(c) Second adhesive test	-0.32	5.93 x 10^{-7}

3.6 Brief summary for silk/Ni–P

Ni–P metallized silk with a high electrical conductivity and a high corrosion resistance in a solution simulating the human sweat was successfully fabricated by the sc–CO_2–assisted electroless plating in this study. Reliability evaluations were conducted by the adhesive test to demonstrate the value in practical applications. In the catalyzation step, the silk substrate was successfully catalyzed by $Pd(acac)_2$ catalyst without any defects owning to usage of the sc–CO_2. The coverage and the thickness of the Ni–P layer increased as a function of the metallization time. The maximum thickness at 0.7 μm was attained by 20 min of the metallization time. The deposition statuses are classified into three stages. The composite material remains high electrical resistance in the first stage, which can be attributed to the non–continuous Ni–P layer on the silk surface. On the other hand, the lowest electrical resistance was achieved in the second stage owning to the full coverage and the smooth surface. Finally, the surface roughness increase in the third stage, which lead to a deteriorated electrical conductivity. The lowest electrical resistance of 1.02 Ω was reached by 4 min of the metallization time. The Tafel plots show the silk/Ni–P composite material possesses an excellent corrosion resistance and the adhesive tests demonstrate the firmly adhesive property of the Ni–P layer on the silk.

Chapter 4 Pt metallized silk textile via sc–CO_2 promoted electroless plating to improve the biocompatibility of the composite

4.1 Introduction

There are always dilemma between cost and quality. For example, Ni–P owns the advantages of low cost and simple operation procedures, however, it might cause allergy reactions to some of the users under some specific circumstances. On the other hand, platinum owns high biocompatibility but it shows high cost and complicated procedures. Since part of the wearable devices have contact to human body or are implanted into human body directly, it is important to make the wearable devices biocompatibility. Pt is widely considered as a biocompatible material. Along with the combination of silk, which is also a biocompatible materials, the fully biocompatible composite materials can be realized in this study. Thus the metallization material was shifted to Pt catalyzation followed by Pt metallization in this section to fulfill the fully biocompatible composite materials for the applications of wearable devices.

4.2 Activation of silk textile via sc–CO_2 $Pt(acac)_2$ catalyzation

Figure 4- 1(a) and (b) show the uncatalyzed silk and the silk textile after the catalyzation, respectively. The light yellow flakes correspond to the $Pt(acac)_2$ catalyst, and the transparent thread bundles represent the silk. By means of conducting the catalyzation with sc–CO_2, the catalysts can be distributed into the silk textile without damaging the silk structure. Although some of the catalysts aggregate in a small range,

distribution of the catalysts in the substrate is nearly homogeneous.

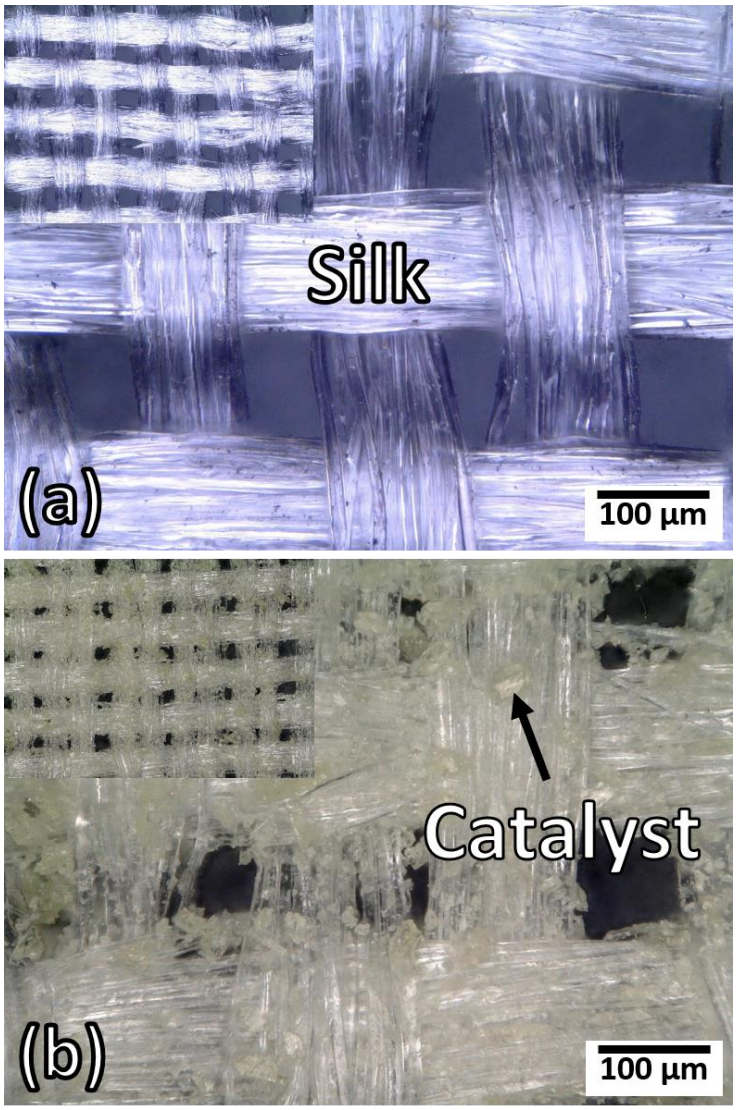

Figure 4- 1 OM images of (a) the non–catalyzed pure silk and (b) the catalyzed silk

4.3 Morphology, composition and structure of silk/Pt

Figure 4- 2 demonstrates X–ray diffraction patterns of the (a) pure silk, (b) catalyzed silk, (c) silk with reduced catalyst, and (d) metallized silk, respectively. The diffraction pattern of the pure silk in Figure 4- 2(a) shows the amorphous structure. On the other hand, all the diffraction peaks in Figure 4- 2(b) correspond well to the $Pt(acac)_2$. In Figure 4- 2(c) and (d), five diffraction peaks located at $2\theta = 40.2^{o}$, 46.7^{o}, 67.9^{o}, 81.7^{o},

and 86.1° can be indexed to (111), (200), (220), (311), and (222) planes of the FCC structure for Pt (JCPDS #87–0647). A broad peak located at around $2\theta = 20^{o}$ in Figure 4-2(c) is the contribution from the silk textile. No characteristic peak of unreduced catalyst or other impurity phases were observed within the detection limit after the Pt metallization.

The coverage tendency at 120, 160, and 200 min of the Pt metallization time durations is shown in Figure 4- 3. The bright phase corresponds to the silk, and the gray phase indicates the Pt metallization layer. In Figure 4- 3(a), the Pt metallization layer is still non–continuous, which is referred as the first stage. While the metallization time is extended to 160 min in Figure 4- 3(b), the silk textile is fully metallized. Similar morphology can be observed when the metallization time is extended to 140 min (not shown here). The silk/Pt composites with full coverage and smooth metallized surface are classified into the second stage.

When the metallization times are extended to 180 and 200 min (third stage), complete coverage can be constructed along with Pt cluster accumulations (indicated by black arrows) and rough surface (Figure 4- 3(c)). Figure 4- 3 shows that coverage of the Pt metallized layer increases as a function of the metallization time length. However, rough morphology and undesired Pt clusters deposited on the surface are observed as shown in Figure 4- 3(c), pointed by the black arrows. The roughened surface would inevitably deteriorate the electrical property (discussed below) in the third stage. On the other hand, the composition analysis results verified the as–deposited Pt layer to be pure Pt with trace impurity, which is in good agreement with the results from the X–ray diffraction pattern. Electrical conductivity of the Pt metallized silk is directly related to the coverage, which will be discussed in the 4.4 Electrical property of silk/Pt section.

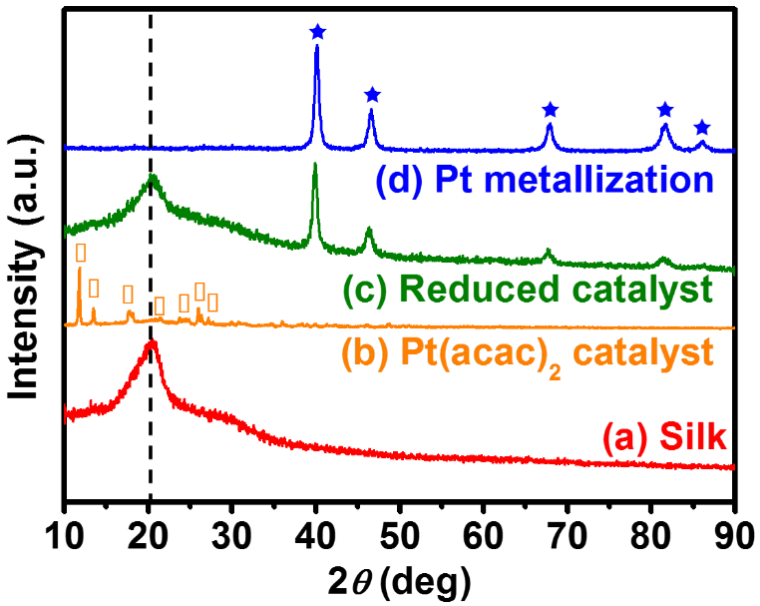

Figure 4- 2 X–ray diffraction patterns of (a) the non–catalyzed pure silk, (b) the catalyzed silk, (c) the silk with reduced catalyst, and (d) the Pt metallized silk

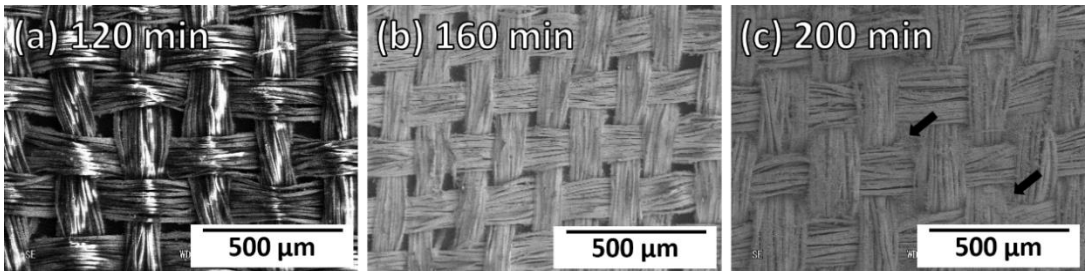

Figure 4- 3 Pt metallization trend shown by SEM images at (a) 120 min, (b) 160 min, and (c) 200 min of the Pt metallization time at 70 °C and 1 atm, respectively (black arrows in (c): Pt clusters and accumulations)

In the same way, the metallized Pt thickness grows with the metallization time length. The dependence between the metallization time duration and the thickness is presented in Figure 4- 4. The maximum Pt thickness deposited with the longest metallization time at 200 min is 0.91 µm. The standard deviation decreases with the metallization time in the first two stages suggesting better deposit homogeneity. On the contrary, the standard deviation increases as a function of the metallization time in the

third stage indicating that the homogeneity decreases as the metallization time prolongs. This can be attributed to the increased surface roughness. Reliable thickness cannot be measured when the metallization time was less than 140 min due to poor conductivity.

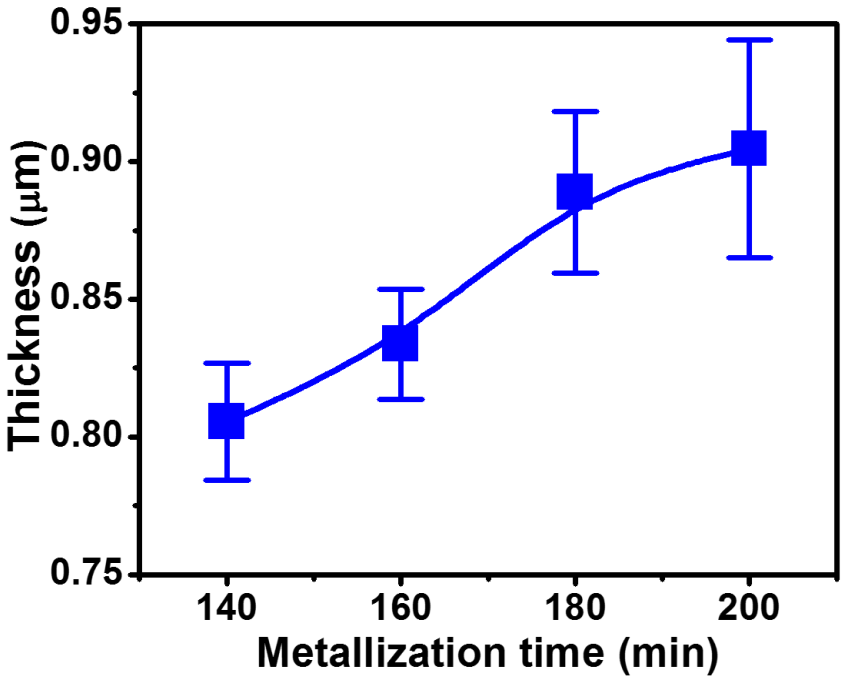

Figure 4- 4 Pt metallization layer thickness as a function of the metallization time

4.4 Electrical property of silk/Pt

The morphology (Figure 4- 3) also reflects on the electrical property. Figure 4- 5 demonstrates the electrical resistance as a function of the metallization time period. The lowest electrical resistance at 86 mΩ is obtained as the metallization time is extended to 160 min with 100% Pt coverage and smooth surface in the second stage. This result is in line with the coverage shown in Figure 4- 3 indicating that the coverage acts as a critical factor to the electrical property. On the contrary, the silk/Pt composite still remains high electrical resistance when the metallization time is less than 140 min (Figure 4- 3(a)) since the Pt layer is discontinuous in the first stage. The electrical resistances rise up in the third

stage at 180 and 200 min of the metallization time durations, which can be attributed to the rough surface. As shown in Figure 4- 3(c), the high surface roughness could bring unnecessary Joule heating and electron scattering, which are the main reasons for the deteriorated electrical resistance [89]. Therefore, 160 min is the optimized metallization time for this full Pt–contained electroless plating process.

Similarly, the standard deviation decreases with the Pt metallization time duration in the first two stages indicating that the inhomogeneity can be mitigated as the Pt metallization time extends. On the contrary, the standard deviation increases in the third stage due to the high surface roughness. Reliable electrical resistance cannot be obtained from the samples with the metallization time less than 120 min owing to the poor electrical conductivity of the silk/Pt composite materials.

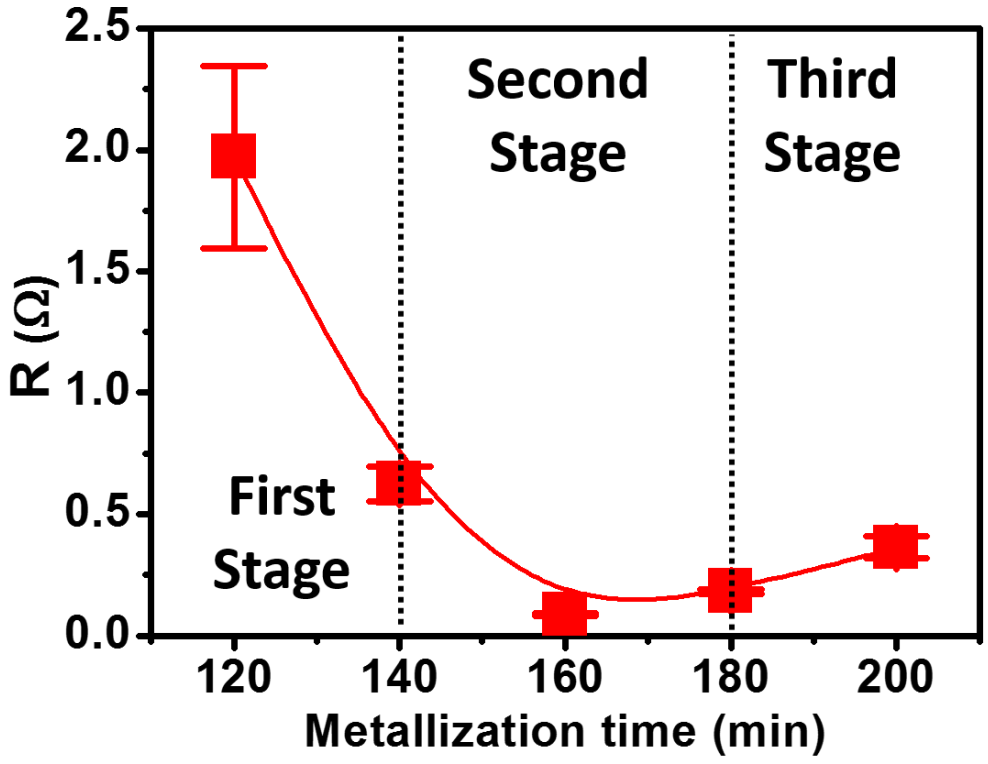

Figure 4- 5 Electrical resistance of the silk/Pt composite as a function of the metallization time at room temperature

A summary of the relationship between the morphologies of silk/Pt composite materials and their electrical resistance in different metallization stages is shown in Figure 4- 6. In the first stage, parts of the silk textile are still non–metallized resulting in a high electrical resistance. When the metallization time is extended to the second stage, the Pt metallization layer becomes continuous along with smooth Pt metallization surface leading to the lowest electrical resistance. However, in the third stage, when the Pt metallization time is beyond the optimized time, the electrical resistance is deteriorated due to the rough Pt metallization surface.

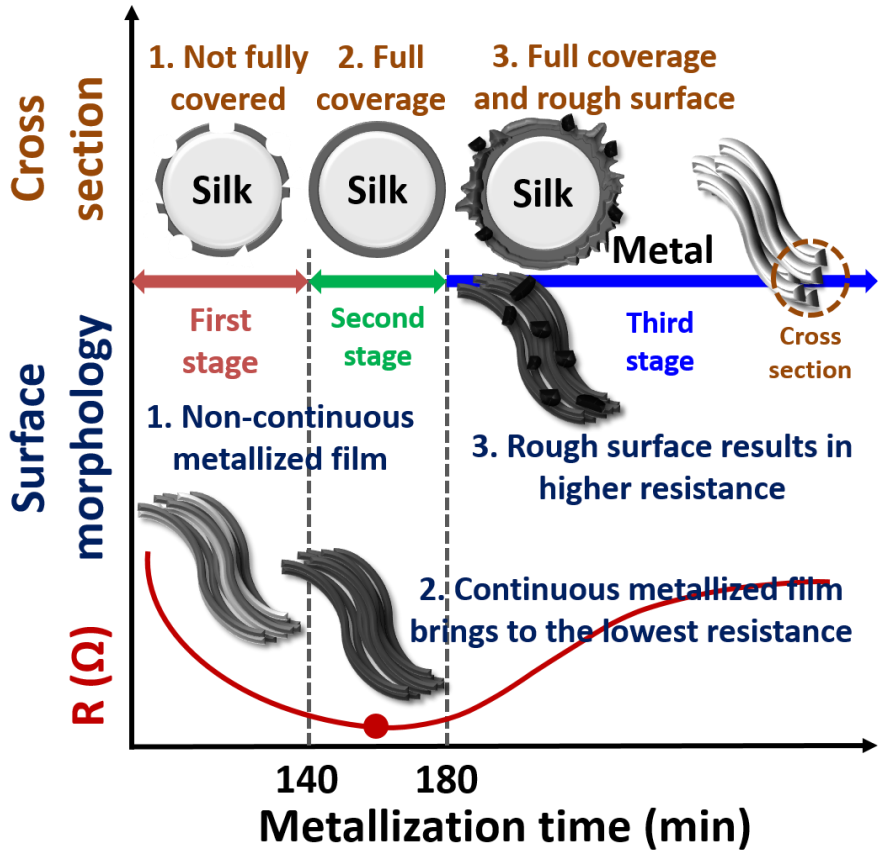

Figure 4- 6 A summary of morphology and electrical resistance of the Pt metallized silk in three different stages as well as the correlations between each properties (i.e. coverage and electrical resistance)

4.5 Biocompatibility assessments of silk/Pt

One of the key factors to trigger the allergy reaction is the ion released from the metal, and the Pt ion released from the silk/Pt composite would be the concern in this case. Therefore, examining the ion releasing rate in the SBF is a direct method to evaluate the biocompatibility of the silk/Pt composite. The Pt ion concentration in human body varies with race, environment, and diet. According to several literature based on different living conditions, the average Pt input from diet is 1.44 μg/day, and the Pt output through the faeces can be up to 1.79 μg/day [95-98]. Regarding evaluation of the ion releasing rate of the silk/Pt composite prepared in this study, only 2.73 μg of Pt was found in the SBF after 3 months of immersion at 37 ºC, which is the human body temperature. The average amount of Pt released from the silk/Pt composite per day would be around 0.03 μg, which is negligible when compared with the daily Pt input. Moreover, based on the daily Pt output, no Pt would accumulate in human body. This result provides a direct evidence that the silk/Pt composite material fabricated in the study is feasible for applications in implantable medical and wearable devices.

4.6 Brief summary for silk/Pt

The applicable Pt metallized silk textile was successfully fabricated via sc–CO_2–assisted electroless plating. Sc–CO_2 was introduced to enhance the electroless plating characteristics. This was the first study that can practice the full Pt–contained electroless plating, in other words, Pt catalyzation followed by Pt metallization. The Pt metallized silk is thus feasible to the medical and wearable devices due to the high biocompatible combination of Pt and silk. The silk textile structure persists after the catalyzation. The coverage and thickness of the Pt metallized layer increase as a function of the metallization time. The maximum thickness at 0.91 μm can be attained after metallization

for 200 minute. The metallization states can be classified into three stages according to the coverage, the morphology, and the electrical resistance. The composite material with non–continuous Pt coverage possesses high electrical resistance in the first stage. On the other hand, as the metallization time is extended to 160 min, a continuous metallized layer and smooth surface can be formed, which is within the second stage and leads to the lowest electrical resistance at 86 mΩ. Standard deviation of the electrical resistance decreases with the metallization time revealing the homogeneity increases with the metallization time length in the first two stages. The electrical resistance and the standard deviation increase again in the third stage because of the rough surface. The Pt ion releasing rate can be neglected when comparing with the daily input and output of Pt amount in human body indicating the feasibility for the applications in medical and wearable devices.

Chapter 5 Efficiency enhancement of platinum metallization on silk textile substrate by Pd(acac)$_2$ sc-CO$_2$ catalyzation

5.1 Introduction

To improve the efficiency of Pt metallization process and keep the composite materials biocompatible, catalyzation process was changed to Pd(acac)$_2$ catalyst instead of Pt(acac)$_2$ (4.2 Activation of silk textile via sc–CO2 Pt(acac)$_2$ catalyzation section). Moreover, the process working with Pd(acac)$_2$ also show lower cost while compared to the Pt(acac)$_2$ one. Similar biocompatibility assessments were done in this section to evaluate the biocompatibility of the composite materials. Mechanisms of the influences from the Pd(acac)$_2$ catalysts in the metallization step were also discussed in the following sections.

5.2 Activation of silk textile via sc–CO$_2$ Pd(acac)$_2$ catalyzation

Figure 5- 1 shows OM images of the non–treated pure silk, catalyzed silk, and catalyzed silk with reduction treatment. Transparent thread bundles shown in Figure 5- 1(a) indicate the silk textile, light yellow flakes shown in Figure 5- 1(b) correspond to Pd(acac)$_2$ catalysts, and the small particles with metallic luster shown in Figure 5- 1(c) are the reduced Pd metallic particles. As shown in Figure 5- 1(b), the Pd(acac)$_2$ catalysts are successfully settled on the substrate without damaging the structure of silk substrate. After the reduction, small Pd metallic particles finely remained on the substrate shown in Figure 5- 1(c).

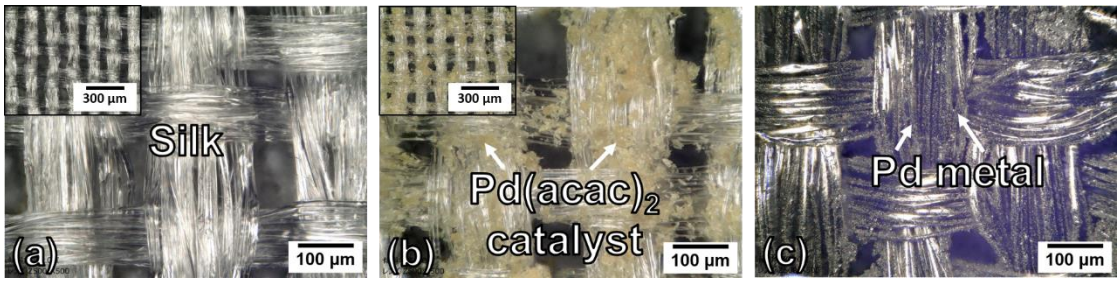

Figure 5- 1 OM images of (a) non–treated pure silk, (b) sc–CO_2–assisted $Pd(acac)_2$ catalyzed silk, and (c) catalyzed silk with reduction treatment

X–ray diffraction patterns of the (a) pure silk, (b) catalyzed silk, and (c) catalyzed silk with reduction treatment are shown in Figure 5- 2. The pure silk shows one broad peak at around $2\theta = 20^{o}$ in Figure 5- 2(a). On the other hand, after the catalyzation, all the X–ray diffraction characteristic peaks can be indexed to the contribution from $Pd(acac)_2$ [82, 83], shown in Figure 5- 2(b). Figure 5- 2(c) shows X–ray diffraction pattern of the reduced catalyst on silk. Four diffraction peaks at $2\theta = 40.1^{o}$, 46.7^{o}, 68.1^{o}, and 82.1^{o} can be indexed to (111), (200), (220), and (311) planes of the FCC structure of palladium (JCPDS #89–4897).

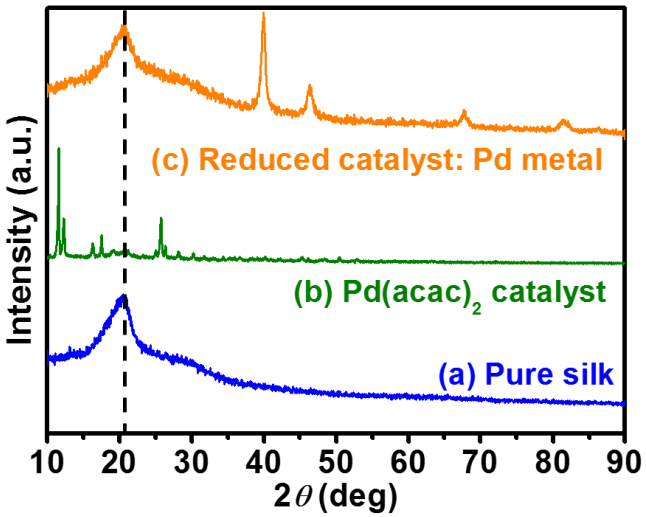

Figure 5- 2 X–ray diffraction patterns of (a) non–treated pure silk, (b) silk with sc–CO_2 catalyzation treatment, and (c) catalyzed silk with the reduction treatment

The broad peak observed at 2θ = 20° in the X–ray diffraction pattern indicates the amorphous structure of silk textile as shown in Figure 5- 2. With the introduction of sc–CO_2, its nonpolar and low viscosity bring the catalysts into the substrate without damaging the substrate structure. The OM image (Figure 3- 1(c)) along with the characteristic peaks in Figure 5- 2(b) reveal that the catalyst was successfully settled on the substrate. Due to the high intensity from the $Pd(acac)_2$ catalysts, the broad peak from silk was suppressed and was not observed in Figure 5- 2(b). According to H. Vrubel et al. [99] and D. A. P. Tanaka et al. [100], the reduction reaction of $Pd(acac)_2$ is believed to be the reactions listed in the following equations:

$$Pd(C_5H_7O_2)_2 + 2N_2H_4 = Pd^{2+} + 2C_5H_8N_2 + 2OH^- + 2H_2O \quad (5.\ 1)$$

where $Pd(C_5H_7O_2)_2 = Pd(acac)_2$

$$Pd^{2+} + N_2H_4 + 4OH^- = 2Pd + N_2 + 4H_2O \quad (5.\ 2)$$

The broad peak at around 2θ = 20° in Figure 5- 2(c) is attributed to the amorphous silk substrate and the sharp peaks indicate successful reduction of the $Pd(acac)_2$ to form Pd metal. Results of Figure 5- 2(a–c) are in good agreement with Figure 3- 1(a) and (c). The reduced catalysts can be used as the active sites for the deposition of Pt metals in the following metallization step.

5.3 Morphology, composition and structure of silk/Pt

Three SEM images shown in Figure 5- 3 demonstrate a trend of coverage of the Pt layer on the silk with various metallization times. Figure 5- 3(a) shows a SEM image of the sample with 80 min of the metallization time, where the bright phase corresponds to non–metallized silk while the gray phase indicates Pt metal. Since the electron cannot be conveyed on the non–conductive silk, thus the electrons accumulate on the non–

metallized silk would show the charging effect. At 80 min of the metallization time, some parts of silk textile were non–metallized (pointed by arrows) showing a non–continuous Pt layer and a smooth surface on the metallized part. Figure 5- 3(b) shows morphology of the sample with 120 min of the metallization time, a continuous Pt metallized layer was constructed showing gray color thoroughly and the surface remained smooth. When the metallization time was extended to 180 min (Figure 5- 3(c)), the silk substrate was also completely covered. However, undesired Pt clusters accumulated on the surface, and the metallized surface became rough (pointed by arrows). Similar phenomenon was observed in previous sections.

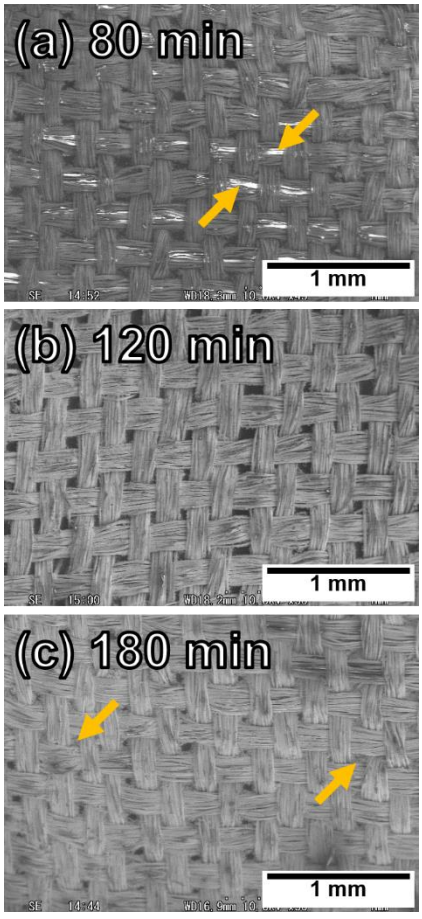

Figure 5- 3 Pt metallization trend demonstrated by SEM images at (a) 80 min, (b) 120 min, and (c) 180 min of the Pt metallization times

In the same way, elemental mapping of the Pt metallized silk (Figure 5- 4) shows the critical time demarcation of full coverage, which lies between (a) 80 and (b) 100 min of the metallization time. The least time needed to construct full coverage is defined as the minimum time, which is 100 min. The composition results show pure Pt layer with merely trace amount of impurity.

Figure 5- 5 shows the X–ray diffraction pattern after the Pt metallization. Five diffraction peaks located at 2θ = 40.2°, 46.8°, 68.4°, 82.4°, and 86.9° can be indexed to (111), (200), (220), (311), and (222) planes of the FCC structure of platinum (JCPDS #87–0647).

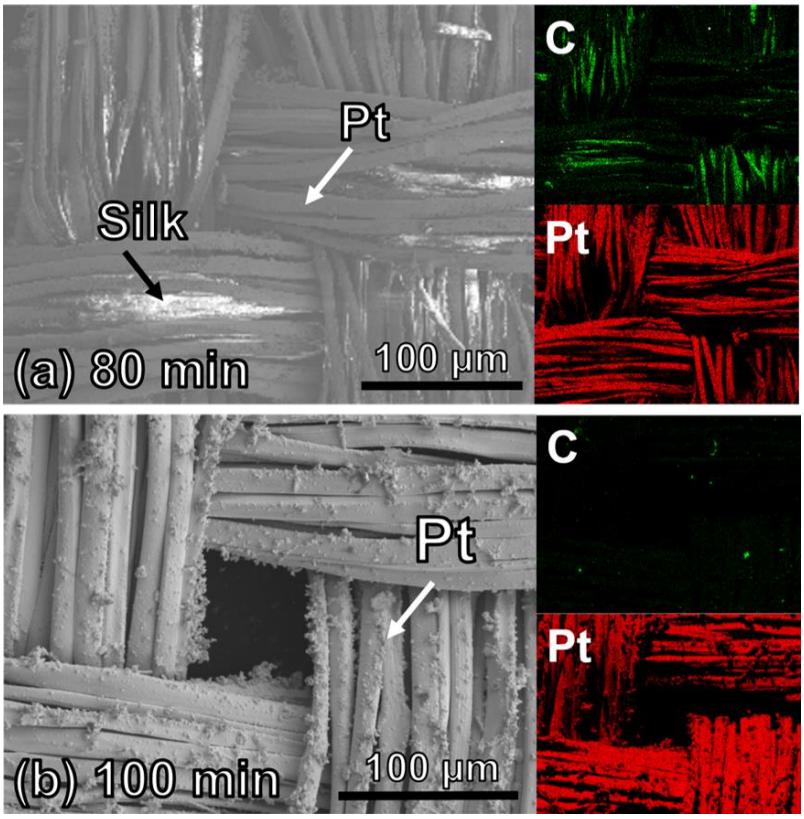

Figure 5- 4 Elemental mapping of Pt metallized silks at (a) 80 min and (b) 100 min of the Pt metallization time (set at upper–right figures: carbon signals; set at bottom–right figures: carbon signals)

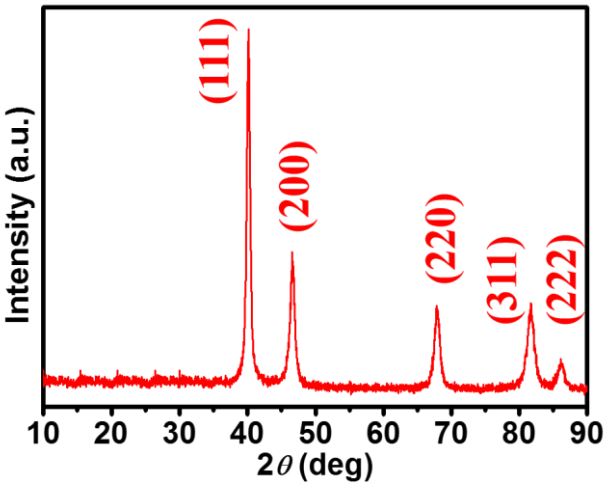

Figure 5- 5 X–ray diffraction pattern of Pt metallized silk substrate

The metallization time dependence of the Pt layer thickness is presented in Figure 5- 6. A positive correlation between the metallization time and the thickness is shown. A reliable thickness value could not be measured for the samples with a metallization time less than the minimum time at 100 min due to the poor electrical conductivity. Pt layer thickness at 0.90 μm was obtained with the longest metallization time at 180 min, which the calculated average growth rate is 1.8 nm/min.

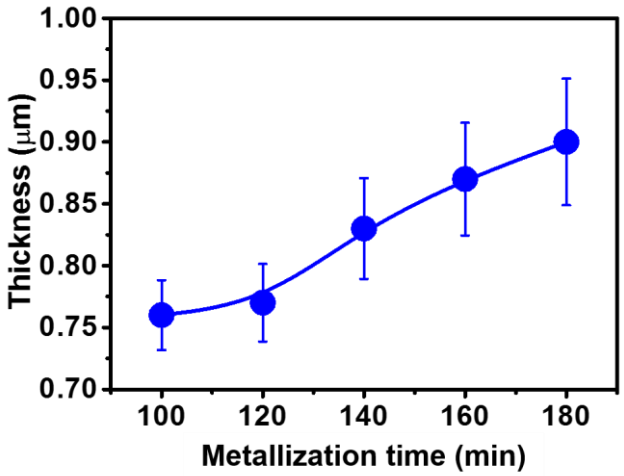

Figure 5- 6 Pt layer thickness on silk substrate as a function of the metallization time

5.4 Electrical property of silk/Pt

Figure 5- 7 illustrates the electrical resistance as a function of the metallization time before and after the adhesion test. Again, a reliable electrical resistance cannot be obtained owing to the poor electrical conductivity when the Pt metallization time is less than 80 min. The electrical resistance was high in the early stage of the Pt metallization and then decreased with an increasing in the Pt metallization time. After reaching a minimum point at 120 min, the electrical resistance gradually increased and stabilized.

The electrical resistances of the silk/Pt composite materials after the adhesion test are shown in Figure 5- 7. The adhesion tests showed serious impact on the samples in the early stage. On the contrary, the electrical resistances of the composites persist after the second adhesion test in the last two stages. In addition, there is no distinct difference between the first and the second adhesion test. The stages can be classified into three according to the morphology and the electrical resistance, which will be discussed in the following section.

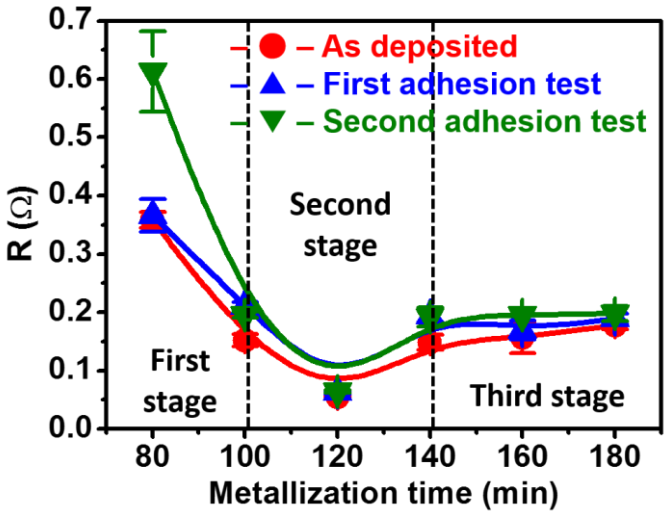

Figure 5- 7 Electrical resistance curves as a function of metallization time of the silk/Pt composites before and after the adhesion tests

Based on the coverage, surface roughness, and electrical resistance, the Pt metallization of silk substrates are classified into three stages. The partially metallized silk with a discontinuous Pt layer at 80 min of the metallization is classified to the first stage (Figure 5- 3(a)). The partly metallized surface showed smooth morphology since the metallization is still in the early stage. In this stage, the electrical resistance remained high due to the discontinuous Pt layer. At 120 min of the metallization time (Figure 5-3(b)), the silk substrate was fully covered with Pt, which is classified into the second stage. Electrical resistance was lowered since continuous Pt layer was constructed. The metallized surface was smooth, and there was not much redundant clusters on the Pt layer. Hence, the lowest electrical resistance at 55 mΩ was built up in the second stage at the optimal metallization time of 120 min. At 180 min of the metallization time (Figure 5-3(c)), the silk was still fully covered; however, undesired Pt clusters and the rough metallization resulted in the elevated electrical resistance. The rough Pt deposition on the substrate surface increased unnecessary Joule heating and caused formation of a relative loose structure. SEM images revealing an increase in the roughness as the metallization time increased are shown in Figure 5- 8. A proportional relationship between the electrical resistance and the roughness is indicated in the literature [90]. Therefore, coverage of the Pt layer and the surface roughness both have significant influence on the electrical resistance.

The influence of morphology on the electrical resistance in different stages is illustrated in Figure 5- 9. In the first stage, the silk was not fully metallized showing a non–continuous Pt layer. It thus gave the highest electrical resistance. When the metallization time was prolonged to the second stage, full coverage was constructed showing a continuous Pt layer. Along with the smooth surface, the electrical resistance

reached its minimum point at 120 min in the second stage. However, rough surface emerged as the metallization time extended; the electrical conductivity was thus deteriorated in the third stage.

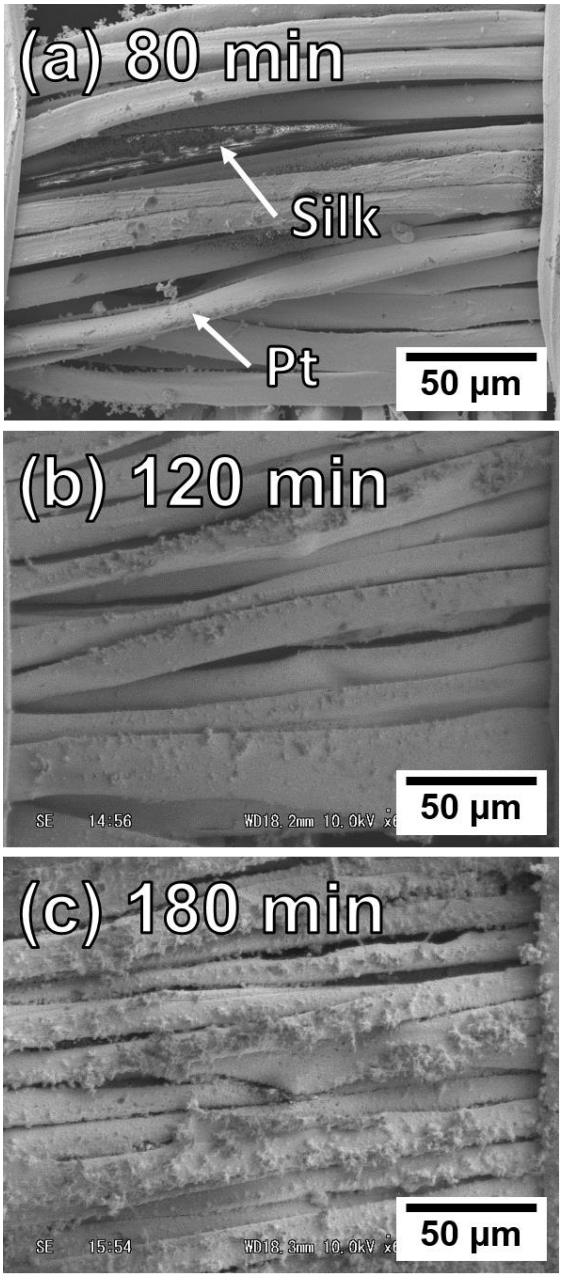

Figure 5- 8 SEM images showing surface conditions of the silk/Pt composites prepared by (a) 80 min, (b) 120 min, and (c) 180 min of the metallization time (metallization temperature: 70 ºC; metallization pressure: 1 atm; with agitation)

In the electrical resistance test, the electrical resistance is expected to be elevated if the adhesion test successfully introduces defects into the Pt layer due to an increase in surface roughness of the Pt layer. The results shown in Figure 5- 7 indicate great impacts in the first stage, on the contrary, the electrical resistance persists in the final two stages. In the first stage, the Pt layer is not continuous and the edge of the Pt layer exposes to the tape during the adhesion tests. The Pt edge would be peeled off more easily than the surface that is fully metallized since it is free from support in the edge. The silk metallized with the optimized time shows perseverance in the second adhesion test indicating its feasibility in the practice of applications even when under adverse conditions.

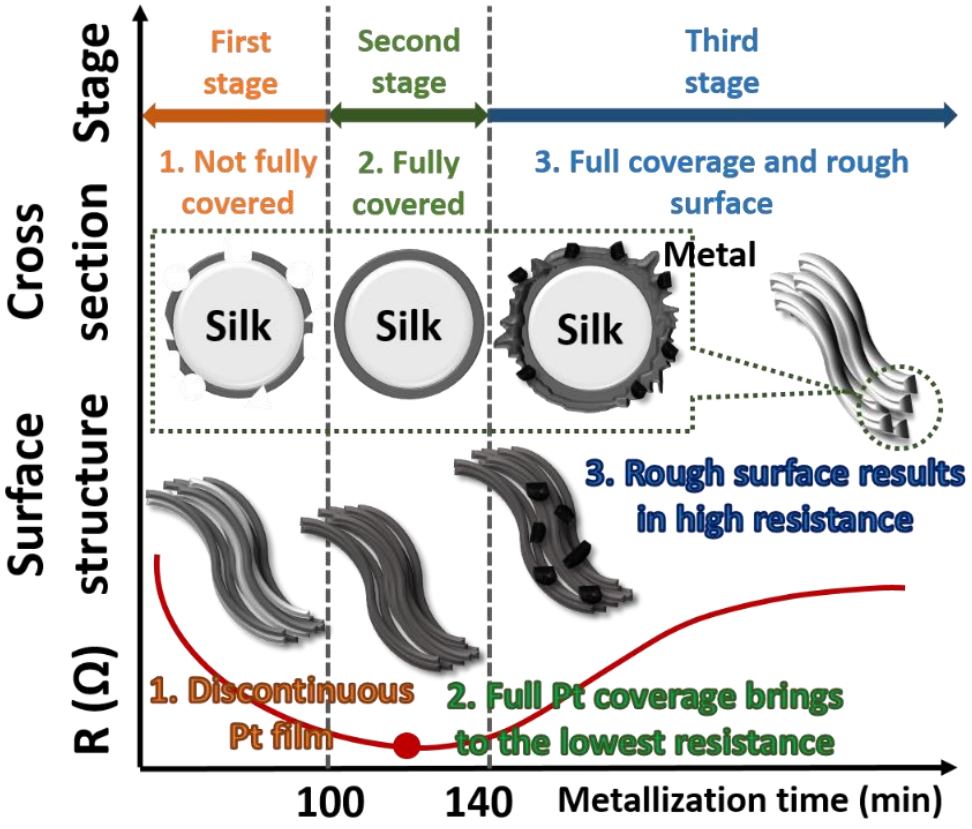

Figure 5- 9 The relationship between Pt metallization morphology and electrical resistance as well as the cross–section morphologies in three different stages

5.5 Corrosion resistance of silk/Pt

Figure 5- 10(a) shows results of the polarization measurements of the silk/Pt composite materials before and after the adhesion test. The silk substrate with 120 min of the metallization time was chosen for the corrosion resistance evaluation. No significant difference was found among the three polarization curves indicating excellent corrosion resistance of the Pt layer even after the second adhesion test. The E_{corr} and I_{corr} are summarized in Table 5- 1(a). Moreover, Figure 5- 10(b) shows the morphology after the second adhesion test and the polarization measurement. No obvious corrosion attack was found after the adhesion test and the polarization test in 3.5 wt.% NaCl solution. For simulating the condition in the human body, similar polarization measurements were carried out in the SBF and the results are shown in the following.

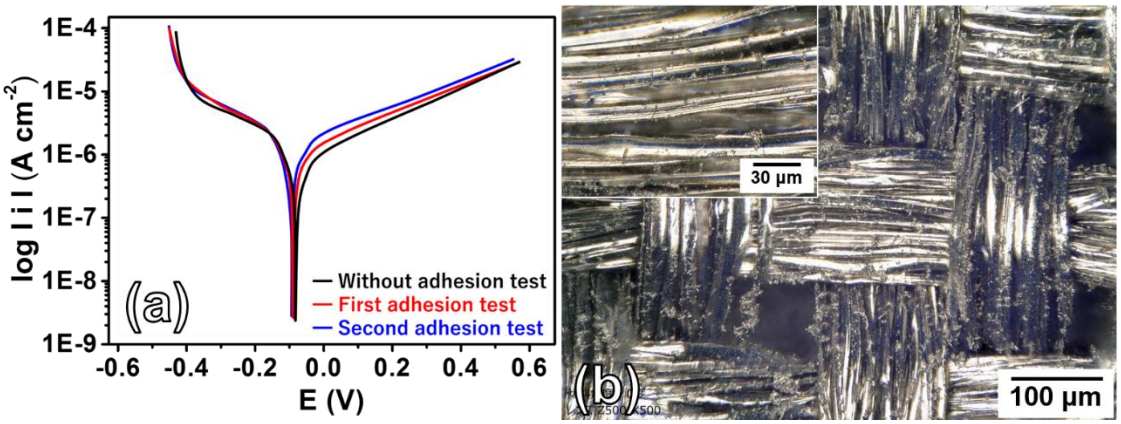

Figure 5- 10 (a) Polarization measurements of the silk/Pt composites before and after the adhesion tests in 3.5 wt.% NaCl solution at room temperature and 1 atm without agitation and (b) OM image of the silk/Pt composite after second adhesive test and polarization measurement

Figure 5- 11(a) shows the polarization curves of the silk–Pt composite materials before and after the adhesion test. In the same way, metallization time at 120 min was

chosen for its best suitability to this application. The corrosion resistance also persisted after the second adhesion test, no significant difference within these three polarization curves was observed. The E_{corr} and I_{corr} are also summarized in Table 5- 1(b). The morphology after the second adhesion test and polarization measurement is shown in Figure 5- 11(b). Similarly, no obvious corrosion attack was inspected after adhesion test and the corrosion test in the SBF solution.

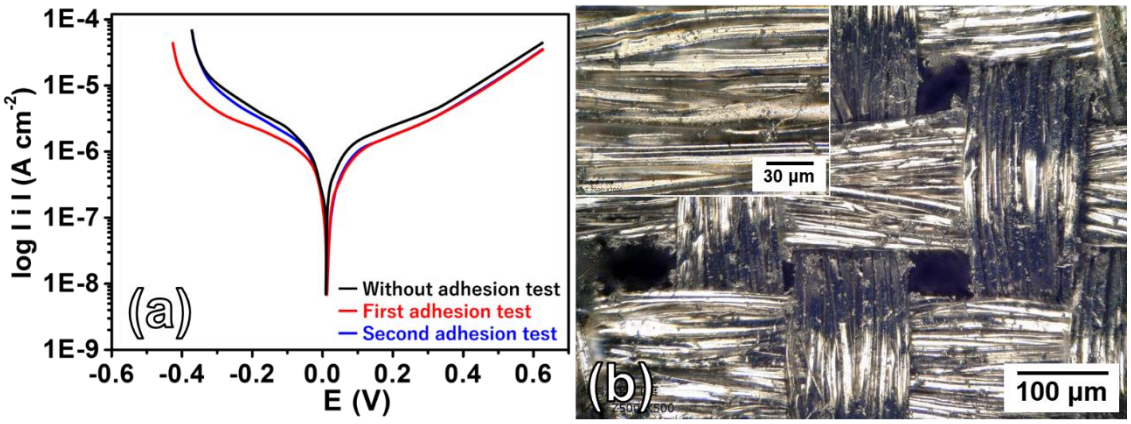

Figure 5- 11 (a) Polarization measurements of the silk/Pt composites before and after the adhesion tests in SBF solution at room temperature and 1 atm without agitation and (b) OM image of the silk/Pt composite after second adhesive test and polarization measurement

In 3.5 wt.% NaCl solution, high corrosion resistance of the silk/Pt is shown in the polarization measurements in Figure 5- 10(a), and limited corrosion attacks on the sample surface are revealed in Figure 5- 10(b). On the other hand, the corrosion current densities of the composite materials in the SBF are all lower than those in 3.5 wt. % NaCl solution since 3.5 wt. % NaCl solution contains more Cl^-, and Cl^- has significant impact on corrosion resistance of metals [95]. The corrosion potential of silk/Pt composite in the SBF is also more positive than those in 3.5 wt. % NaCl solution indicating that the Pt

layer is more inert in the SBF solution. Despite the fact that thin Pt layer was electroless plated on the non–conductive substrates, the corrosion rates are comparable to those of Pt metal, which indicates the well deposition of Pt layer on the silk. Overall, the silk/Pt composites show high corrosion resistances in the two solutions. These results suggest that the silk/Pt composite is not merely practical in wearable devices but also in implantable devices.

Table 5- 1 Corrosion potentials and corrosion currents of the silk/Pt composite materials in (a) 3.5 wt.% NaCl and (b) SBF solutions measuring at room temperature and 1 atm

(a) Samples (in 3.5 wt.% NaCl)	E_{corr} (V)	I_{corr} (A/cm^2)
As–deposited	-0.090	3.58×10^{-7}
First adhesive test	-0.092	3.50×10^{-7}
Second adhesive test	-0.093	3.56×10^{-7}
(b) Samples (in SBF)	E_{corr} (V)	I_{corr} (A/cm^2)
As–deposited	0.015	2.16×10^{-7}
First adhesive test	0.018	2.02×10^{-7}
Second adhesive test	0.019	2.02×10^{-7}

The levels of damage severity from the adhesion test were evaluated by both corrosion and electrical resistance measurements. Generally, defects and cracks would be formed after the adhesion test. Then the corrosion test solution can penetrate into the defects and cracks to give an increase in the current during the polarization measurement. Since the surface area is assumed to be constant, the current density is thus expected to be increased after formation of the defects and cracks. However, no significant difference in the corrosion current density was found after the adhesion test indicating that the samples stay intact after the adhesion test and hence shows the high adhesive property of the Pt layer on the silk.

5.6 Biocompatibility assessment of silk/Pt by immersion test

Releasing of the metal ions is an essential factor to provoke the allergy reactions [101], therefore, investigating released ion concentration in the SBF is a direct way to evaluate biocompatibility of the silk/Pt composite. After three months of the immersion at human body temperature (37 ºC) in the SBF, only 0.011 μg/day and 0.018 μg/day of Pd and Pt were observed, respectively.

The metal ion concentration in human body varies with races, environments, and diets. According to several literature based on different living conditions, average Pt input from diet is 1.44 μg/day, and Pt output through the faeces can be up to 1.79 μg/day [95-98]. On the other hand, the average Pd intake is 2 μg/day, and the Pd output can be up to 2.5 μg/day [102, 103]. From the immersion test, only 0.018 μg Pt/day and 0.011 μg Pd/day were observed in the SBF solution. Both values are far less than the intake and have no chance to accumulate in the human body according to the literature and the ICP results. In addition, the Pt ion releasing rate of the silk/Pt composite prepared in this study is lower than those catalyzed by the $Pt(acac)_2$ (4.5 Biocompatibility assessments of silk/Pt section). Since the samples catalyzed by $Pd(acac)_2$ shows relative smooth deposition and less defects (Figure 5- 12), it is thus corroded mildly in the immersion tests while comparing to those catalyzed by $Pt(acac)_2$.

5.7 Enhancement of the metallization efficiency

The electroless plating system catalyzed by $Pd(acac)_2$ demonstrates a more efficient process and improved material properties than those catalyzed by $Pt(acac)_2$ (4.2 Activation of silk textile via sc–CO2 $Pt(acac)_2$ catalyzation section). In this study, the optimal metallization time needed to reach the lowest electrical resistance is at 120 min,

which shows 25% reduction in the time when comparing to the study using $Pt(acac)_2$ as the catalyst. The improved efficiency is suggested to be attributed to the high reduction efficiency of $Pd(acac)_2$ to Pd metal. According to the literature [104], $Pd(acac)_2$ owns a lower decomposition temperature than that of $Pt(acac)_2$, it thus can be decomposed or reduced to metal state more efficiently. After formation of the activation sites and gradual deposition of the Pt layer on the silk surface, the catalysts would be fully covered by the Pt and have no significant influence on the succeeding Pt deposition rate.

It is worth to mention that the silk/Pt composite materials fabricated in this study showed electrical resistances 36% lower than those in 4.4 Electrical property of silk/Pt section. When comparing with reduction of $Pd(acac)_2$ to Pd metals, reduction of $Pt(acac)_2$ to Pt metals is less efficient and takes longer time. The non–synchronize $Pt(acac)_2$ reduction leads to uneven growth of the Pt activation sites and the Pt metallization later on. The irregular sizes of Pt activation sites make the succeeding Pt deposition to grow roughly and thus shows the high electrical resistance. The decomposition temperature of $Pt(acac)_2$ is higher than those of $Pd(acac)_2$ [104], which is an evident showing that the bonding between Pt and $(C_5H_7O_2)_2$ is stronger than those of Pd and $(C_5H_7O_2)_2$. It takes time for $Pt(acac)_2$ to be reduced to Pt metallic particles and therefore it shows non–synchronize reduction. The relationship between the metallization time and the Pt layer roughness is shown in Figure 5- 12. Rough Pt cross–section shown in Figure 5- 12(a) was catalyzed by $Pt(acac)_2$; while, the smooth one in Figure 5- 12(b) was catalyzed by $Pd(acac)_2$. By using $Pd(acac)_2$, nucleation and growth of the activation site would be uniform and lead to even growth of the Pt layer. Hence, the electrical resistance could be lowered.

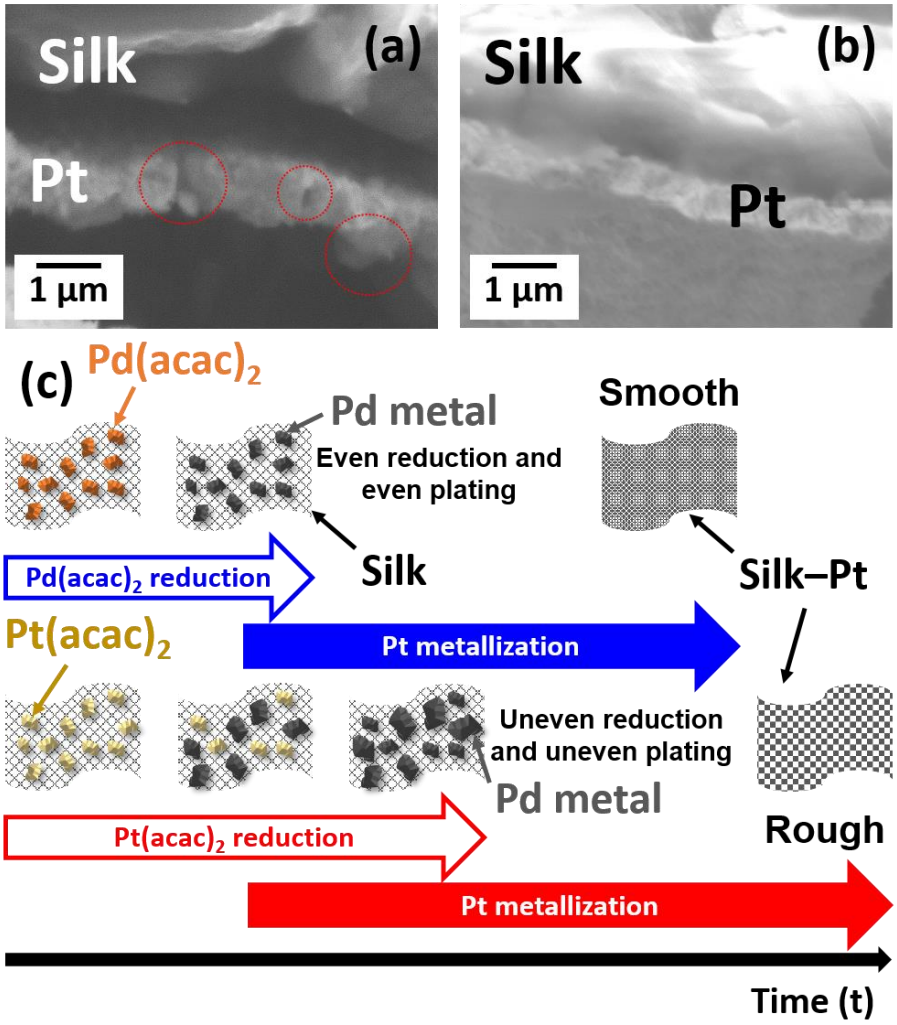

Figure 5- 12 Cross–sections of (a) Pt catalyzation followed by Pt metallization, (b) Pd catalyzation followed by Pt metallization, and (c) illustration of the influence of different catalysts on the smoothness of Pt layer

5.8 Brief summary for silk/Pt

The Pt metallized silk was successfully fabricated from the electroless plating promoted by sc–CO_2 in this study. In the catalyzation step, $Pd(acac)_2$ catalyst was successfully settled on the silk substrate without damaging the structure due to the introduction of sc–CO_2. The coverage and thickness of the Pt layer increased as a function of the metallization time. Silk textile was fully covered at 100 min of the metallization

time, which is the minimum time to achieve full coverage. A maximum thickness of 0.90 μm was obtained at 180 min of the metallization time, which the average growth rate is 1.8 nm/min. The Pt metallization is classified into three stages. In the first stage, non–continuous Pt layer on the silk remained high electrical resistance. On the other hand, the lowest electrical resistance and full coverage were achieved in the second stage. In the end, rough surface was deposited in the third stage resulting in deteriorated electrical conductivity. Pt metallized silk showed high corrosion resistance in both 3.5wt. % NaCl and the SBF solutions. Average Pd and Pt ion releasing rates in the SBF were 0.011 μg/day and 0.018 μg/day, respectively, which are negligible when comparing with the daily input and output of Pd and Pt of human body. The lowest electrical resistance at 55 mΩ was reached at the optimal metallization time of 120 min. Strong adhesion of the Pt layer on the silk was revealed by both corrosion test and electrical resistance measurement after the adhesion test. The results indicate the feasibility of this material for medical and wearable devices.

Chapter 6 Full sc-CO_2 promoted platinum electroless plating for enhancing the electrical conductivity and reliability of the silk/Pt composite materials

6.1 Introduction

There are two steps of electroless plating, the first step is catalyzation step to embed the catalyst into the substrate making it active and the second step is the metallization to metallize the substrate equipping it with electrical conductivity. Sc–CO_2 cannot only be applied to the catalyzation step, but also can be applied to the metallization procedure. In the previous three sections, sc-CO_2 was only introduced into the catalyzation step. On the other hand, in this section, sc–CO_2 is introduced into the metallization step to further enhance the metallization properties. A non-ionic surfactant is introduced into the aqueous metallization bath in the meanwhile (Figure 6- 1) to emulsify the aqueous electrolyte bath and form sc–CO_2/surfactant micelles [105]. With the help of sc–CO_2/surfactant micelles, it can carry the hydrogen bubbles away from the substrate due to its non–polarity and high self–diffusivity. The metallization layer turns out to be compact and smooth by elimination of the hydrogen bubbles and the electrical conductivity was also enhanced accordingly. Therefore, a sc–CO_2–assisted method was introduced into the metallization process in this section to enhance the properties of the metal film and solve the difficulties in the CONV metallization.

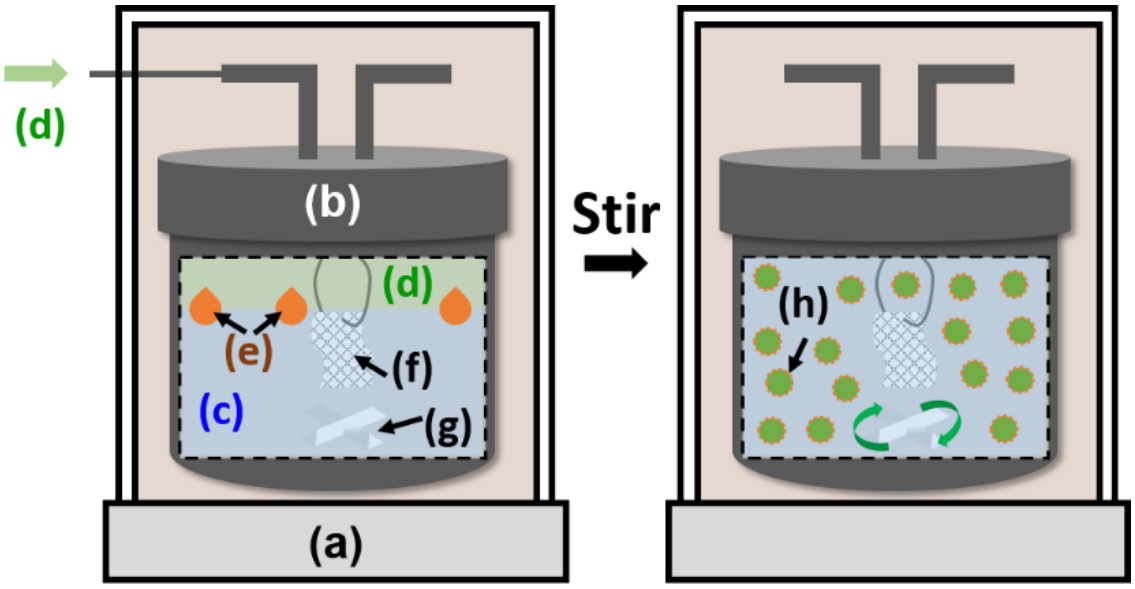

Figure 6- 1 Experimental settings of the sc–CO_2 assisted metallization step: (a) A thermal bath that is controlled by an isothermal furnace, (b) the reaction–cell (PEEK–lined SUS316L), (c) Pt metallization electrolyte (80 vol.%), (d) sc–CO_2 (19.8 vol.%), (e) non–ionic surfactant (0.2 vol.%), (f) silk textile, and (g) cross stirrer, and (h) sc–CO_2/surfactant micelles formed when the solution is stirred in the reaction cell

6.2 Activation of silk textile via sc–CO_2 $Pd(acac)_2$ catalyzation

Figure 6- 2 shows the (a) as–received silk and (b) sc–CO_2 catalyzation–treated silk. Transparent thread bundles and light yellow flakes seen in the OM images indicate the silk substrate and $Pd(acac)_2$, respectively. With the help of sc–CO_2 in the catalyzation step, the $Pd(acac)_2$ was successfully inlaid into the silk substrate without damaging the silk structure (Figure 6- 2(b)).

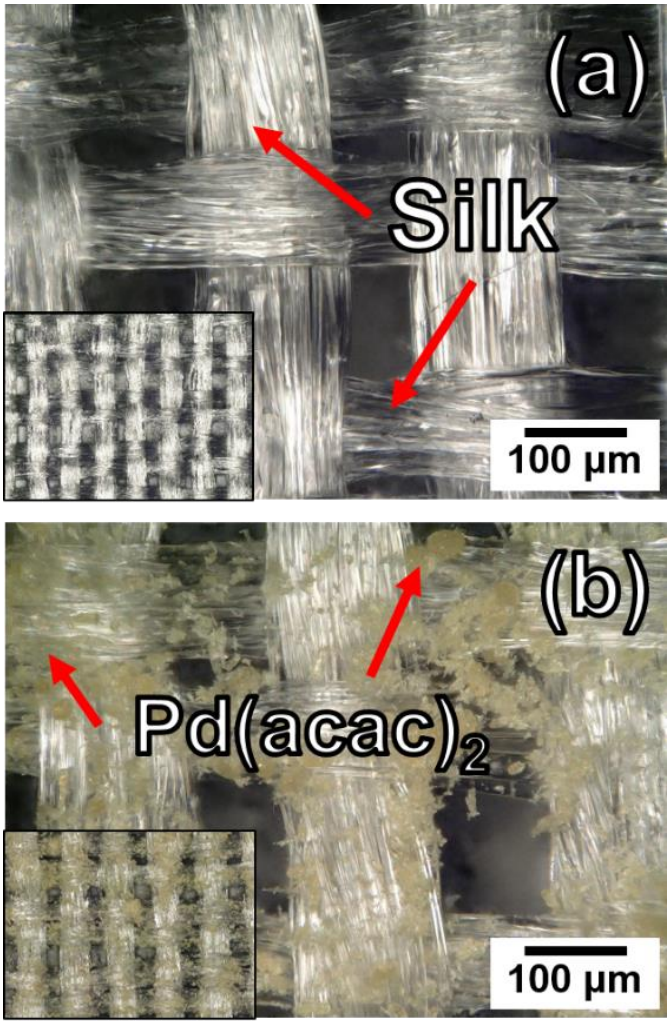

Figure 6- 2 OM images of the (a) as–received and (b) sc–CO_2 catalyzed silks

6.3 Morphology, composition, and structure of sc–CO_2 metallized silk/Pt

X–ray diffraction patterns of the (a) as–received silk, (b) sc–CO_2 catalyzation–treated silk, and (c) Pt metallized silk are shown in Figure 6- 3. Silk textiles in Figure 6-3(a) shows one broad peak at around $2\theta = 20^{o}$ indicating the amorphous structure of the substrate. After the catalyzation, all the diffraction peaks in Figure 6- 3(b) can be indexed to $Pd(acac)_2$ (diamond symbol) well suggesting the $Pd(acac)_2$ was successfully deposited. X–ray diffraction pattern of the Pt metallized silk is demonstrated in Figure 6- 3(c), five diffraction peaks locating at $2\theta = 40.2^{o}$, 46.8^{o}, 68.4^{o}, 82.4^{o}, and 84.5^{o} can be indexed to

(111), (200), (220), (311), and (222) planes of the FCC structure for platinum (circle) (JCPDS #87–0647), respectively. This result indicates that metallic platinum phase was deposited with only trace amount of impurity, and no other phases were observed as well within the X–ray detection limitation. Due to the small amount of reduced Pd metal catalyst, no metallic Pd characteristic peaks were observed after the metallization step.

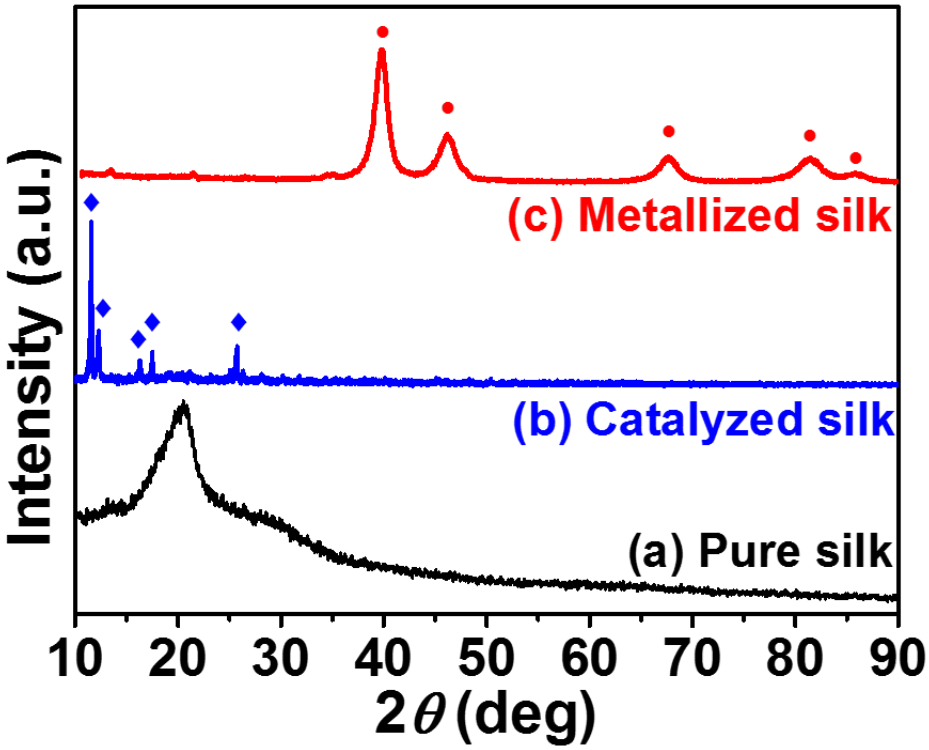

Figure 6- 3 X–ray diffraction patterns of the (a) as–received, (b) sc–CO_2–assisted $Pd(acac)_2$ catalyzation treated, and (c) Pt metallized silks (blue diamond: $Pd(acac)_2$ catalysts; red circle: Pt)

Figure 6- 4 shows diffraction patterns of the Pt metallized silk by the (a) CONV method and (b) the sc–CO_2–assisted metallization technique. In Figure 6- 4, full width at half maximums of the diffraction peaks of the Pt layer fabricated by the sc–CO_2–assisted technique were clearly wider than those prepared by the CONV method indicating that the sc–CO_2–assisted metallization brings a finer grain size.

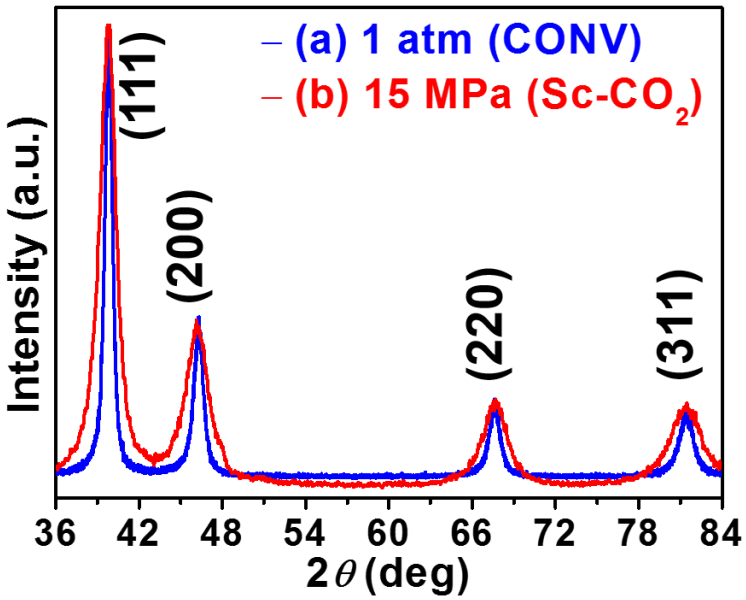

Figure 6- 4 X–ray diffraction patterns of Pt metallized silks by the (a) CONV at 1 atm, and (b) sc–CO_2–assisted metallization methods

Influence of the sc–CO_2 on the grain size is shown in Figure 6- 5. In the CONV metallization, concentration of Pt complex around the electrode surface is similar to the concentration in the bulk solution and Pt nucleated on the substrate surface in early stage of the metallization as shown in Figure 6- 5(a). As the metallization proceeds (Figure 6- 5(b)), concentration of the Pt complex around the substrate surface gradually decreases, which favors grain growth instead of nucleation. On the other hand, micelles composed of surfactant and sc–CO_2 would repeatedly bounce on the substrate surface to promote mixing of reactive species in the solution (Figure 6- 5(d)). In this case, transfer or diffusion of Pt complex from the bulk solution to surface of the substrate is enhanced and leads to a higher Pt complex concentration near the substrate than that in the CONV metallization as shown in Figure 6- 5(e). When concentration of the reactive species, the Pt complex in this case, is high, nucleation is favored instead of grain growth, thus, high nuclei density and fine grain size are obtained Figure 6- 5(c) and (f)). In addition, high

nuclei density also brings about the smooth surface due to even growth rate of the Pt metallization layer on entire surface of the substrate. Since no obvious difference in ratio of the X–ray diffraction peak intensities was found between the CONV and the sc–CO_2–assisted metallization method, the sc–CO_2 is suggested to have no influence on preferred crystal orientation of the Pt. Influence of the grain size on properties of the silk–Pt composites will be discussed in the following.

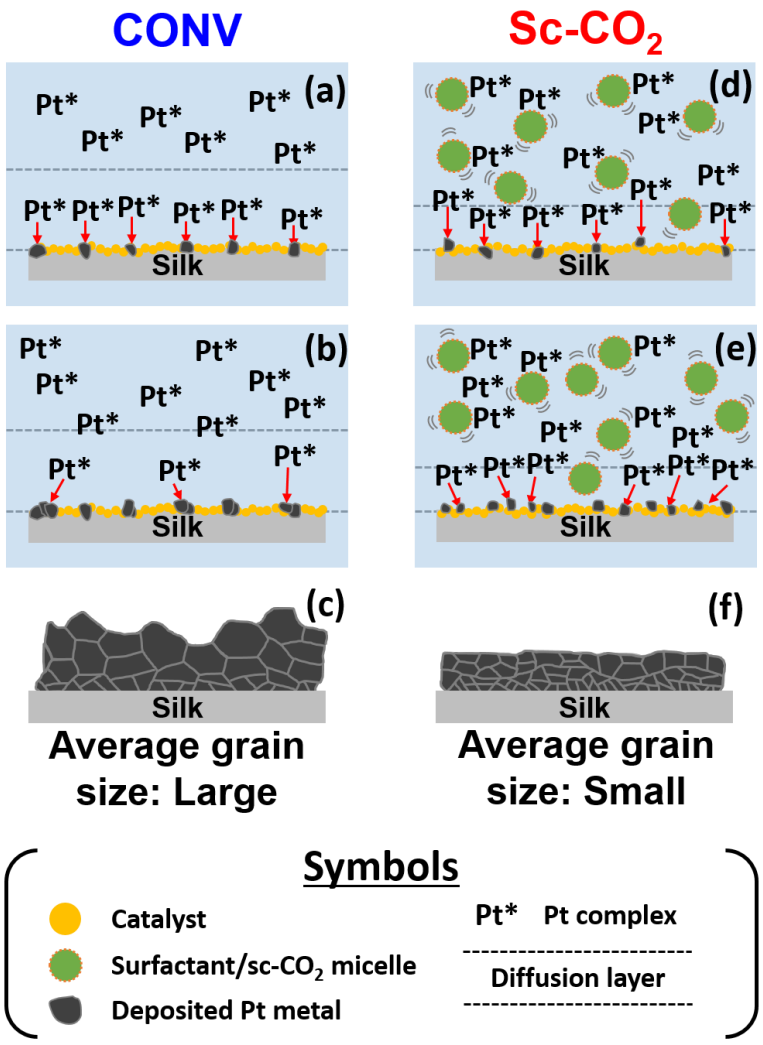

Figure 6- 5 Illustration of influences of sc–CO_2 in the metallization step: (a–c) CONV and (d–f) sc–CO_2–assisted metallization methods

Six SEM images of silk–Pt composites metallized at 10, 20, 60, 100, and 140 min are shown in Figure 6- 6(a–e) to demonstrate the Pt coverage trend. Figure 6- 6(a) reveals surface condition of the silk substrate metallized for only 10 min, and the dark phase is the Pt metallized region. Composition of the dark phase is pure Pt phase with only limited impurities. The bright phase corresponds to the silk, since silk is a non–conductive material which shows charging effect under SEM observation. Some parts of the silk are still non–metallized (pointing by arrows) indicating the Pt metallization layer is not continuous on the silk.

Depending on the coverage condition of Pt metallization layer, the metallization results are classified into two stages. This partially metallized silk substrate is classified into the first stage. Figure 6- 6(b) shows a SEM image of the sample metallized for 20 min. A continuous and fully covered Pt layer was achieved showing gray color on the entire surface, which are characterized into the second stage. As the Pt metallization time extended to 60, 100, and 140 min, (Figure 6- 6(c–e)), the silk substrates were completely covered.

It is worth to note that, the surface roughness increases as a function of the metallization time in the CONV metallization (Figure 3- 9). On the other hand, since sc–CO_2 gives brightener–like effect during the metallization [106], the surface became smoother than that metallized by the CONV metallization method when sc–CO_2 is applied. Moreover, hydrogen bubbles, which are generated as a side reaction during the metallization reaction, can be removed away from the substrate surface by the sc–CO_2 micelles due to the non–polar and high self–diffusivity characteristics [107], and this eventually leads to smooth Pt metallization layer as shown in Figure 6- 7.

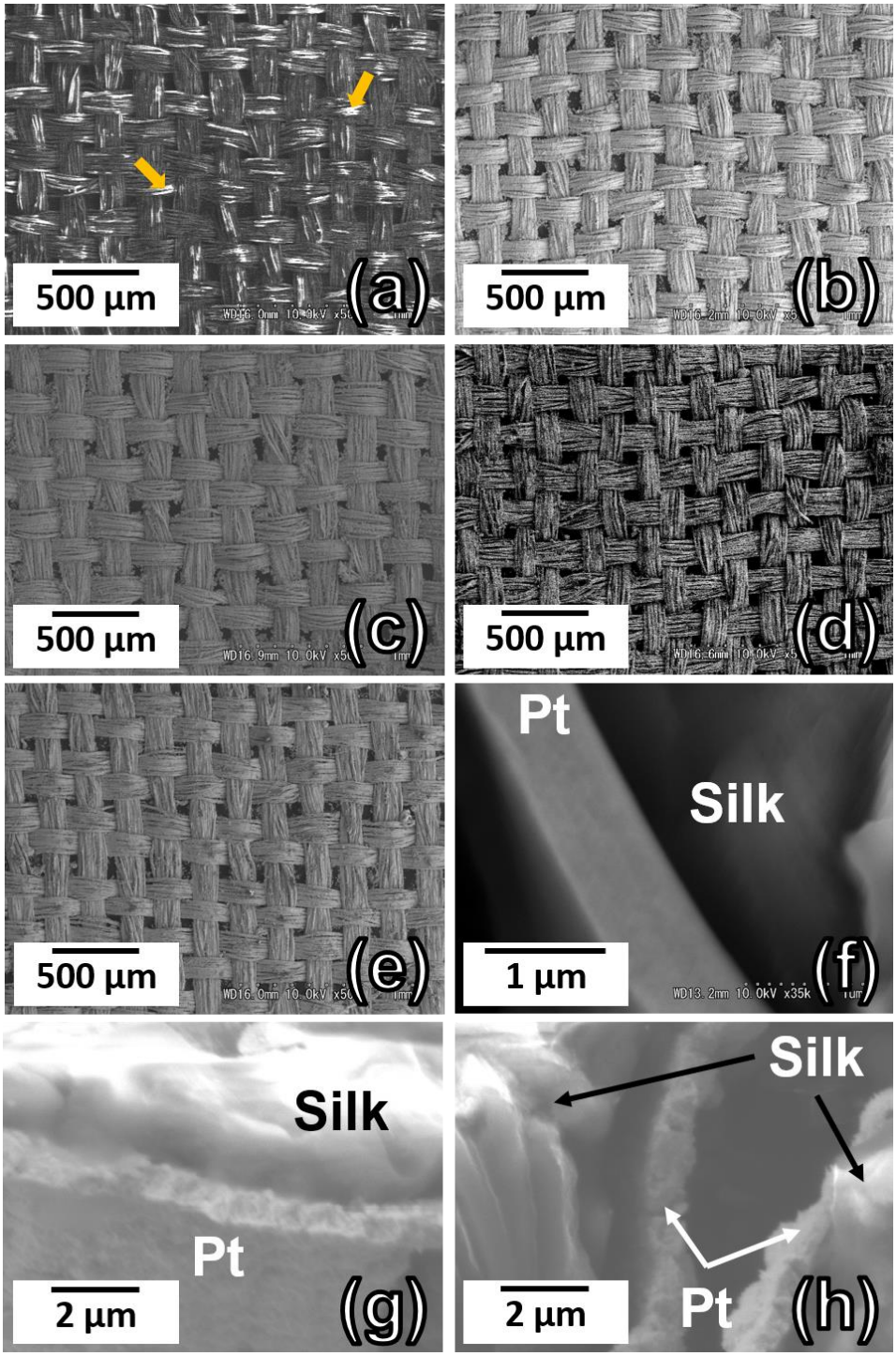

Figure 6- 6 SEM images of the Pt metallized silk with (a) 10 min, (b) 20 min, (c) 60 min, (d) 100 min, and (e) 140 min of the metallization time, and (f) cross–section of the silk/Pt by 140 min of the sc–CO_2 metallization, and (g) and (f) cross–section of the silk/Pt by CONV sc–CO_2 metallization

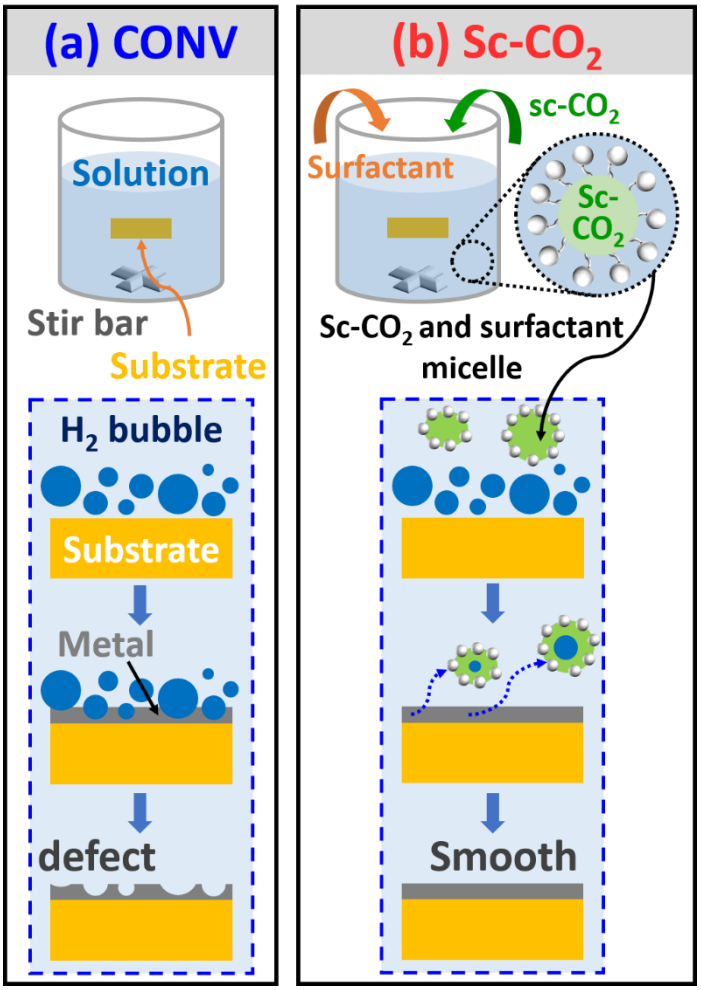

Figure 6- 7 Illustration of effects of sc–CO_2 on morphologies of the Pt layer by the (a) CONV and (b) sc–CO_2–assisted metallization

The dependences between the Pt layer thicknesses with the metallization time length are demonstrated in Figure 6- 8. Figure 6- 8(a) shows thickness of the Pt layer metallized at 100 min by the CONV metallization (5.3 Morphology, composition and structure of silk/Pt section). For the sc–CO_2–assisted metallization, Figure 6- 8(b), the Pt thicknesses show a positive correlation with the metallization time. The highest thickness at 0.75 μm was constructed with the longest metallization time of 140 min. The average growth rate was at 2.3 nm/min. This result is in accordance with the morphology shown in Figure 6- 6. No reliable thickness could be measured when the metallization time is

less than 10 min due to the poor electrical conductivity. The sc–CO_2–assisted metallization prepared specimens entered the second stage (full coverage stage) at 20 min of the metallization time having a thickness at 0.48 μm while the CONV samples entered the second stage at 100 min of the metallization time along with 0.76 μm of the Pt thickness. These results indicated that more Pt sources were used in growth of the Pt thickness instead of covering the silk textile in the CONV case. The full coverage with a thinner thickness can also be attributed to the high nuclei density in the sc–CO_2–assisted metallization (Figure 6- 5) [108]. Based on the aforementioned reasons, through introduction of sc–CO_2, full Pt coverage was achieved with less metallization time and less Pt ion source indicating a more efficient metallization.

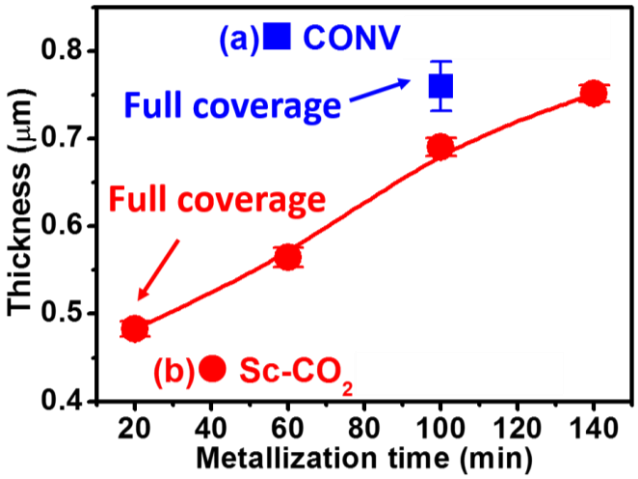

Figure 6- 8 Thickness of the Pt layer metallized by the (a) CONV method at 100 min of metallization time (**5.3 Morphology, composition and structure of silk/Pt** section) and (b) sc–CO_2–assisted method as a function of the metallization time

6.4 Electrical property of sc–CO_2 metallized silk/Pt

Electrical resistances of the as–metallized and the adhesive test–treated silk/Pt composites as a function of the metallization time are revealed in Figure 6- 9. Samples in the first stage exhibited high electrical resistances, which are mostly due to the incomplete

Pt coverage (refer to Figure 6- 6(a)). On the other hand, at 60 min of the metallization time, the electrical resistance reached 50 mΩ. The electrical resistance remained almost unaffected as the metallization time extended beyond 60 min due to the same degree of Pt coverage and smooth surface. This result is in accordance with the coverage shown in Figure 6- 6 indicating that the Pt coverage is one of the critical factors affecting the electrical resistance. After a significant drop of the electrical resistance in the first stage, the electrical resistance for the samples metalized at 20 to 140 min deliberately decreased in the second stage (also refer to Figure 6- 6(b–f)).

In the CONV metallization, similar two stages were found; however, the electrical resistance was offset by the increasing roughness as the metallization time goes beyond 140 min (5.4 Electrical property of silk/Pt section). On the other hand, the sc–CO_2–assisted metallization gives compact and smooth Pt coatings on the silk (Figure 6- 6(f)). The electrical resistance thus persisted after 60 min of the metallization time. The second stage was prolonged by the sc–CO_2–assisted metallization, and the region showing the deteriorated electrical conductivity was not found in this study. No experiments were conducted at the metallization time longer than 140 min since the electrical resistances are expected to remain at the same level.

The grain size can affect the electrical resistance, and a finer grain size is expected to result a higher electrical resistance [109]. In Figure 6- 4, finer grain size of the Pt layer via the sc–CO_2–assisted metallization was obtained while comparing to the CONV metallization. However, electrical resistance of the silk/Pt synthesized by the sc–CO_2–assisted metallization method shows a 16% reduction while comparing to those without sc–CO_2 (5.4 Electrical property of silk/Pt section). Roughness of the Pt layer metallized

on the silk is suggested to be the cause of the difference in electrical resistance [109]. Cross–sections of the samples prepared by the CONV (Figure 6- 4(g) and (h)) and the sc–CO_2–assisted metallization methods (Figure 6- 6(f)) with the optimized metallization conditions clearly demonstrated the difference in roughness of Pt layer metallized on silk.

Electrical resistances of the adhesive test–treated silk/Pt are shown in Figure 6- 9. No adhesive tests were performed for the samples in the first stage due to the unfeasible high electrical resistance for applications. Impact of the adhesive test on electrical resistance of the sc–CO_2–assisted metallized samples was not obvious. 18% reduction in the electrical resistance after second adhesive was observed in the sample prepared by the CONV method (5.4 Electrical property of silk/Pt section). On the other hand, only 0.5% reduction in the electrical resistance was observed after second adhesive test in this study. The closely packed and smooth Pt coating prepared by the sc–CO_2–assisted metallization method allows the Pt layer to stay intact after second adhesive test and shows better resistance against the adhesive tests than those prepared without utilizing sc–CO_2.

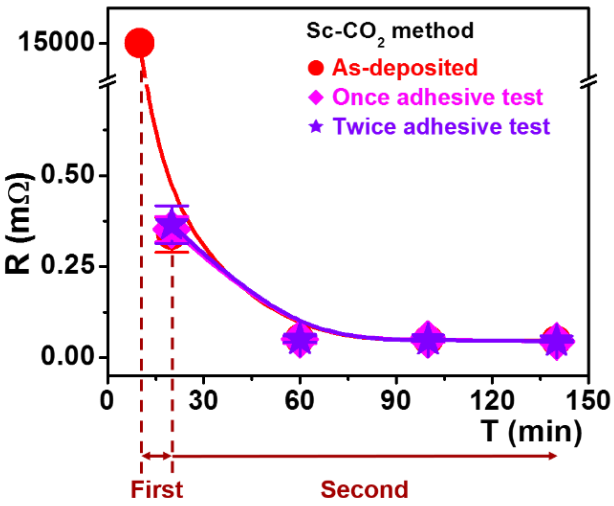

Figure 6- 9 Electrical resistance–metallization time curves of silk/Pt composites before and after the adhesive tests

6.5 Corrosion resistance of sc–CO_2 metallized silk/Pt

Figure 6- 10(a) shows polarization curves of the as–metallized and the adhesion test–treated silk/Pt composites in 3.5 wt.% NaCl solution. Samples prepared with 140 min of the metallization time were chosen for the corrosion resistance evaluations. No significant difference was found between the three polarization curves in Figure 6- 10(a) revealing excellent corrosion resistance of this Pt layer. The E_{corr} and I_{corr} are summarized in Table 6- 1. Specimens prepared by the sc–CO_2–assisted metallization show higher corrosion resistance than those by the CONV method (5.4 Electrical property of silk/Pt section). In 3.5 wt.% NaCl solution, the corrosion current density after second adhesive test decreased from 5.93 x 10^{-7} to 2.17 x 10^{-7} A/cm^2 when sc–CO_2 was introduced into the metallization step. Decrease in the corrosion current density is suggested to be a result of the smooth surface condition and compact Pt metallization layer when the sc–CO_2–assisted metallization step is applied.

Similarly, Figure 6- 10(b) shows polarization curves of the as–metallized and adhesion–treated samples in the SBF. In the same way, composites metallized at 140 min were chosen as the working electrode. The E_{corr} and I_{corr} are also listed in Table 6- 1, which shows limited standard deviation around ± 0.005 (μA/cm^2). The corrosion resistances are similar to those of bulk Pt metal indicating high corrosion resistance of the Pt metallization layer despite being deposited on a non–conductive substrate. In addition, the corrosion current density after second test decreased from 2.02 x 10^{-7} to 1.71 x 10^{-7} A/cm^2 in the SBF while sc–CO_2 was introduced (5.5 Corrosion resistance of silk/Pt section). Silk/Pt composite shows high corrosion resistance in the corrosion test in both 3.5 wt.% NaCl and SBF. The results indicated that the silk/Pt composites fabricated by sc–CO_2–assisted metallization method is a promising materials for the wearable devices.

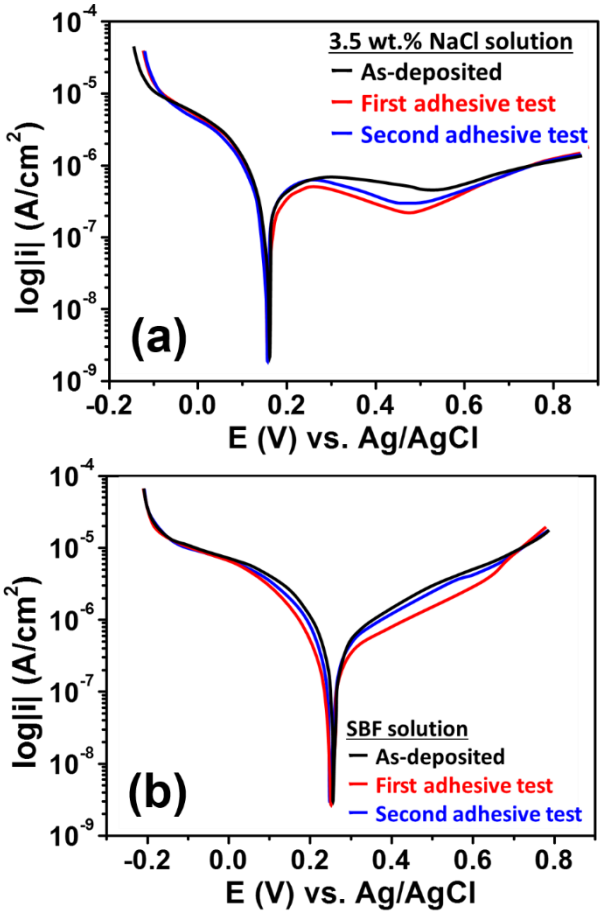

Figure 6- 10 Polarization curves of the silk/Pt composites in (a) 3.5 wt.% NaCl and (b) SBF solutions at room temperature and 1 atm

Table 6- 1 Corrosion potentials and corrosion current densities of the silk/Pt composites in (a) 3.5 wt.% NaCl and (b) SBF solutions at room temperature and 1 atm

(a) Samples (in 3.5 wt.% NaCl)	E_{corr} (V)	I_{corr} ($\mu A/cm^2$) ± SD
As–deposited	0.16	0.217 ± 0.005
First adhesive test	0.16	0.220 ± 0.004
Second adhesive test	0.16	0.217 ± 0.004
(b) Samples (in SBF)	E_{corr} (V)	I_{corr} ($\mu A/cm^2$) ± SD
As–deposited	0.25	0.175 ± 0.007
First adhesive test	0.26	0.167 ± 0.006
Second adhesive test	0.25	0.171 ± 0.005

6.6 Biocompatibility assessment of sc–CO_2 metallized silk/Pt by immersion test

Allergy reaction is provoked when there is metal ion released from the environment and transferred into human body as reported by Wataha [101], therefore, examining metal ion releasing rates in the SBF is a straightforward approach to assess the biocompatibility of the silk/Pt composite. Metal ion concentrations in human body vary with races, environments, and diets. The input and output of Pd and Pt ions for human body has been already discussed in 5.6 Biocompatibility assessment of silk/Pt by immersion test section. In this study, after 3 months of the immersion test in the SBF at human body temperature (37 ^{o}C), the Pd and Pt releasing rates were only 0.037 μg/day and 0.057 μg/day, respectively. The releasing rates are too small and can be neglected when comparing to the daily intake and output rates. Despite of the small grain size, which can promote release of metal ions, the corrosion resistance was balanced by the high compactness of the Pt layer.

The silk/Pt composites prepared by sc–CO_2–assisted catalyzation and metallization methods showed smooth and compact surface conditions for the Pt metallization layer, decent electrical conductivity, high reliability from the adhesive tests, and high biocompatibility in both of the immersion and polarization measurements. The results further demonstrated practicability of the Pt metallized silks in wearable and medical devices.

6.7 Brief summary for sc–CO_2 metallized silk/Pt

Robust and electrical conductive Pt metallized silks were successfully fabricated via the sc–CO_2–assisted eletroless plating technique in this study. In the catalyzation step, the $Pd(acac)_2$ was successfully inlaid into the silk textile without damaging the structure

with the help of sc–CO_2. In the metallization step, a compact and smooth Pt layer was metallized. The coverage and thickness of the Pt metallized layer increased as a function of the metallization time. Full Pt coverage on the silk substrate was achieved in merely 20 min of the metallization time, which was shortened significantly while comparing to the metallization method without sc–CO_2. The electrical resistance reached 50 mΩ at 60 min of the metallization time and remained almost unchanged as the metallization time extended to 140 min since the surface was smoothened by the introduction of sc–CO_2. The electrical resistance persisted after the adhesive tests, which also confirmed the great enhancement in the reliability while comparing to those synthesized by the metallization method without sc–CO_2. The silk/Pt composite shows high corrosion resistance before and after the adhesive test in both 3.5 wt.% NaCl and the SBF solutions. The Pd and Pt ion releasing rates were both negligible comparing to the daily input and output of Pd and Pt in human body.

Chapter 7 Functionalization of Au metallized silk textile by ZnO cathodic deposition

7.1 Introduction

The global market of wearable devices is predicted to keep prospering in the future. In the meanwhile, wearable devices are diversified into different functions such as biomedical devices, supercapacitors, and photocatalytic devices [110] due to diverse requirements in the next–generation technology. The integration of functional and flexible materials turns out to be the most critical step in fabrication of the component used in wearable devices. For example, integration of photocatalytic, electrical conductive, and flexible materials is needed to realize wearable devices capable of harvesting solar energy.

Regarding the photocatalytic functionality, there are various synthetic methods to deposit photocatalytic metal oxides. Among the synthetic techniques, cathodic deposition allows a simple and effective process for the synthesis of metal oxides (1.2.3 Cathodic deposition section). In addition, cathodic deposition can cooperate with lithography to allow further applications such as patterning. In this section, the flexible cloth textile/metal/photocatalyst composite material was realized by sc–CO_2 assisted electroless plating and cathodic deposition for applications in functional wearable devices.

7.2 Activation of silk textile via sc–CO_2 $Pd(acac)_2$ catalyzation

Figure 7- 1 shows OM images and X–ray diffraction patterns of the as–received silk and the catalyzed silk. The crossed–linked see–through bundles shown in Figure 7- 1(a) imply the silk textile, and the yellow flakes in Figure 7- 1(c) specify the $Pd(acac)_2$

catalyst. A broad peak at $2\theta = 20^{o}$ can be observed in Figure 7- 1(b), which reveals an amorphous structure of the silk textile. On the other hand, diffraction peaks labelled by diamond symbols can be indexed to $Pd(acac)_2$ [82, 83], and the results indicated the catalysts were successfully deposited on the substrate. As shown in the OM images, the silk substrate remained intact after the catalyzation step due to the low surface tension, low viscosity, and non–corrosive properties of sc–CO_2. The sc–CO_2 assisted catalyzation step demonstrated a significant improvement while comparing to the CONV catalyzation process which was shown in 3.2 Activation of silk textile via sc–CO2 $Pd(acac)_2$ catalyzation section. $Pd(acac)_2$ acts as an activation site after it was reduced to Pd metal by the reductant in the metallization solution. Pd metal can play the role of catalyst and activate the following metallization.

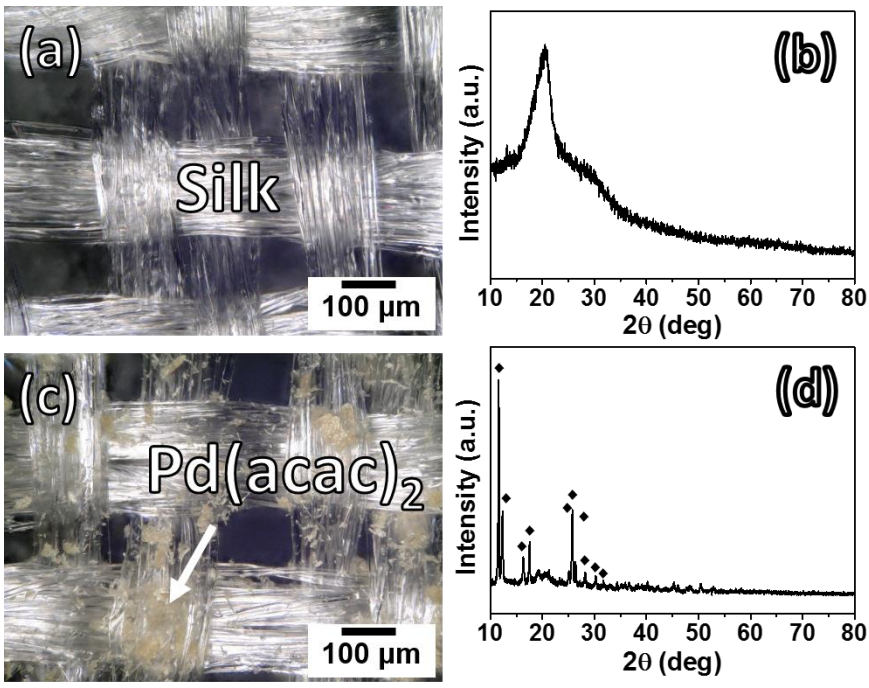

Figure 7- 1 (a) OM image and (b) X–ray diffraction pattern of the as–received silk as well as (c) OM image and (d) X–ray diffraction pattern of the catalyzed silk (diamond symbol: $Pd(acac)_2$ catalysts)

7.3 Morphology, composition and structure of silk/Au

Development of the Au layer is shown in Figure 7- 2. Figure 7- 2(a) shows morphology of the specimen with the Ni–P metallization time at 4 min before the Au metallization. Figure 7- 2(b–d) demonstrate the Au metallization time at 3 min, 5 min, and 80 min, respectively. At 3 min of the Au metallization (Figure 7- 2(b)), part of the Ni–P layer was still not enclosed showing a gray luster. As the Au metallization times was extended to 5 min and longer (Figure 7- 2(c) and (d)), the Ni–P layer was completely concealed by the Au layer.

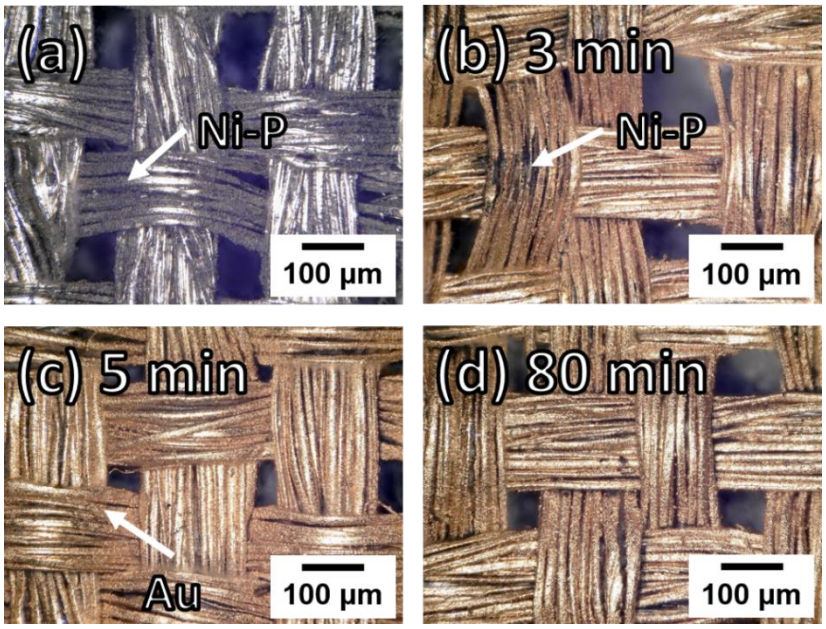

Figure 7- 2 OM images of the (a) Ni–P metallized silk and the Au metallization at (b) 3 min, (c) 20 min, and (d) 80 min

The X–ray diffraction patterns at various Au metallization time are shown in Figure 7- 3(a–c). Five apparent diffraction peaks shown in Figure 7- 3(a–c) locate at 2θ = 38.2°, 44.4°, 64.6°, 77.6°, and 81.7° can be indexed to (111), (200), (220), (311), and (222) planes, respectively, of the FCC structure for Au (JCPDS #65–2870). In Figure 7- 3(a), at 3 min of the Au metallization time, only a thin layer of Au was metallized on the

silk, and the broad diffraction peak of silk at around 20° was still detectable. Ni–P diffraction peaks were not found in Figure 7- 3(a), because the Ni–P layer is designed as the sacrifice layer for the Au metallization. In addition, it owns amorphous structure (Figure 3- 4), which the amorphous peaks might be overlapped by the high intensity Au diffraction peaks. As the Au metallization proceeded, no diffraction peaks of the silk were found in the X–ray diffraction patterns (Figure 7- 3(b–c)) since the Au layer is thick enough to suppress the diffraction peaks from the silk. Figure 7- 3(d) shows the composition change with the Au metallization time. In the early stage, due to the insufficient thickness of Au, the Ni–P layer was detectable by the EDX. On the contrary, the Ni–P was no longer detectable as the Au metallization time extended to 80 min. Phosphorus was not detected owing to the insufficient amount (Table 3- 1).

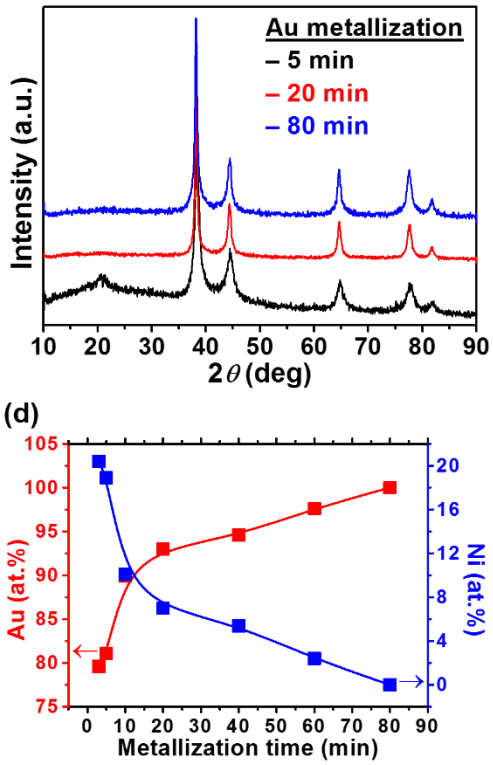

Figure 7- 3 X–ray diffraction patterns of the Au metallization at (a) 5 min, (b) 20 min, and (c) 80 min and (d) the composition revolution with the Au metallization time

Figure 7- 4 illustrates growth of the Au layer thickness with the Au metallization time. There is no obvious partition of the Ni–P and Au layer shown in the inserted SEM image in Figure 7- 4. A positive correlation was found between the Au layer and the Au thickness presenting the average growth rate at 0.48 μm/hr. The growth rate slowed down slightly from 60 min to 80 min of the Au metallization time due to the consumption and reduction in concentration of the metal ion and reducing agent as the reaction proceeded.

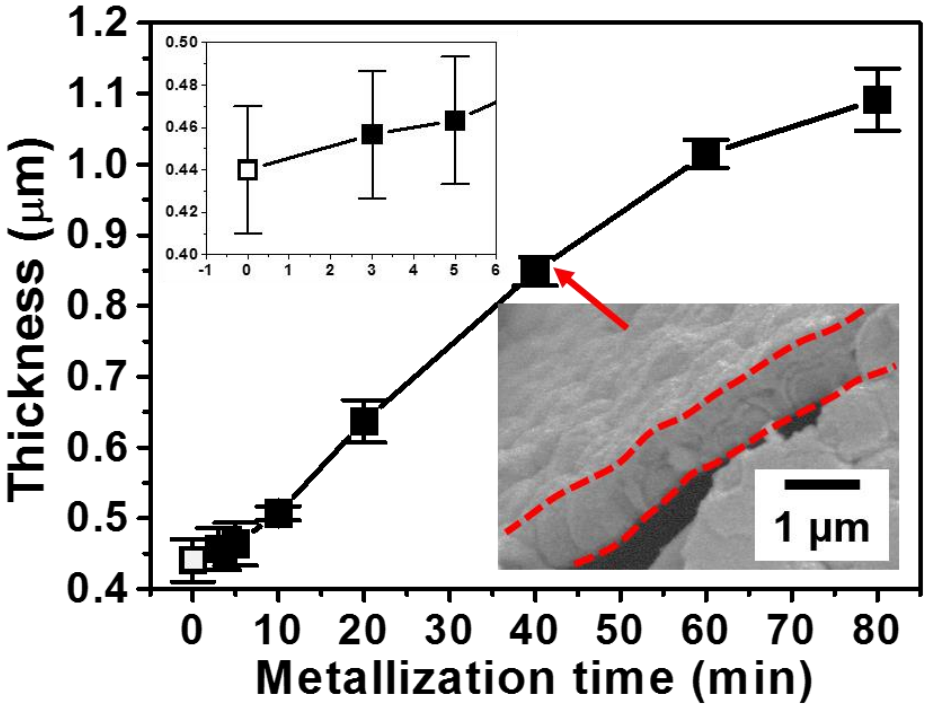

Figure 7- 4 Plot of the Au metallization thickness versus the metallization time (hollow symbol: Ni–P metallization at 4 min and solid symbols: Au metallization thickness versus Au metallization time) (OM image of Au metallized at 40 min of the metallization time is inserted into bottom–right)

7.4 Electrical property of silk/Au

The electrical resistances at various Au metallization times are shown in Figure 7- 5. The electrical resistance dropped down in the early stage and increased after reaching

a minimum point. Since the Ni–P layer is not fully covered by Au at 3 min of Au metallization time (solid symbol) (Figure 7- 2(a) and Figure 7- 2(a)), it showed high electrical resistance close to the Au–free specimen at 0 min of Au metallization (hollow symbols) (Figure 7- 5(a)). An inserted graph in Figure 7- 5(a) shows results of the Au metallization time between 0 to 5 min.

The electrical resistances obtained from 0 to 5 min (the dash line shown in Figure 7- 5) of the metallization time, which merely showed a slight difference from the Au–free one, are classified into the first stage. Full coverage was constructed as the Au metallization time reached 5 min, and the electrical resistance was improved accordingly. The electrical resistance reached its minimum at the Au metallization time of 20 min due to the complete coverage, smooth surface, and sufficient Au thickness (Figure 7- 5(b)). From the beginning of the full coverage to the region near the lowest electrical resistance can be sorted to the second stage (from the dash line at 5 min to the other one at 40 min). The electrical resistance increased slightly as the Au metallization time increased beyond the minimum point. The surface grew coarser (pointed by the arrows in Figure 7- 5(c)) with the elongated metallization time, and the electrical resistances were deteriorated due to more electron scattering [89]. The region of worsened electrical resistance and bumpy surface can be categorized into the third stage.

The electrical resistances after the adhesive tests are also shown in Figure 7- 5(a). No significant impact was observed in all stages since the silk was completely enclosed by the Ni–P and Au, and the adhesions between the silk and the Ni–P and between the Ni–P and the Au both showed sturdy adhesive property.

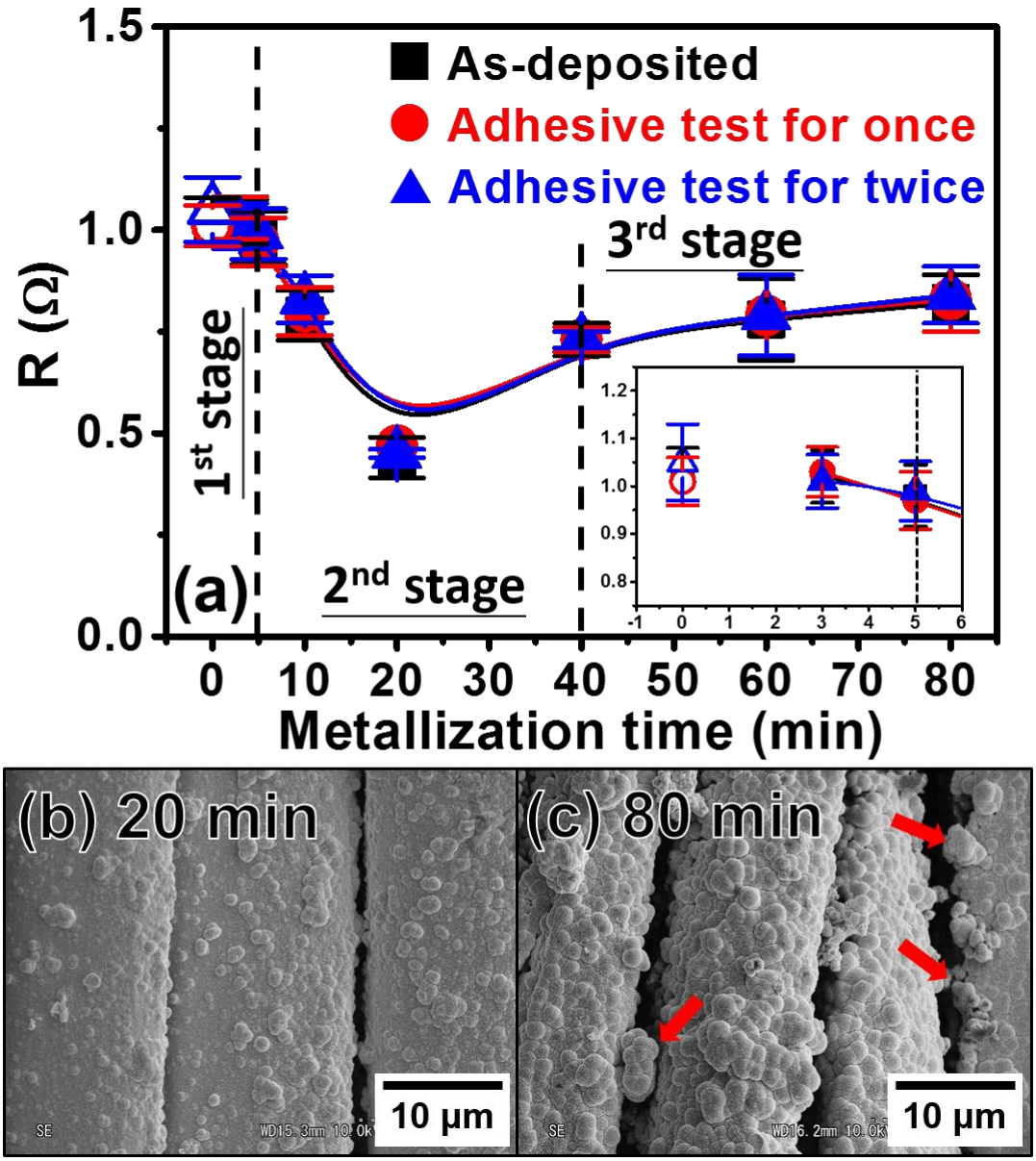

Figure 7- 5 (a) Electrical resistances of the Au metallized silk at various metallization times and SEM images of the Au metallized silk at (b) 20 min and (c) 80 min of the metallization time (hollow symbols: Au–free; solid symbols: Au metallized)

7.5 Cathodic ZnO deposition

Figure 7- 6 shows SEM images (Figure 7- 6(a–d)) and OM images (Figure 7- 6(e–h)) of the pristine ZnO deposited with H_2O_2 concentration varied from 0 to 0.3 wt.%.

Tower–like ZnO nanowires are observed in all of the SEM images (Figure 7- 6(a–d)). ZnO coverage on the Au layer was processed and calculated by a built–in software of the OM. The ZnO coverages were at 63%, 62%, 41%, and 32% for the specimens deposited with free of H_2O_2 to 0.3 wt.% H_2O_2. Morphology of cathodically deposited ZnO is often affected by Cl^- in the solution. The Cl^- ion can act as a capping agent adsorbing on the (0001) plan of ZnO to stabilize the surface and leads to formation of nano–rod like structures. On the other hand, when concentration of the Cl^- is low, tower–like structures instead of nano–rod structures are formed [61]. Furthermore, size of the ZnO particle increased as the H_2O_2 concentration increased from 0 to 0.2 wt.% as shown in the SEM images. Similar results on increase in the ZnO particle size as the H_2O_2 concentration increased were reported in a literature [111]. However, in Figure 7- 6(d), the particle size decreased when the H_2O_2 concentration went beyond 0.2 wt.%. ZnO deposition equations are shown in the following [112]:

$$NO_3^- + H_2O + 2e^- = NO_2^- + \ 2OH^- \quad (7.\ 1)$$

$$H_2O_2 + 2e^- = 2OH^- \quad (7.\ 2)$$

$$Zn^{2+} + 2OH^- = ZnO + H_2O \quad (7.\ 3)$$

OH^- generated on the substrate from equation (1) and (2) are expected to react with Zn^{2+} in the electrolyte to form ZnO on the substrate. As shown in equation (2), generation rate of the OH^- would be increased with an increase in H_2O_2 concentration. Since the diffusivity of Zn^{2+} in aqueous solution is four times slower than that of H_2O_2, diffusion of Zn^{2+} to the substrate surface cannot catch up with the generation of OH^- as the H_2O_2 concentration increased [113]. When the amount of H_2O_2 was increased to 0.3 wt.%, generation rate of the OH^- could be too high and accumulate at the electrode surface.

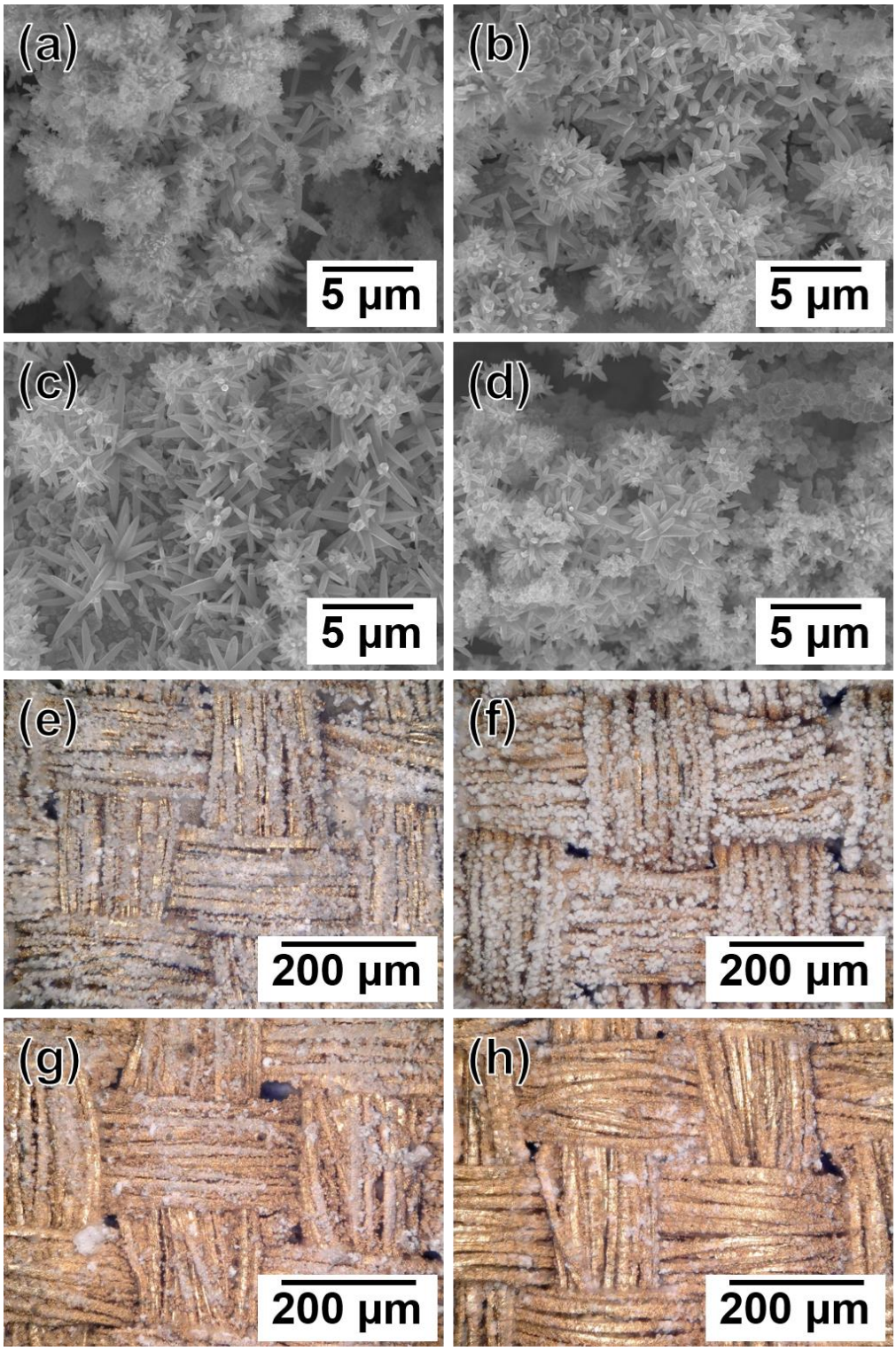

Figure 7- 6 SEM images of the specimens deposited in (a) free of H_2O_2, (b) 0.1 wt.%, (c) 0.2 wt.%, and (d) 0.3 wt.% H_2O_2, and the OM images in (e) free of H_2O_2, (f) 0.1 wt.%, (g) 0.2 wt.%, and (h) 0.3 wt.% H_2O_2

A general scheme of the solute concentration profiles in the electrolyte is shown in Figure 7- 7. OH^- are generated on the substrate, hence the concentration is gradually lowered toward the bulk solution direction. Zn^{2+} would diffuse from the bulk solution to the substrate surface to react with the OH^-, therefore, the concentration is lowered as it approaches the substrate surface. Depends on the OH^- generation rate, local OH^- concentration, or pH, on the substrate could vary. ZnO is formed at a pH range of ca. 8 to 12, and ZnO would dissolve away to form ZnO_2^{2-} or $HZnO^{2-}$ when the pH is higher than 12 [62, 114]. The region suitable for deposition of ZnO is defined as region I, and the region leads to dissolution of ZnO is denoted as region II as shown in Figure 7- 7.

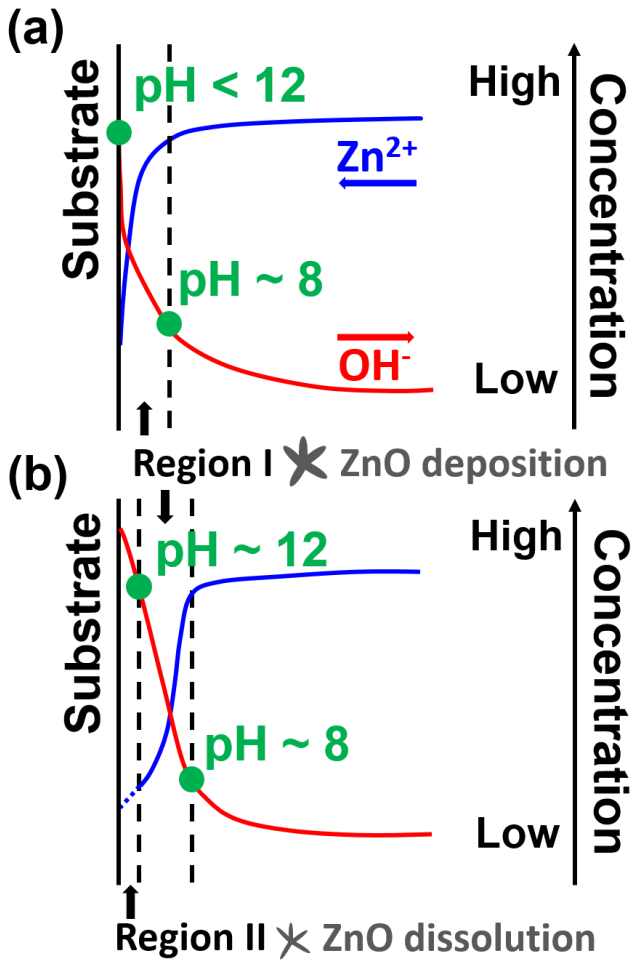

Figure 7- 7 General scheme of the solute concentration profiles

The region near surface of the substrate would be in region I when the H_2O_2 concentration was lower than 0.2 wt.%. Therefore, an increase in the H_2O_2 concentration led to an increase in the particle size (Figure 7- 6(a–b)) and the coverage (Figure 7- 6(e–f)). When the H_2O_2 concentration was increased to 0.3 wt.%, both the particle size (Figure 7- 6(d)) and the coverage (Figure 7- 6(h)) were decreased, which suggest the pH near the substrate surface could be higher than 12. The results suggest the region near the substrate surface is in region II when the H_2O_2 concentration is higher than 0.3 wt.%.

Figure 7- 8(a) shows X–ray diffraction patterns of the ZnO deposited with various H_2O_2 concentrations in the electrolyte. Only the diffraction peaks of Au (star symbol) and ZnO (hexagon symbol) were observed. No secondary phase was found in the X–ray diffraction patterns after the ZnO deposition. A relative crystallinity of ZnO on the Au layer was roughly estimated by calculating ratio of the Au (111) intensity to the ZnO (100) intensity with consideration of the ZnO coverage. The ratios were at 0.10, 0.11, 0.34, and 0.16 from free of H_2O_2 to 0.3 wt.% H_2O_2. The ratios indicated the electrolyte containing 0.2 wt.% H_2O_2 produced ZnO with the best crystallinity, and the crystallinity became worse when 0.3 wt.% H_2O_2 was used. Another explanation concerning crystallinity of the ZnO is provided here. Crystallinity of the ZnO is reported to be dependent on concentration of the Zn^{2+} [115], which defects and deteriorated crystallinity are introduced to the ZnO when the Zn^{2+} concentration is low. In this study, when the H_2O_2 concentration reached 0.3 wt.%, local concentration of OH^- near the electrode surface would be high, and higher diffusion rate of OH^- to the bulk solution was built. Then, pH far away from the substrate surface became suitable for formation of ZnO and consumed great amount of the Zn^{2+}. In this case, amount of the Zn^{2+} diffused to the substrate surface was lowered and resulted the deteriorated crystallinity.

Figure 7- 8(b) shows the voltage–time curves during the ZnO deposition. While there is H_2O_2 in the electrolyte, the potential drop decreased as the H_2O_2 concentration increased. The potential drop here refers to the potential difference between the potential at ca. 0 sec of the reaction time and the potential as the reaction gradually stabilized with time. No obvious difference was found in the specimens deposited with free of H_2O_2 and 0.1 wt.% H_2O_2, which are in good agreement with the ZnO coverage in Figure 7- 6(e) and Figure 7- 6(f) revealing that 0.1 wt.% H_2O_2 has limited influence on the ZnO deposition. The potential fluctuation increased with an increase in the H_2O_2 concentration, which is because more N_2 gas is emitted at high pH [116].

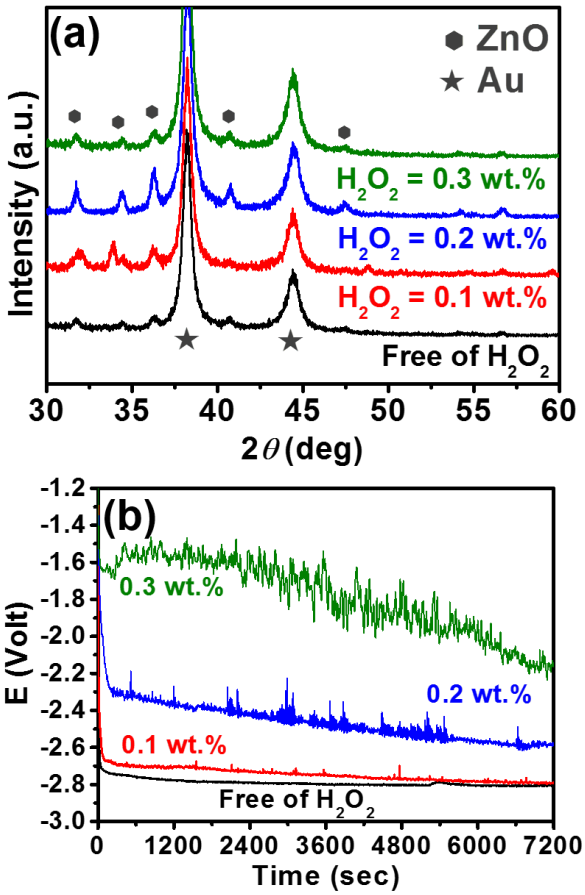

Figure 7- 8 (a) X–ray diffraction patterns and (b) voltage–time plot of the specimens fabricated with electrolytes containing various H_2O_2 concentration

7.6 Photocurrent evaluation of silk/Au/ZnO

To assess the applicability as photocatalytic materials, photocurrent generated from photoelectrochemical water splitting reaction using the as–deposited sample as the photoanode was evaluated. Figure 7- 9 shows the chronoamperometric I−t curves of the silk/Au/ZnO layered materials recorded in 0.5 M Na_2SO_4 electrolyte under chopped light illumination. The current density was corrected by considering coverage of the ZnO on the Au layer, which the ZnO coverages are provided in the beginning of this section.

Figure 7- 9(a) shows the as obtained current density, which is before the correction, while Figure 7- 9(b) shows the corrected values. All the specimens showed an increased in the current density when the illumination is on, which imply the effective generation, transfer and collection of the electrons during the water splitting process. The ZnO deposited with 0.2 wt.% H_2O_2 showed the highest current density in both Figure 7- 9(a) and Figure 7- 9(b) since it owns the highest crystallinity. It has been reported that the high crystallinity can assist in suppressing the possible photocorrosion effect [117]. In addition, high crystalline ZnO leads to efficient transportation of the excited electrons. Photocurrent density of the ZnO fabricated with 0.2 wt.% H_2O_2 increased 11.5 times while comparing to the one deposited without H_2O_2. The greater photoelectrochemical performance can be attributed to the facile carrier transport resulting from the oriented crystallinity. In this study, high H_2O_2 concentration led to the high photocurrent owing to the high crystallinity; however, excess OH^- resulted in the dissolution of ZnO and deteriorated crystallinity, which resulted deteriorated photocurrent density. A digital photo is inserted into Figure 7- 9(a) to show the flexibility of the composite material.

Various evaluations have been done on the silk/Au/ZnO composite materials in

this study. The composite shows flexibility, high electrical conductivity, and high adhesive firmness. Photocurrent density was enhanced significantly by the optimized ZnO deposition solution. Therefore, the results showed the potential of the materials in the applications of flexible wearable devices.

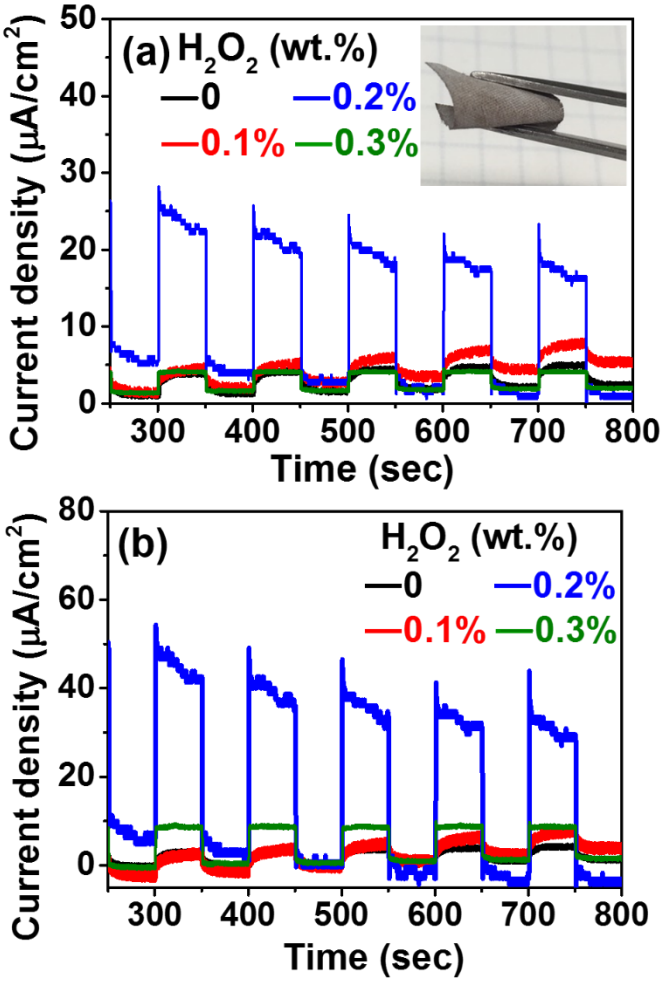

Figure 7- 9 Photocurrent density of the silk/Au/ZnO hybrid materials with (a) non–corrected (an inserted figure shows the flexibility of the composite material) and (b) corrected by the ZnO coverage

7.7 Brief summary for silk/Au/ZnO

ZnO/Au layered structure was successfully fabricated on the silk textile by sc–

CO_2 assisted electroless deposition and cathodic deposition. Common problems encountered in the conventional electroless plating were solved by the introduction of sc–CO_2. With the help of sc–CO_2, silk was catalyzed without defects and the adhesive property between the silk and the metallized layer was enhanced at the same time. Surface coverage and thickness of the Au layer increased with the Au metallization time. The lowest electrical resistance was achieved as the Au metallization time extended to 20 min. On the other hand, ZnO was deposited on the Au metallized silk via the cathodic deposition method. The coatings on the silk have been confirmed to be metallic Au phase and ZnO wurtzite phase. ZnO deposited with 0.2 wt.% H_2O_2 showed the best crystallinity and the highest photocurrent density. The ZnO modified specimen with 0.2 wt.% H_2O_2 performed 11.5 times enhancement in the photocurrent density while comparing to that without H_2O_2.

Chapter 8 Reliability and photocatalytic activity enhancement by Ni–P co–deposition

8.1 Introduction

In this chapter, our objective is to enhance the various properties of the photocatalytic composites such as adhesive property, corrosion resistance, and photocatalytic activity. Co–deposition was utilized since the oxides and metallization layer can be co–deposited and thus the adhesive property can be enhanced. On the other hand, TiO_2 was used for its inactive property, acting as a reinforcing phase, and high photocatalytic activity.

8.2 Activation of silk textile via sc–CO_2 $Pd(acac)_2$ catalyzation

Figure 8- 1 shows OM images and XRD patterns of the as–received silk and the sc–CO_2 catalyzed silk. The transparent interwoven bundles shown in Figure 8- 1(a) indicate the silk textile, and Figure 8- 1(b) shows a broad peak at around $2\theta = 20^{o}$, this broad peak reveals an amorphous structure of the silk textile. The light yellow flakes around the silk bundles in Figure 8- 1(c) specify the $Pd(acac)_2$, and the diffraction peaks in Figure 8- 1(d) labelled by triangle symbols can be indexed to $Pd(acac)_2$ very well [82, 83], which indicated that the $Pd(acac)_2$ organometallic compounds were successfully deposited on the silk substrate. As demonstrated in the Figure 8- 1(a) and (c), the silk textile remained undamaged after the 2 hours sc–CO_2 catalyzation treatment due to the low surface tension, low viscosity, and non–corrosive properties to most of polymers of sc–CO_2 [15, 21, 84]. The sc–CO_2 catalyzation practiced a significant advancement when

it is compared to the conventional catalyzation process [15].

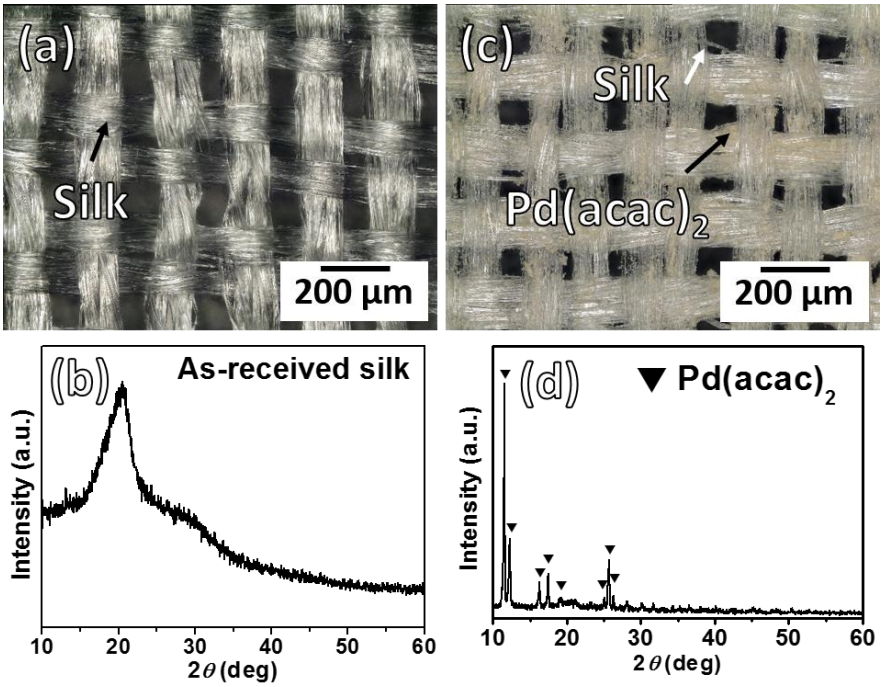

Figure 8- 1(a) OM image and (b) XRD pattern of the as–received silk, and (c) OM image and (d) XRD pattern of the sc–CO_2 catalyzed silk (triangle symbols: $Pd(acac)_2$).

8.3 Ni–P/TiO_2 co–deposition

Surface conditions of the Ni–P/TiO_2 decorated silk textiles prepared from the Ni–P electrolytes containing various TiO_2 concentrations (0, 10, 20, 30, 40, and 50 g/L) can be observed from SEM and OM images (inserted into top–left of each SEM images) shown in Figure 8- 2. Figure 8- 2(a) shows morphology of the specimen deposited without TiO_2 particles in the Ni–P electrolyte. It shows smooth surface while comparing to the other ones deposited with TiO_2 in the electrolyte (Figure 8- 2(b–f)). The bright nano–sized protrusions shown in Figure 8- 2(b–f) indicate the deposition of TiO_2 which resulted in roughening of the surface. However, the surface roughness decreased when the TiO_2 concentration went beyond 30 g/L in Ni–P electrolyte.

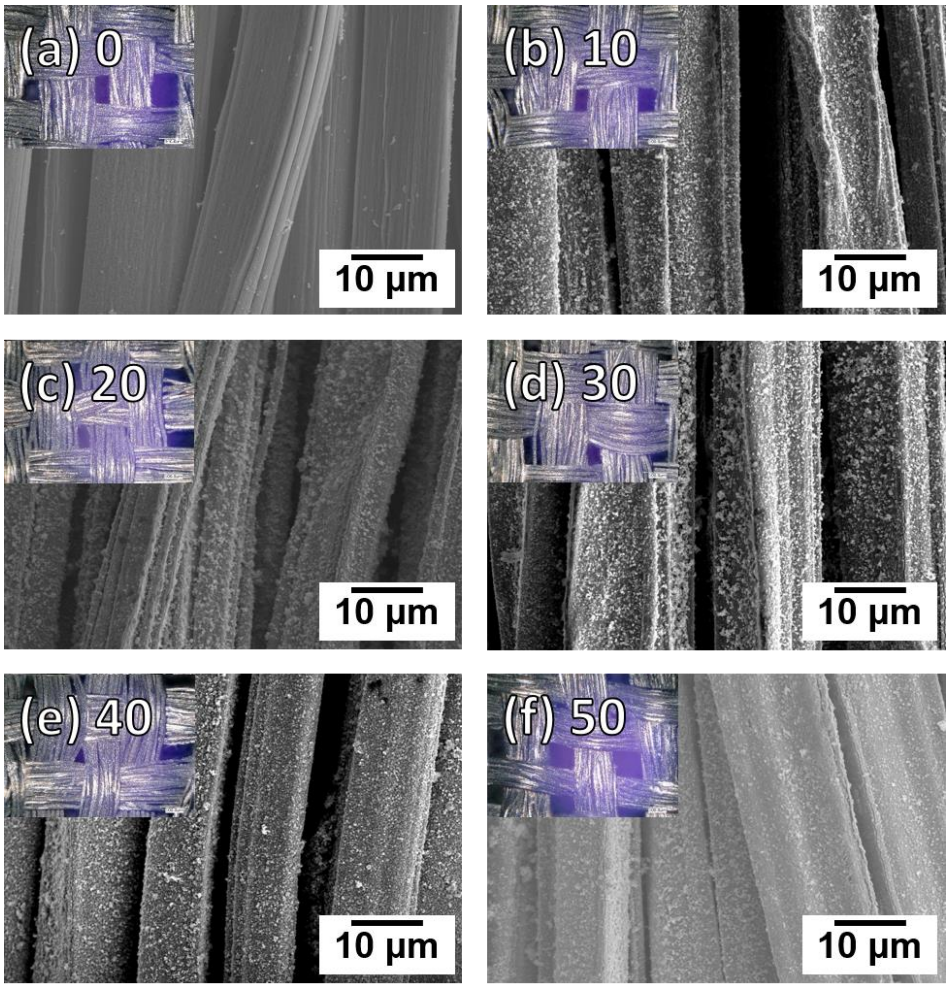

Figure 8- 2 SEM images and OM images (inserted into top–left) of Ni–P/TiO_2 deposition with various TiO_2 concentration at (a) 0, (b) 10, (c) 20, (d) 30, (e) 40, and (f) 50 g/L, respectively.

The nano-scale TiO_2 particles in the electrolyte would aggregate to form large aggregate particles, and average size and size distribution of the aggregate particle are related to concentration of the oxides particle in the solution [118-123]. In this study, when the TiO_2 concentration is low (10 and 20 g/L), there is only slight aggregation of the TiO_2 particles in the Ni–P electrolyte. Average size of the aggregate particle size is small, and the distribution is narrow as illustrated in Figure 8- 3(a). Level of the aggregation gradually increases with an increase in concentration of the TiO_2, and average

size of the aggregate particle becomes larger with a wider size distribution as shown in Figure 8- 3(b and c). Compositions of Ni–P/TiO_2 depositions are shown in Table 8- 1.

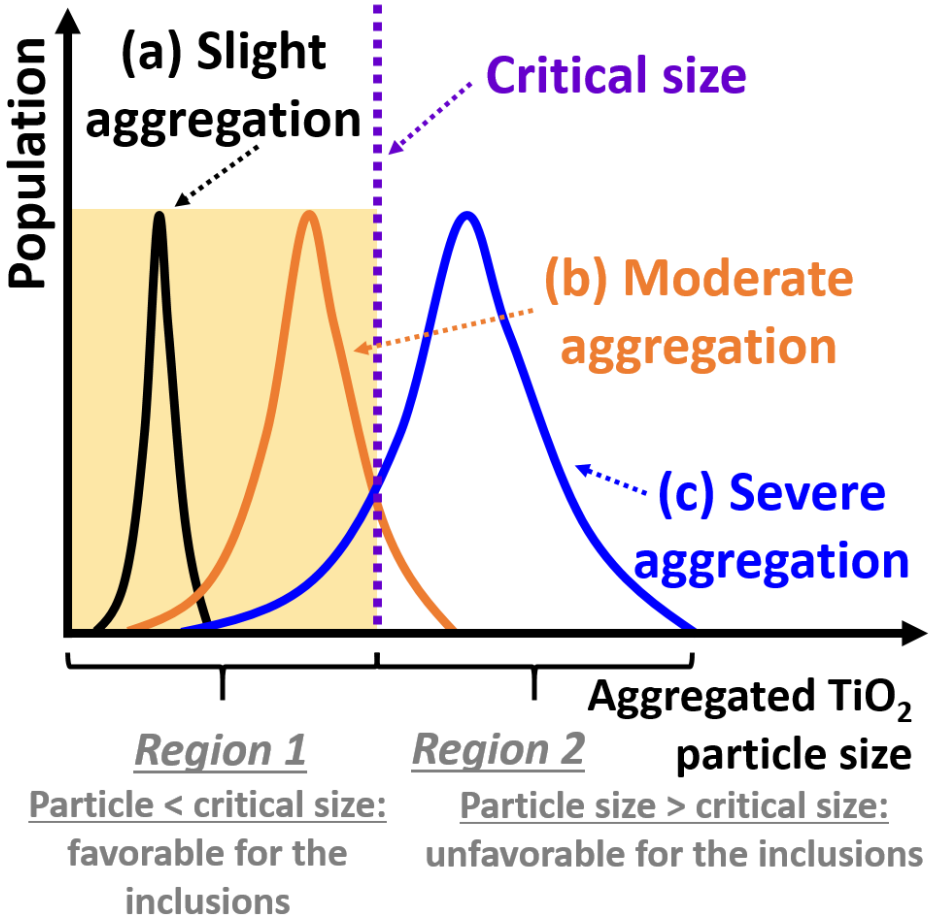

Figure 8- 3 TiO_2 particle size distribution with different amount of TiO_2 in the electrolyte: (a) slight aggregation, (b) moderate aggregation, and (c) severe aggregation.

Table 8- 1 Composition of as–deposited Ni–P/TiO_2 metallization layers on silk textiles.

	TiO_2 (g/L)						
Atom	**0**	**10**	**20**	**30**	**40**	**50**	**60**
P (at.%)	22.11	18.82	19.85	19.89	19.17	18.37	20.09
Ti (at.%)	0.00	4.62	5.95	10.16	6.15	5.32	4.76
Ni (at.%)	77.89	76.56	74.20	69.95	74.68	76.31	75.15
Sum	100.00	100.00	100.00	100.00	100.00	100.00	100.00

The mechanism of the TiO_2 inclusion is illustrated in Figure 8- 4. It is suggested that Ni ions would adsorb on surface of the TiO_2 aggregate particles suspending in the electrolyte to form Ni^{2+}–TiO_2 complex particles, and the complex particles diffuse to the substrate then reduction of the Ni ions on surface of the complex particle occurred to engulf the TiO_2 aggregate particle into the Ni–P layer [63, 124]. When the TiO_2 concentration is low with a small aggregate particle size in the electrolyte, the TiO_2 aggregate particles are easily included into the Ni–P as shown in Figure 8- 3(a) and Figure 8- 4(a). Because of the small aggregate particle size, a relatively smooth surface is obtained as exampled by the specimen shown in Figure 8- 2(b and c). With an increase in the TiO_2 concentration, average size of aggregate particles included into the Ni–P gradually increases and leads to a roughened surface condition as illustrated in Figure 8- 4(b). Figure 8- 2(d) demonstrates the result of the rough surface caused by the large aggregate particles in the moderate aggregate region (Figure 8- 3(b)). When size of the TiO_2 aggregate (or the Ni^{2+}–TiO_2 complex) particle reaches a critical size, a phenomenon named steric obstruction takes place to affect inclusion of the particles [30-37]. Steric obstruction is unfavorable for the inclusion as shown in Figure 8- 4(c). At first, removal of already–adsorbed oxide particles and decrease in the number of new particles adhering to the substrate occur because of collisions between particles near the substrate [125]. Secondly, inclusion of the particles is dependent on reduction of Ni ions adsorbed on the aggregate TiO_2 particle surface. Surface to volume ratio of the aggregate particle is lowered with an increase in the aggregate TiO_2 particle size. When the aggregate TiO_2 particle size is larger than the critical size, shortage of Ni ions adsorbed on surface of the particle makes it less likely to include the aggregate TiO_2 particle into the Ni–P before been removed away from the surface because of the collision [126]. In this study, average

size of the aggregate TiO_2 particle is suggested to be close to the critical size causing the steric obstruction when the TiO_2 concentration is at 30 g/L (Figure 8- 2(d) and Figure 8-4(b)), which is defined as the critical concentration resulting either maximum or minimum characteristics in the composite.

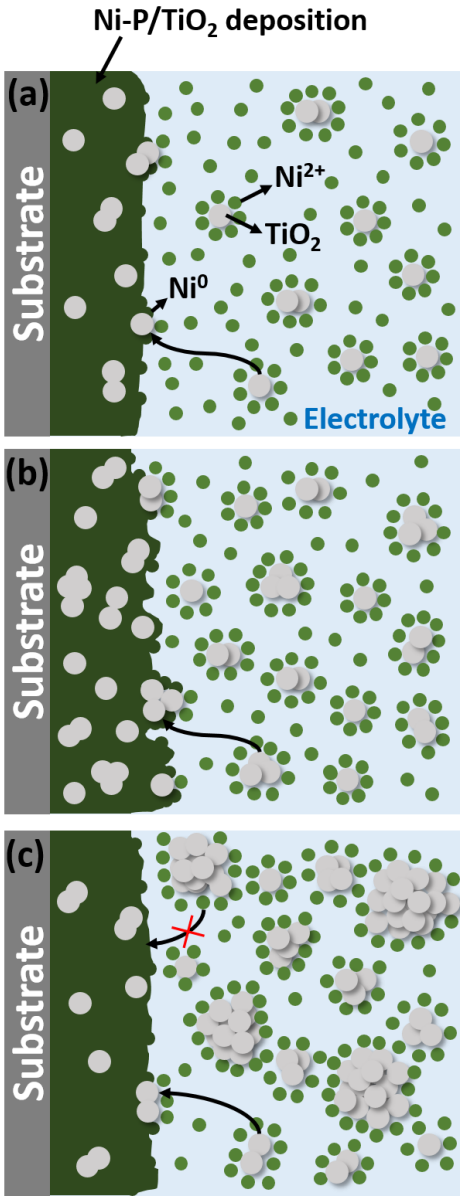

Figure 8- 4 Mechanism of TiO_2 inclusion with (a) TiO_2 concentration less than critical amount, (b) TiO_2 concentration at critical amount, and (c) TiO_2 concentration more than critical amount.

Figure 8- 5 shows elemental mapping results of the Ni–P/TiO_2 composite prepared with the electrolyte containing 30 g/L of TiO_2. Figure 8- 5(a) shows the rough surface condition of the composite layer deposited at the critical concentration. P, Ni, and Ti elements were homogeneously distributed on the surface indicating well–mixing of the electrolyte and homogeneous distribution of TiO_2 in the composite layer as indicated by results shown in Figure 8- 5(b) to (d).

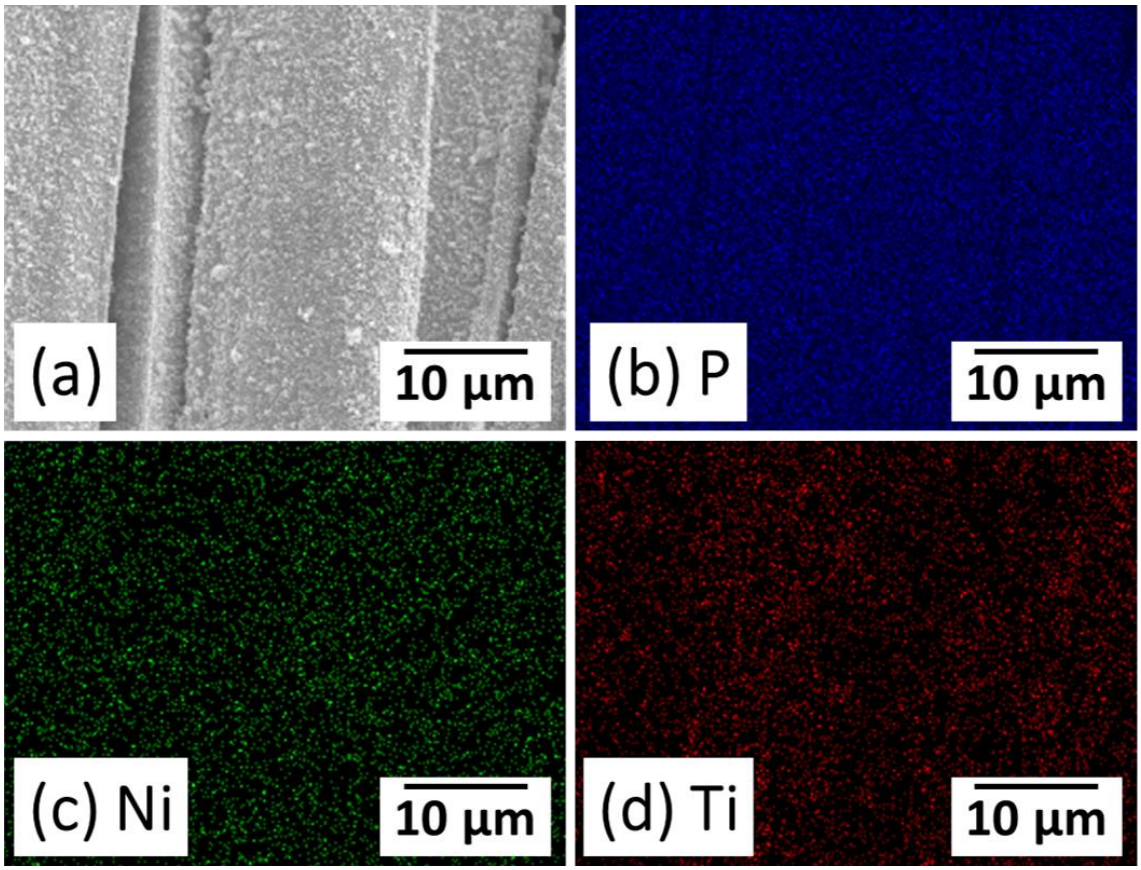

Figure 8- 5 Elemental mapping of Ni–P/TiO_2 composite layer deposited with 30 g/L TiO_2.

Figure 8- 6 shows XRD patterns of the Ni–P/TiO_2 deposited silk textiles at various TiO_2 concentrations in the electrolyte. A broad peak at around $2\theta = 45^o$ indicates amorphous structure of the Ni–P phase while a sharp peak at around $2\theta = 25^o$ suggests

anatase phase of the TiO_2. All specimens show TiO_2 diffraction peak at $2\theta = 25^{o}$ except for the one without the introduction of TiO_2 (0 g/L) in Figure 8- 6(a). No impurity or third phase was found in the XRD pattern within the detection limitation. TiO_2 concentration was approximately compared by the ratio between intensities of the Ni–P and the TiO_2 major peaks to qualitatively estimate the TiO_2 concentration in the Ni–P metallization layer. The ratio increased as concentration of TiO_2 in the electrolyte increased until it reached 30 g/L, which implies an increase in concentration of TiO_2 in the composite layer. Then the ratio decreased indicating a decrease in concentration of TiO_2 in the composite layer (Figure 8- 6e and f). This observation confirmed 30 g/L of TiO_2 in the electrolyte being the critical concentration to give the highest TiO_2 inclusion in the composite and the effect of steric obstruction (Figure 8- 3 and Figure 8- 4).

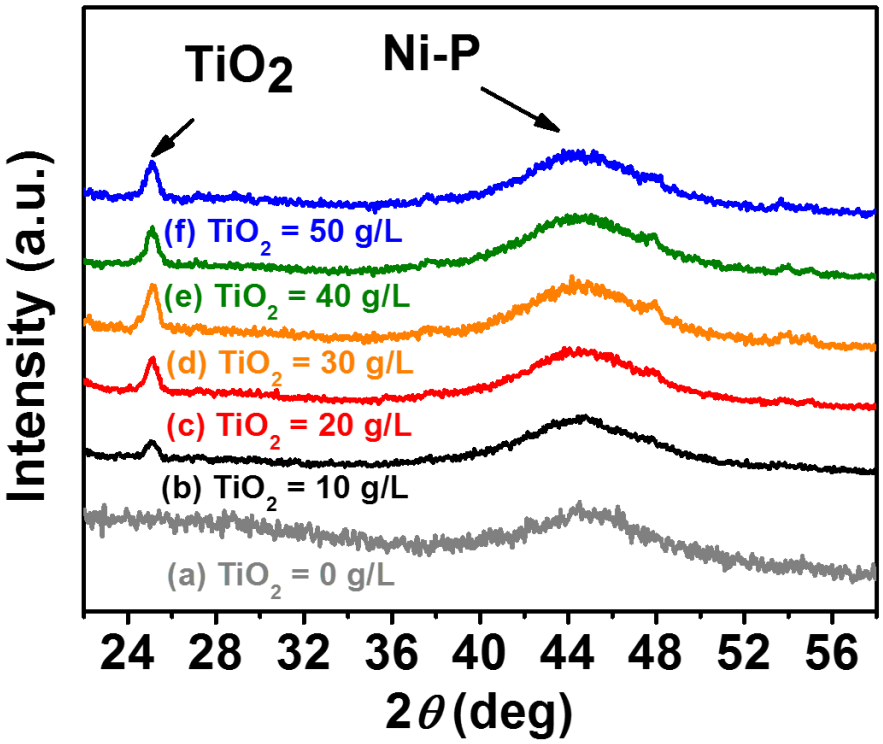

Figure 8- 6 X–ray diffraction patterns of Ni–P/TiO_2 deposition with various TiO_2 concentrations at (a) 0, (b) 10, (c) 20, (d) 30, (e) 40, and (f) 50 g/L, respectively.

Figure 8- 7 illustrates a positive correlation between the Ni–P/TiO_2 composite layer thickness and the TiO_2 concentration in the electrolyte before reaching the critical concentration. A SEM image was inserted in the bottom–right corner of Figure 8- 7 to show cross–section of the silk/Ni–P/TiO_2 composite layer deposited with 50 g/L TiO_2 in the electrolyte. The average growth rate was at 3.4 μm/hr before reaching the critical concentration. On the other hand, the thickness decreased slightly in the 40 g/L and 50 g/L specimens since large TiO_2 aggregate particles were formed to cause the steric obstruction (Figure 8- 3 and Figure 8- 4).

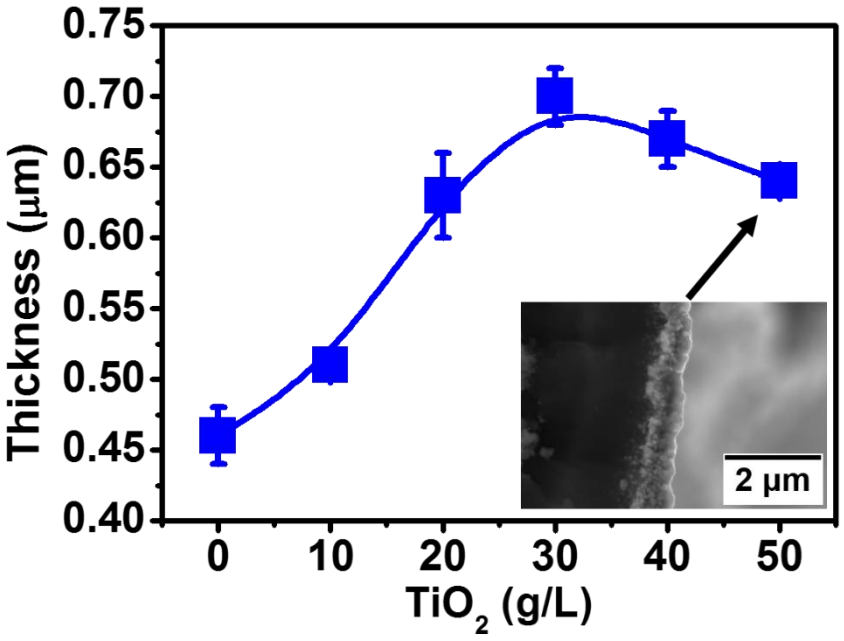

Figure 8- 7 Relationship of Ni–P/TiO_2 thickness and TiO_2 concentration in the electrolyte.

8.4 Electrical conductivity and adhesive tests

Electrical resistances of composite layers prepared at various TiO_2 concentrations in the Ni–P electrolyte are shown in Figure 8- 8. Since TiO_2 is a semiconductor, it owns lower electrical conductivity than Ni–P. TiO_2 thus shows negative

influence on the electrical conductivity in the Ni–P metallization layer. Ni–P metallization layer without TiO_2 inclusion performed the lowest electrical resistance. The electrical resistance increased monotonously with TiO_2 concentration in the electrolyte before reaching the critical concentration of TiO_2 (30 g/L) in the electrolyte. On the other hand, when the TiO_2 concentration in the electrolyte went beyond the critical concentration, the electrical resistance dropped owning to lower TiO_2 concentration in the Ni–P metallization layer. The inclusion trend of TiO_2 revealed by the electrical resistances is in accordance with the surface morphologies from SEM observations, the intensity ratios from XRD patterns, and the layer thickness results.

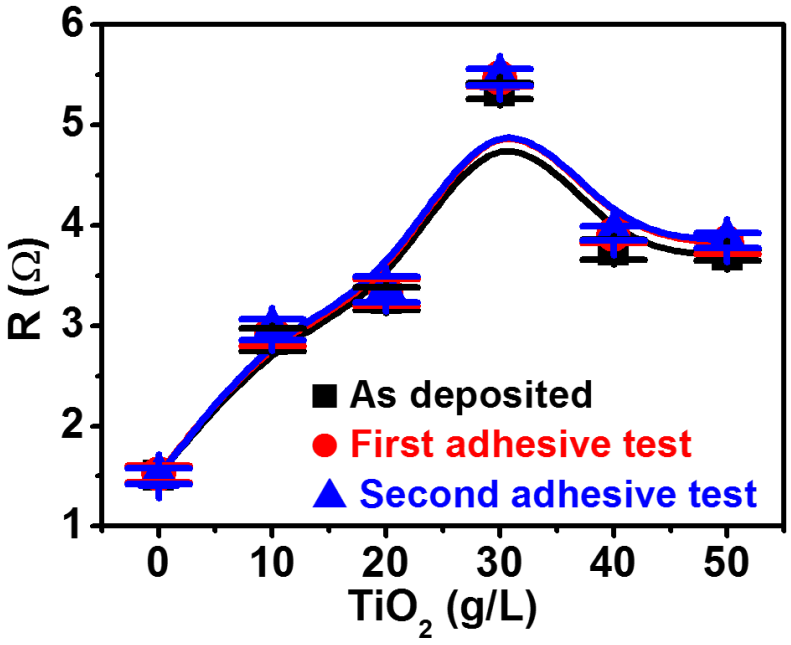

Figure 8- 8 The influence of included TiO_2 concentration to the electrical resistance of the silk/Ni–P/TiO_2 composite material.

Adhesive test evaluations are also shown in Figure 8- 8. Square symbol represents the as–deposited specimen, circle symbol depicts the first adhesive test, and the triangle one indicates the second adhesive test. Here, first adhesive test indicates one

cycle of the adhesive treatment is performed. Accordingly, second adhesive test means two cycles of the test are conducted. The results show that the electrical resistances persisted after the second adhesive test. Moreover, no significant difference was found between the first and second adhesive tests, and thus no further adhesive tests were conducted. These results demonstrate the high reliability and the robustness of the silk/Ni–P/TiO_2 composite materials and indicate that it is practicable for wearable devices.

8.5 Corrosion resistance

Figure 8- 9 shows the corrosion behaviors of the as–deposited silk/Ni–P composite and the silk/Ni–P/TiO_2 composite materials in 3.5 wt.% NaCl solution at both room temperature (Figure 8- 9(a)) and 37 ºC (body temperature) (Figure 8- 9(b)). The silk/Ni–P/TiO_2 composite fabricated with 30 g/L of TiO_2 in the electrolyte was chosen for the corrosion resistance evaluations. The corrosion potential (E_{corr}) and the corrosion current density (I_{corr}) are summarized in Table 8- 2. These results show that the Ni–P/TiO_2 composite have excellent corrosion resistance when compared with the pure Ni–P coating at both room temperature and 37ºC. According to the results, TiO_2 particles play an important rule for the improvement of the corrosion resistance. TiO_2 particles act as inert physical barriers to the initiation and development of defect corrosion and modify microstructure of the Ni–P metallization layer to improve the corrosion resistance. On the other hand, the E_{corr} of silk/Ni–P/TiO_2 is more positive than the silk/Ni–P indicating that the silk/Ni–P/TiO_2 composite is more inert than the silk/Ni–P due to the inclusion of inert TiO_2 particles. This result demonstrates that the composite material can persist in salty human sweat at both room temperature and body temperature, which is promising for applications in wearable devices.

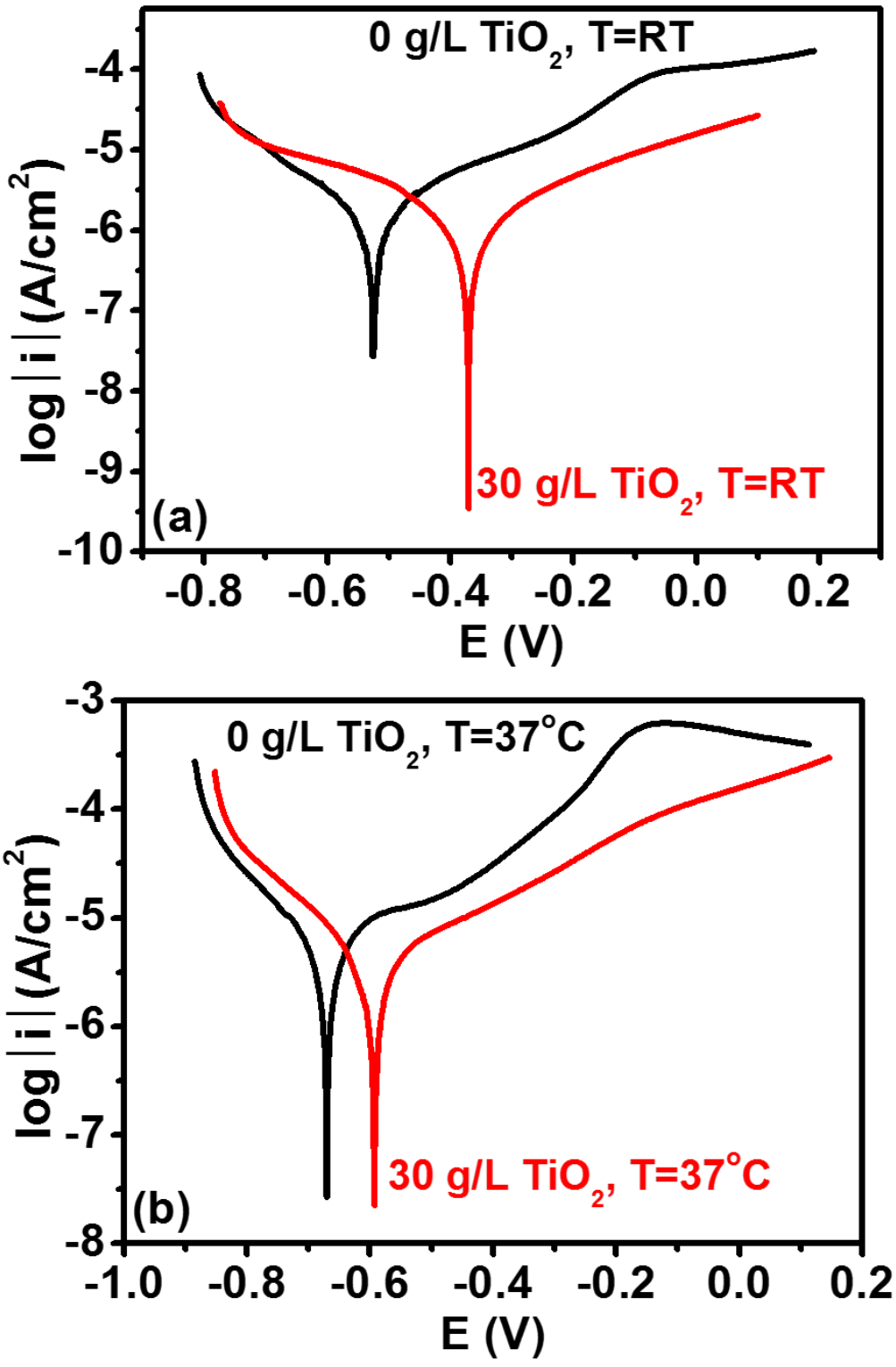

Figure 8- 9 Polarization curves of pure Ni–P coating and Ni–P/TiO_2 (3 g/L TiO_2 in the electrolyte) deposition on silk textile at (a) room temperature and (b) 37 ºC (body temperature).

Table 8- 2 Corrosion potentials and corrosion currents of the silk/Ni–P and silk/Ni–P/TiO_2 composites in 3.5 wt.% NaCl at (a) room temperature and (b) 37 ºC (body temperature).

(a) Room temperature	E_{corr} (V)	I_{corr} (A/cm^2)
Silk/Ni–P	-0.53	6.00×10^{-7}
Silk/Ni–P/TiO_2 (3g/L)	-0.37	1.56×10^{-7}
(b) 37 ºC (body temperature)	E_{corr} (V)	I_{corr} (A/cm^2)
Silk/Ni–P	-0.67	3.79×10^{-6}
Silk/Ni–P/TiO_2 (3g/L)	-0.59	1.02×10^{-6}

8.6 Photocatalytic activity assessment

To evaluate the practicability as photocatalytic materials, photocurrent generated from photoelectrochemical water splitting reaction was evaluated. The as–deposited sample was used as the photoanode. Figure 8- 10 shows the chronoamperometric I−t curves of the silk/Ni–P/TiO_2 composite materials recorded in 0.5 M Na_2SO_4 electrolyte illuminated by periodic white light at room temperature. The current density was corrected by considering overall surface area of the silk substrate. All the specimens showed an increasing anodic current when the illumination was turned on, which indicated the effective excitation, transfer, and collection of the electrons during the water splitting reaction. TiO_2 concentration in the metallization layer increased with TiO_2 concentration in the electrolyte, hence the current density increased monotonously from 0 g/L until the critical concentration (30 g/L). Because of the steric obstruction, less TiO_2 was included into the Ni–P metallization layer when the TiO_2 concentration went beyond the critical concentration, and the current density dropped. Again, the Ni–P/TiO_2 deposited with 30 g/L TiO_2 in the electrolyte showed the highest current density since it owns the greatest inclusion amount of TiO_2 in the Ni–P metallization layer.

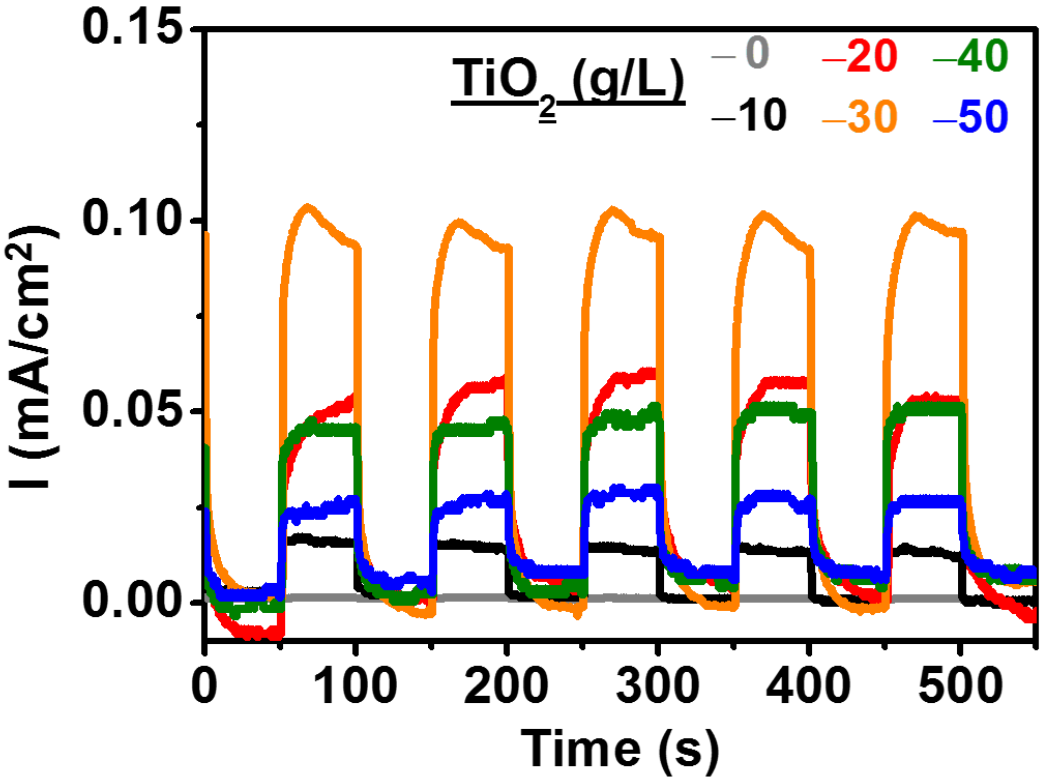

Figure 8- 10 Photocurrent density of the silk/Ni–P/TiO_2 incorporated materials illumined by periodic white light in 0.5 M Na_2SO_4 electrolyte at room temperature.

Figure 8- 11 shows the photocurrent densities of the as–deposited and the second adhesive test–treated specimens. The photocurrent densities persisted after the second adhesive test showing its high reliability and robustness. These results reveal that the adhesive properties were enhanced significantly while compare to literature [127, 128] due to the codeposition of Ni–P and TiO_2.

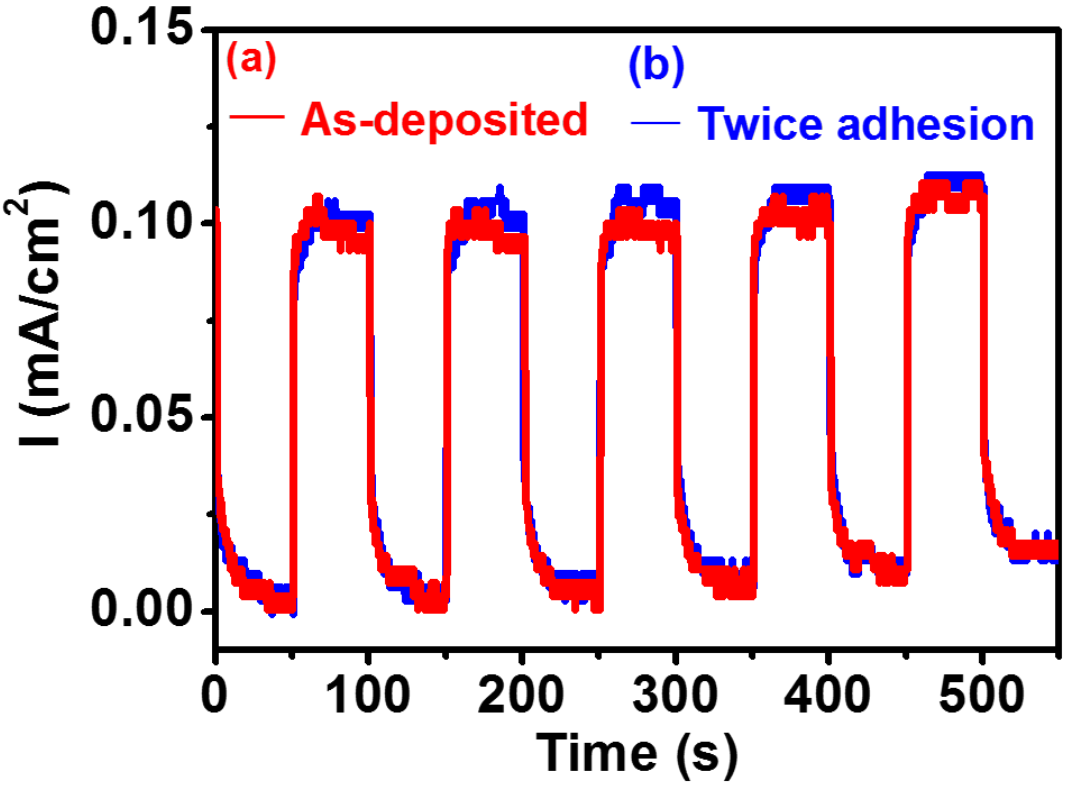

Figure 8- 11 Photocurrent density of (a) the as–deposited and (b) second adhesive test–treated silk/Ni–P/TiO_2 composite illumined by periodic white light in 0.5 M Na_2SO_4 electrolyte at room temperature.

Various evaluations were executed to reveal properties of the silk/Ni–P/TiO_2 composite materials in this study. The silk/Ni–P/TiO_2 composite materials possessed flexibility, electrical conductivity, high adhesive firmness, and high corrosion resistance. Photocurrent density was enhanced significantly by the inclusion of TiO_2 at its critical concentration in the electrolyte. Therefore, the results demonstrated potentials of the silk/Ni–P/TiO_2 composite materials for applications in flexible and functional wearable devices.

8.7 Brief summary for silk/Ni–P/TiO_2

Ni–P/TiO_2 composite layer was successfully co–deposited on silk textile by sc–

CO_2 assisted electroless plating. Common difficulties encountered in the conventional electroless plating were solved by the introduction of sc–CO_2, and the $Pd(acac)_2$ organometallic compounds were embedded into the silk substrate at around 330 nm in the depth. The composite layer on the silk were confirmed to be amorphous Ni–P phase and TiO_2 anatese phase. The composite showed the highest electrical resistance when the concentration of TiO_2 in the electrolyte was 30 g/L (critical concentration) since the highest TiO_2 concentration was included into the Ni–P metallization layer. High adhesive property of this silk/Ni–P/TiO_2 composite was revealed by the adhesive tests, the electrical resistance, and the photocatalytic activity evaluations. The Ni–P/TiO_2 showed higher corrosion resistance than that of Ni–P metallized silk without TiO_2 particles at both room temperature and body temperature. The highest photocatalytic activity was obtained in the composite with 30 g/L of TiO_2 particles in the electrolyte.

Chapter 9 General conclusions

Chapter 3

In this chapter silk textile was metallized by thin film Ni–P and Pt to fulfill the electrically conductive property, high corrosion resistance, and high wear resistance while keeps the silk textile flexible. Ni–P was chosen for its electrical conductivity, high wear resistance, high corrosion resistance, and low cost. Silk textile was firstly catalyzed by $Pd(acac)_2$, and the catalysts were successfully embedded into the silk textile around 200 nm in the depth without damaging the silk textile by the sc–CO_2 catalyzation. On the other hand, silk was damaged and lost its original structure after the CONV catalyzation in the acidic catalyzation solution of $SnCl_2/PdCl_2$. Ni–P was successfully metallized on the silk substrate and shows the homogeneous distribution of elemental composition. Ni–P metallization thickness shows positive correlation to the metallization time.

Three stages were defined according to the Ni–P coverage on the silk textile and electrical resistance, those Ni–P that is not fully covered was defined as the first stage showing high electrical resistance. Smooth metallization and full coverage of Ni–P was defined as second stage when the metallization time was extended. The lowest electrical resistance was observed in the second stage. Surface roughness increased with metallization time was observed and the Ni–P metallization with high surface roughness and full coverage was defined as third stage. The increased surface roughness was due to the severe diffusion control when the metallization was further extended. The electrical resistance was deteriorated in the third stage due to the high surface roughness. Adhesive

properties of the silk/Ni–P was also carried out in this study. Hardly did the electrical resistance changed after the adhesive tests showing the firmly adhesive property of the silk/Ni–P composite materials.

Corrosion resistance of silk/Ni–P was also evaluated. Corrosion resistance was measured after as–deposition, first adhesive test, and second adhesive test, respectively. No significant difference was observed after all the adhesive test and the corrosion resistance was comparable to the bulk Ni–P indicating the high corrosion resistance of the silk/Ni–P deposited on the silk textile. The results from surface morphology, electrical resistance, and corrosion resistance suggested that the Ni–P is a proper material for the application of wearable devices.

Chapter 4

Ni–P is a promising material for the wearable devices owing to the aforementioned advantages. Due to the concern of biocompatibility, the metallization was shifted to the Pt metallization to overcome the allergy reactions which would be triggered by Ni. $Pt(acac)_2$ catalyst was used to fulfill the full–Pt material. Similarly, $Pt(acac)_2$ catalysts were successfully embedded into the silk textile without damaging the silk structure by the sc–CO_2 catalyzation. Similar three stages were also found in the Pt metallization process and the thickness of Pt metallization also showed positive correlation to Pt the metallization time.

Test of Pt ion releasing rate by immersion test in the SBF at body temperature was carried out in this study to evaluate the biocompatibility of the silk/Pt composite materials. Only trace amount of Pt ion was observed while comparing to the daily Pt input and output to human body indicating the biocompatibility of the composite materials. The

results from surface morphology, electrical resistance, and immersion test suggested that the silk/Pt is a proper composite material for the application of biocompatible wearable devices and medical devices.

Chapter 5

For improving the metallization efficiency, the catalyst for the Pt metallization was shifted to $Pd(acac)_2$. Similarly, $Pd(acac)_2$ catalysts were successfully embedded into the silk textile without damaging the silk structure by the sc–CO_2 assisted catalyzation. Similar three stages were also found in the Pt metallization process and the thickness of Pt metallization also showed positive correlation to the metallization time. Pt metallization efficiency was improved due to the synchronization of the reduction of $Pd(acac)_2$ catalysts.

Since the catalyst was changed, identical immersion test in SBF at body temperature was also carried out to evaluate the biocompatibility of the composite materials. Only trace amount of Pd and Pt ions were observed while comparing to the daily input and output of Pd and Pt to human body indicating the biocompatibility of the $Pd(acac)_2$ catalyzed silk/Pt composite materials. Thus, the metallization efficiency was enhanced by the $Pd(acac)_2$ catalyst while the composite materials still show it biocompatibility. In addition, Pt metallization shows both high corrosion resistance in the 3.5 wt. NaCl solution and SBF. The results from surface morphology, electrical resistance, immersion test, and corrosion resistance suggested that the Pt is a proper material for the applications of biocompatible wearable devices and medical devices.

Chapter 6

Sc–CO_2 was introduced into the metallization solution to improve the Pt

metallization properties. $Pd(acac)_2$ catalyst was chosen for its high metallization efficiency. Similarly, $Pd(acac)_2$ catalysts were successfully embedded into the silk textile without damaging the silk structure by the sc–CO_2 assisted catalyzation. Only two stages were found in the sc–CO_2 metallization since the diffusivity of metal ions was enhanced by the bouncing sc–CO_2/surfactant micelles in the electrolyte.

Due to the smoothened Pt metallization, only two stages were defined according to the surface morphology and electrical resistance. Since the surface roughness of Pt metallization was suppressed by the introduction of sc–CO_2 into the metallization solution, third stage was not observed and thus no deteriorated electrical conductivity was found. The Pt metallization properties was improved by the introduction of sc–CO_2 to the Pt metallization electrolyte.

Test of ion releasing rate by immersion test in the SBF was carried out to evaluate the biocompatibility of the sc–CO_2 assisted Pt metallization composite materials. Only trace amount of Pt ion was observed while comparing to the daily Pt input and output to human body indicating the biocompatibility of the silk/Pt composite materials. The results from surface morphology, electrical resistance, and immersion test suggested that the sc–CO_2 assisted Pt metallization is a proper material for the applications of biocompatible wearable devices and medical devices.

In chapter 3, Ni–P and Pt were metallized on the silk textile, respectively. Ni–P owns the efficient metallization and low cost while Pt owns the biocompatibility and high corrosion resistance. Both of the composite are promising materials for the wearable devices according to the evaluations of electrical resistance, corrosion resistance, immersion test, and adhesive tests.

Chapter 7

For functionalizing the silk textile, Au was metallized on the silk substrate and ZnO was deposited on the Au metallized silk substrate. $Pd(acac)_2$ catalyst was selected for its low cost and high efficiency in the metallization. Similarly, $Pt(acac)_2$ catalysts were successfully embedded into the silk textile without damaging the silk structure by the sc–CO_2 assisted catalyzation. A thin Ni–P was deposited on the silk substrate for acting as a diffusion barrier layer between silk and Au metallization. Similar three stages were also found in the CONV Au metallization process and the thickness of Au metallization also showed positive correlation to the Au metallization time.

ZnO was successfully deposited on the Au metallized silk. The coverage of ZnO decreased with increasing H_2O_2 concentration in the solution. Since the H_2O_2 was the OH^- source of OH^-, the substrate surface became more alkaline when there are more H_2O_2 in the electrolyte. Thus, ZnO dissolved back to the solution when the surface pH went beyond 12 and the coverage of ZnO decreased accordingly. When he H_2O_2 at 0.2 wt.%, ZnO shows the highest crystallinity, therefore, the silk/Au/ZnO composite shows the highest photocurrent density in the photocatalytic activity test. The results from the electrical resistance, adhesive test, and photocatalytic activity evaluations suggested that the silk/Au/ZnO composite material is a proper material for the application of functional wearable devices.

Chapter 8

Ni–P/TiO_2 composite layer was successfully co–deposited on silk textile by sc–CO_2 assisted electroless plating. Common difficulties encountered in the conventional electroless plating were solved by the introduction of sc–CO_2, and the $Pd(acac)_2$

organometallic compounds were embedded into the silk substrate at around 330 nm in the depth. The composite layer on the silk were confirmed to be amorphous Ni–P phase and TiO_2 anatese phase. The composite showed the highest electrical resistance when the concentration of TiO_2 in the electrolyte was 30 g/L (critical concentration) since the highest TiO_2 concentration was included into the Ni–P metallization layer. High adhesive property of this silk/Ni–P/TiO_2 composite was revealed by the adhesive tests, the electrical resistance, and the photocatalytic activity evaluations. The Ni–P/TiO_2 showed higher corrosion resistance than that of Ni–P metallized silk without TiO_2 particles at both room temperature and body temperature. The highest photocatalytic activity was obtained in the composite with 30 g/L of TiO_2 particles in the electrolyte.

Chapter 10 List of achievements and others

10.1 Awards

• Best poster award, Taiwan-Japan Joint Symposium & Nano Engineering and Microsystem Technology Conference

May 2018

• Best poster award, second place, The Minerals, Metals & Materials society (TMS) 2018

Mar. 2018

• Thin Film Society (TSF) Special Award (Oral presentation)

Oct. 2017

• Taiwan Association for Coating and Thin Film Technology (TACT) 2017 Gold Award

Oct. 2017

• Research Fellow of Japan Society for the Promotion of Science, JSPS

Apr. 2017-Sept. 2018

• Best Paper Award, 15th Symposium on Development of Supercritical Fluid Technology and Application, Taiwan Supercritical Fluid Association (TSCFA)

Sept. 2016

• Interchange Association international student scholarship, Japan–Taiwan Interchange Association

Apr. 2016-now

• Research assistantship, Tokyo Tech

Oct. 2015-now

• 2015 Honors Scholarship, Japan Student Services Organization (JASSO)

Oct. 2015

10.2 Publications

10.2.1 International Journal

1. **W.-T. Chiu**, C.-Y. Chen, T.-F. M. Chang, Y. Tahara, T. Hashimoto, H. Kurosu, and M. Sone, "Platinum Coating on Silk by a Supercritical CO_2 Promoted Metallization Technique for Applications of Wearable Devices", *Surface & Coating Technology*, doi.org/10.1016/j.surfcoat.2018.02.070 (In press). SCI, IF: 2.589
2. **W.-T. Chiu**, C.-Y. Chen, T.-F. M. Chang, Y. Tahara, T. Hashimoto, H. Kurosu, and M. Sone, "Fabrication and Photocatalytic Performance of Au/ZnO Layered Structure on Silk Textile for Flexible Device Applications", *Electrochimica Acta*, **253**(1) (2017) 39-46. SCI, IF: 4.798
3. **W.-T. Chiu**, Y. Tahara, C.-Y. Chen, T.-F. M. Chang, T. Hashimoto, H. Kurosu, and M. Sone, "Fundamental Property Assessments of Biocompatible Silk–Pt Composite Prepared by Supercritical Carbon Dioxide Promoted Electroless Plating" *ACS Industrial & Engineering Chemistry Research*, **56**(31) (2017) 8864-8871. SCI, IF: 2.567
4. **W.-T. Chiu**, Y. Tahara, C.-Y. Chen, T.-F M. Chang, T. Hashimoto, H. Kurosu, and M. Sone, "A Supercritical CO_2 Promoted Electroless Ni-P Plating on Silk and Their Fundamental Characteristics Investigations", *Journal of The Electrochemical Society*, **164**(7) (2017) D406-D411. SCI, IF: 3.014
5. **W.-T. Chiu**, Y. Tahara, C.-Y. Chen, T.-F M. Chang, T. Hashimoto, H. Kurosu, and M.

Sone, “Silk-Pt Composite Integration by Supercritical Carbon Dioxide Assisted Electroless Plating for Medical Devices Application”, *Microelectronic Engineering*, **175**(C) (2017) 34-37. SCI, IF: 1.277

10.2.2 Domestic Journal

1. M. Sone, M. Sano, **W.-T. Chiu**, T.-F. M. Chang, H. Kurosu, and T. Hashimoto, “超臨界二酸化炭素を用いた生体適合性貴金属被覆高分子繊維の創成”, ケミカルエンジニアリング, **6** (2016).

10.2.3 Invited Articles

1. **W.-T. Chiu**, M. Sano, C.-C. Wang, T.-F. M. Chang, C.-Y. Chen, H. Kurosu, M. Sone, “以超臨界二氧化碳無電鍍達成應用於穿戴式裝置之複合材料”, *ITRI Materialsnet*, October (2017).

10.2.4 Book

1. **W.-T. Chiu**, B.-H. Woo, M. Sano, T.-F. M. Chang, C.-Y. Chen, T. Hashimoto, H. Kurosu, and M. Sone, “Highly Reliable Metallization on Polymer and Their Fundamental Characteristics toward Wearable Devices Applications”, *Advances in Biosensors: Reviews*, IFSA Publishing **2** (2018).

10.2.5 International Conference

1. **W.-T. Chiu**, C.-Y. Chen, T.-F. M. Chang, T. Hashimoto, H. Kurosu, and M. Sone, “Silk/Ni–P/TiO_2 Composite Material Prepared by Supercritical CO_2 Promoted Electroless Plating for Flexible Photocatalytic Device Applications” *44th International Conference on Micro and Nanoengineering*, Copenhagen, Denmark,

September, 2018. (abstract accepted) *Oral presentation

2. **W.-T. Chiu**, C.-Y. Chen, T.-F. M. Chang, T. Hashimoto, H. Kurosu, and M. Sone, "Co-Deposition of Ni–P and TiO_2 on Silk Textile by Supercritical CO_2 Promoted Electroless Plating for Gas Sensor Applications" *The 2nd Taiwan-Japan Joint Symposium*, Taipei, Taiwan, May, 2018. *Best poster award
3. **W.-T. Chiu**, C.-Y. Chen, T.-F. M. Chang, T. Hashimoto, H. Kurosu, and M. Sone, "Co-deposition of Ni-P and P25 on Silk Textile by Supercritical CO_2 Promoted Electroless Plating for Flexible Photocatalyst Applications", *22nd Topical Meeting of the International Society of Electrochemistry*, Tokyo, Japan, April, 2018.
4. **W.-T. Chiu**, C.-Y. Chen, T.-F. M. Chang, T. Hashimoto, H. Kurosu, and M. Sone, "Composite of ZnO/Au Hybrid Structure on Silk Textile for Flexible Photocatalyst Application", *TMS 2018 147th Annual Meeting & Exhibition*, Arizona, USA, March, 2018. *Oral presentation
5. **W.-T. Chiu**, C.-Y. Chen, T.-F. M. Chang, T. Hashimoto, H. Kurosu, and M. Sone, "ZnO Synthesis on the Au Metallized Silk Textile for Flexible Photocatalyst Application", *TMS 2018 147th Annual Meeting & Exhibition*, Arizona, USA, March, 2018. *Best poster award, second place
6. **W-T Chiu**, H. Tang, C.-Y. Chen, T.-F. M. Chang, H. Kurosu and M. Sone, "Realization of flexible and photocatalytic ZnO/Au/silk composite materials as components in wearable devices", *16th Symposium on Development of Supercritical Fluid Technology and Application*, Taichung, Taiwan, October, 2016.
7. **W.-T. Chiu**, Y. Tahara, C.-Y Chen, T.-F. M. Chang, T. Hashimoto, H. Kurosu, and M. Sone, "Highly Reliable Platinum Coating on Silk via an Efficient Supercritical CO_2 Promoted Electroless Plating for Biocompatible Wearable Devices", *TACT 2017*

International Thin Films Conference, Hualien, Taiwan, October, 2017. *Oral presentation *Thin Film Society (TSF) Special Award (Oral presentation) * Taiwan Association for Coating and Thin Film Technology (TACT) 2017 Gold Award

8. **W.-T. Chiu**, C.-Y. Chen, T.-F. M. Chang, T. Hashimoto, H. Kurosu, and M. Sone, "ZnO/Au Hybrid Layered Structure on Silk Textile Prepared by Supercritical Carbon Dioxide Promoted Electrodeposition for Applications in Flexible Multifunction Electronic Devices", *43rd International Conference on Micro and Nano Engineering*, Braga, Portugal, September, 2017. *Final run in the poster competition
9. **W.-T. Chiu**, C.-Y. Chen, T.-F. M. Chang, T. Hashimoto, H. Kurosu, and M. Sone, "Metallization on Silk Utilizing Supercritical Carbon Dioxide Assisted Electroless Plating for Wearable Device", *PRiME 2016/230th ECS Meeting*, Hawaii, USA, October, 2016.
10. **W.-T. Chiu**, Y. Tahara, C.-Y Chen, T.-F. M. Chang, T. Hashimoto, H. Kurosu, and M. Sone, "Fabrication of Pt Metallization on Silk via Supercritical Carbon Oxide-Assisted Electroless Plating for Wearable Medical Devices", *2nd International Conference and Expo on Separation Techniques*, Valencia, Spain, September, 2016. *Oral presentation
11. **W.-T. Chiu**, Y. Tahara, C.-Y. Chen, T.-F. M. Chang, T. Hashimoto, H. Kurosu, and M. Sone, "Fabrication of Pt-Silk Composite Material by a Novel Catalyzation in Supercritical Carbon Dioxide for the Application of Medical Devices", *42nd International Conference on Micro and Nano Engineering*, Vienna, Austria, September, 2016.
12. **W.-T. Chiu**, M. Sano, C.-Y. Chen, T.-F. M. Chang, T. Hashimoto, H. Kurosu, and M. Sone, "Metallization of textiles by electroless plating with supercritical carbon

dioxide for the applications in wearable devices", *15th Symposium on Development of Supercritical Fluid Technology and Application*, Kaohsiung, Taiwan, September, 2016. *Oral presentation *Best Paper Award, 15th Symposium on Development of Supercritical Fluid Technology and Application, Taiwan Supercritical Fluid Association (TSCFA)

13. T.-F. M. Chang, **W.-T. Chiu**, Y. Tahara, C.-Y. Chen, T. Hashimoto, H. Kurosu, and M. Sone. "Fabrication of High Biocompatible Pt-Nylon and Pt-Silk Composite Materials by Supercritical Carbon Dioxide-Assisted Metallization Method", *4th International Conference on Integrative Biology*, Berlin, Germany, July, 2016.
14. **W.-T. Chiu**, Y. Tahara, C.-Y. Chen, T.-F. Mark Chang, T. Hashimoto, H. Kurosu, and M. Sone, "Platinum Electroless Plating of Silk Utilizing Supercritical Carbon Dioxide", *19th Topical Meeting of the International Society of electrochemistry*, Auckland, New Zealand, April, 2016.

10.3 Research Experience

Tokyo Institute of Technology, Yokohama, Japan *Research assistant, Oct. 2015-now*

[Thesis project] Functionalization of silk textile via supercritical CO_2 promoted electrochemical method

(Granted by Grant-in-Aid for Scientific Research (JSPS KAKENHI Grant Number 17J07395) and the Grant-in-Aid for Scientific Research (B) (JSPS KAKENHI Grant Number 26282013))

- Ni-P, Pt, and Au metallized silk textile via supercritical carbon dioxide promoted electroless plating for wearable devices.
- Biocompatibility assessments of metallized silk composite materials by immersion tests.

- Electrical resistance, corrosion resistance, and adhesive strength evaluations of silk-metal materials for achieving highly reliable applications.
- ZnO fabrication on gold metallized silk by cathodic deposition and its photoelectro-chemical evaluation for functional wearable devices.

[Project] Supercritical CO_2 assisted Pt electroless plating on silk textile for wearable device applications.

(Granted by Grant-in-Aid for Scientific Research (JSPS KAKENHI Grant Number 17J07395)

- Pt metallization on silk textile via supercritical CO_2 promoted electroless plating for the applications of wearable electronic and medical devices.
- Reliability assessments of the composite materials for fulfill the applications.

[Project] Construct the instrument for polymerization of polyaniline and atomic layer gold insertion.

(Granted by Casio)

- Cooperation with Georgia Institute of Technology
- Constructed the devices for the polymerization of polyaniline and build up the flow system for atomic gold layer insertion.

[Project] PET catalyzation under supercritical carbon dioxide for wearable device applications.

(Granted by Industrial Technology Research Institute of Taiwan)

- Cooperation with Industrial Technology Research Institute of Taiwan
- Activated PET fiber by palladium(II) acetylacetonate using supercritical carbon dioxide promoted catalyzation for the applications of wearable devices.

[Project] Investigate the chemical bonding between textile surface and catalyst by solid

state NMR

(Granted by Grant-in-Aid for Scientific Research (B) (JSPS KAKENHI Grant Number 26282013))

- Cooperation with Nara Women's University
- Catalyzed silk and nylon 66 fabric via supercritical carbon dioxide catalyzation technique and observe the catalyst-substrate interaction by NMR.

Georgia Institute of Technology, Atlanta, US *Visiting Research Student, Apr. 2017*

- Polymerization of polyaniline by electrochemical method.
- Gold atomic layer deposition on the polyaniline and its performance in alcohol oxidation.

10.4 Acknowledgement

Four years ago, I met Sone sensei in IUMRS international conference which was hold in Taipei, Taiwan. That is the beginning of this three-year doctoral life. Before the entrance examination, I faced some difficulties, but Sone sensei was so friendly to me and gave me many assistances. Fortunately, I came to Sone lab after solving some troubles. Sone sensei, as usual, is always kind to every students, and always has a good sense in educating, communicating, and researching. Students in Sone lab usually have the opportunities to go to international conferences to explore our global prospect. I always learnt a lot from the international conferences and expanded my academic contact all over the world. I really appreciated these opportunities which I cannot have in other places. Before graduating, I suffered from job hunting. Sone sensei gave me tons of assistances, and everything was settled down in the end. Without all the assistances from Sone sensei, I wouldn't be able to survive from all the difficulties. There are still one billion of things that I have to express my thanks to Sone sensei but one billion thanks still cannot convey my gratitude to Sone sensei. Even though I am leaving Sone lab soon, I feel proud to be a member in Sone lab, and I hope Sone sensei can feel proud of me in the future.

Similarly, four years ago, I met Dr. Chang in IUMRS international conference. Oh no, I think I met Dr. Chang earlier than the time I met Sone sensei. I met you when I was a master student in Tsing Hua. Before entering Tokyo Tech, Dr. Chang already gave me tons of assistances, they can be from life supports in Japan to academic issues. Without your help, I cannot come to Sone lab that smoothly. After entering, every time I asked you “do you have free time now? I would like to discuss something with you”, your answers are always “YES”. You always gave me some good advices and helpful comments. You always have good sense in presentation and have a strong fundamental in

electrochemistry and material sciences, I always benefit a lot from you. In daily life, whenever there are any benefits, you always fight that for us such as international conferences and some life supports. And Dr. Chen, you always have a good sense in some trivial things which are always important but are always neglected by us. For example, I cannot imagine that we go to the international conferences without you. You always settled everybody down quickly and smoothly.

I would like to thank my previous advisors, who are Prof. Sinn-Wen Chen and Prof. Yang-Yuan Chen in National Tsing Hua University and Academia Sinica. I really appreciated your understanding and the opportunity letting me be a member in your lab. Without your helps, I would not be able to come to Japan and get my PhD degree.

I also want to express my appreciations to my dear friends in Sone lab and out of Sone lab. Tang and I always have some stupid conversations. It makes the daily life funny and I always like to talk something stupid to you. I wish you have an even brighter life than now in the future. My junior Teranishi-chan always supported me in learning Japanese and always be on my side when I faced almost the greatest setback in my life last year. My junior Ken Hashigata, without you, I might be in heaven right now, you are a life saver lololol. I always like to talk to you, something serious and something stupid. I will haunt you till I go to the tomb. And please remember to dress in pink when you come to my funeral. All the master students in Sone lab, you always helped me in translations. Every time I asked for your helps, I feel sorry to you since it was really time consuming and troublesome. But you always helped my with the translation without any complain. I really appreciate your kindness, especially Tei-kun, Igawa-kun, Nakajima-kun, and Nitta-kun. It is really nice to have these cute juniors. My co-worker in Nakamoto

lab PJ, oh well although I still cannot spell your name, but it is my pleasure to be your friend. You are a dedicated student, a good listener, and a good advice giver. I always like to talk to you and I wish you a fruitful PhD life in the coming two years. Dr. Hsu, I always learnt a lot of Japanese and the way living in Japan. It was always fun to have some conversions with you. And you always have a good sense in beauty, life, and foods.

Finally, I would like to express my gratitude to my family. Every time I went back to Taiwan, you always let me be a piece of trash sleeping almost 16 hours per day and feed me as a poultry. And thanks for not blocking me from being an international student in Japan. Although I faced the greatest setback in Japan last year, I never regret that I came to Japan. And I am sorry that I will not go back to Taiwan after my graduation. But I believe that I will go back one day (probably…)

10.5 Reference

[1] K. Suganuma, Introduction, Introduction to Printed Electronics, Springer2014, pp. 1-22.

[2] K. Hung, Y.-T. Zhang, B. Tai, Wearable medical devices for tele-home healthcare, Engineering in Medicine and Biology Society, 2004. IEMBS'04. 26th Annual International Conference of the IEEE, IEEE, 2004, pp. 5384-5387.

[3] G.O. Mallory, J.B. Hajdu, Electroless plating: fundamentals and applications, William Andrew1990.

[4] J.R. Henry, Electroless (autocatalytic) plating, Metal finishing, 99 (2001) 424-435.

[5] M. Saito, Electrochemical Studies on Chemical Copper Plating, J. Metal. Finish. Soc. Japan, 16 (1965) 300.

[6] K.M. Gorbunova, M.V. Ivanov, V.P. Moiseev, Electroless Deposition of Nickel‐Boron Alloys Mechanism of Process, Structure, and Some Properties of Deposits, Journal of The Electrochemical Society, 120 (1973) 613-618.

[7] K. Holbrook, P. Twist, Hydrolysis of the borohydride ion catalysed by metal–boron alloys, Journal of the Chemical Society A: Inorganic, Physical, Theoretical, (1971) 890-894.

[8] F. Pearlstein, R. Weightman, Electroless Deposition of Ag Using Dimethylamine Borane, Plating, 61 (1974) 154-157.

[9] Y. Okinaka, An Electrochemical Study of Electroless Gold‐Deposition Reaction, Journal of The Electrochemical Society, 120 (1973) 739-744.

[10] I. Ohno, O. Wakabayashi, S. Haruyama, Anodic Oxidation of Reductants in Electroless Plating, Journal of The Electrochemical Society, 132 (1985) 2323-2330.

[11] J.E.A.M. Van Den Meerakker, On the mechanism of electroless plating. II. One

mechanism for different reductants, Journal of Applied Electrochemistry, 11 (1981) 395-400.

[12] C. De Minjer, P. vd Boom, The Nucleation with SnCl2 - PdCl2 Solutions of Glass Before Electroless Plating, Journal of The Electrochemical Society, 120 (1973) 1644-1650.

[13] T. Osaka, H. Nagasaka, F. Goto, An electron diffraction study on mixed PdCl2/SnCl2 catalysts for electroless plating, Journal of The Electrochemical Society, 127 (1980) 2343-2346.

[14] T. Osaka, H. Takematsu, K. Nihei, A study on activation and acceleration by mixed PdCl2/SnCl2 catalysts for electroless metal deposition, Journal of The Electrochemical Society, 127 (1980) 1021-1029.

[15] M. Sano, Y. Tahara, C.-Y. Chen, T.-F.M. Chang, T. Hashimoto, H. Kurosu, T. Sato, M. Sone, Application of supercritical carbon dioxide in catalyzation and Ni-P electroless plating of nylon 6, 6 textile, Surface and Coatings Technology, 302 (2016) 336-343.

[16] W.-T. Chiu, Y. Tahara, C.-Y. Chen, T.-F.M. Chang, T. Hashimoto, H. Kurosu, M. Sone, A Supercritical CO2 Promoted Electroless Ni-P Plating on Silk and Their Fundamental Characteristics Investigations, Journal of The Electrochemical Society, 164 (2017) D406-D411.

[17] M. McHugh, V. Krukonis, Supercritical fluid extraction: principles and practice, Elsevier2013.

[18] S.P. Sawan, S.P. Sawan, Supercritical fluid cleaning: fundamentals, technology and applications, Elsevier1998.

[19] G. Brunner, Gas extraction: an introduction to fundamentals of supercritical fluids and the application to separation processes, Springer Science & Business Media2013.

[20] H. Adachi, K. Taki, S. Nagamine, A. Yusa, M. Ohshima, Supercritical carbon dioxide assisted electroless plating on thermoplastic polymers, The Journal of Supercritical Fluids, 49 (2009) 265-270.

[21] S. Tengsuwan, M. Ohshima, Electroless nickel plating on polypropylene via hydrophilic modification and supercritical carbon dioxide Pd-complex infusion, The Journal of Supercritical Fluids, 69 (2012) 117-123.

[22] T.-F.M. Chang, M. Sone, Function and mechanism of supercritical carbon dioxide emulsified electrolyte in nickel electroplating reaction, Surface and Coatings Technology, 205 (2011) 3890-3899.

[23] C. Gorla, N. Emanetoglu, S. Liang, W. Mayo, Y. Lu, M. Wraback, H. Shen, Structural, optical, and surface acoustic wave properties of epitaxial ZnO films grown on (0112) sapphire by metalorganic chemical vapor deposition, Journal of Applied Physics, 85 (1999) 2595-2602.

[24] B. Panigrahy, M. Aslam, D. Misra, D. Bahadur, Polymer-mediated shape-selective synthesis of ZnO nanostructures using a single-step aqueous approach, CrystEngComm, 11 (2009) 1920-1925.

[25] C.-H. Ku, J.-J. Wu, Aqueous solution route to high-aspect-ratio zinc oxide nanostructures on indium tin oxide substrates, The Journal of Physical Chemistry B, 110 (2006) 12981-12985.

[26] Q. Zhang, C. Tian, A. Wu, T. Tan, L. Sun, L. Wang, H. Fu, A facile one-pot route for the controllable growth of small sized and well-dispersed ZnO particles on GO-derived graphene, Journal of Materials Chemistry, 22 (2012) 11778-11784.

[27] J.R. Henry, Electroless (autocatalytic) plating, Metal Finishing, 97 (1999) 431-442.

[28] A. Brenner, G.E. Riddell, Nickel plating on steel by chemical reduction, Plating and

surface finishing, 85 (1998) 54-55.

[29] A. Brenner, G.E. Riddell, Deposition of nickel and cobalt by chemical reduction, J. Res. Nat. Bur. Stand, 39 (1947) 385-395.

[30] G. Gutzeit, Industrial Nickel Coating by Chemical Catalytic Reduction, Anti-Corrosion Methods and Materials, 3 (1956) 208-208.

[31] P. Cavallotti, G. Salvago, STUDIES ON CHEMICAL REDUCTION OF NICKEL AND COBALT BY HYPOPHOSPHITE. PT. 2. CHARACTERISTICS OF THE PROCESS, Electrochim metallorum, 3 (1968) 239-266.

[32] G. Salvago, P. Cavallotti, CHARACTERISTICS OF THE CHEMICAL REDUCTION OF NI ALLOYS WITH HYPOPHOSPHITE, Plating, 59 (1972) 665-671.

[33] J.P. Rondin, H. Hintermann, A calorimetric study of the electroless deposition of nickel, Journal of The Electrochemical Society, 117 (1970) 160-167.

[34] S. Mizuhashi, C.E.J. Cordonier, H. Matsui, H. Honma, O. Takai, Comparative study on physical and electrochemical characteristics of thin films deposited from electroless platinum plating baths, Thin Solid Films, 619 (2016) 328-335.

[35] S. Mizuhashi, C.E. Cordonier, H. Honma, O. Takai, Stabilization of an Electroless Platinum Plating Bath Using S-Bearing Additives, Journal of The Electrochemical Society, 162 (2015) D497-D502.

[36] C.R.K. Rao, M. Pushpavanam, Electroless deposition of platinum on titanium substrates, Materials Chemistry and Physics, 68 (2001) 62-65.

[37] J.J. Pak, S.-E. Cha, H.-J. Ahn, S.-K. Lee, Fabrication of ionic polymer metal composites by electroless plating of Pt, Proc. of the 32nd Intl. Symp. on Robotics, 2001.

[38] N. Lago, K. Yoshida, K.P. Koch, X. Navarro, Assessment of biocompatibility of chronically implanted polyimide and platinum intrafascicular electrodes, IEEE

Transactions on Biomedical Engineering, 54 (2007) 281-290.

[39] H. Hoffmann, G. Fischer, Electrical conductivity in thin and very thin platinum films, Thin Solid Films, 36 (1976) 25-28.

[40] M. Pourbaix, J. Van Muylder, N. De Zoubov, Electrochemical properties of the platinum metals, Platinum Metals Review, 3 (1959) 47-53.

[41] A. Buch, Pure metals properties: a scientific and technical handbook, (1999).

[42] T. Fusayama, T. Katayori, S. Nomoto, Corrosion of gold and amalgam placed in contact with each other, Journal of dental research, 42 (1963) 1183-1197.

[43] J.R. Davis, ASM specialty handbook: heat-resistant materials, Asm International1997.

[44] Y. Okinaka, ELECTROLESS GOLD DEPOSITION USING BOROHYDRIDE OR DIMETHYLAMINE BORANE A REDUCING AGENT, Plating, 57 (1970) 914-920.

[45] A.B. Djurišić, Y.H. Leung, A.M.C. Ng, Strategies for improving the efficiency of semiconductor metal oxide photocatalysis, Materials Horizons, 1 (2014) 400-410.

[46] E. Pelizzetti, C. Minero, Metal oxides as photocatalysts for environmental detoxification, Comments on Inorganic Chemistry, 15 (1994) 297-337.

[47] T. Hisatomi, J. Kubota, K. Domen, Recent advances in semiconductors for photocatalytic and photoelectrochemical water splitting, Chemical Society Reviews, 43 (2014) 7520-7535.

[48] M.R. Hoffmann, S.T. Martin, W. Choi, D.W. Bahnemann, Environmental applications of semiconductor photocatalysis, Chemical reviews, 95 (1995) 69-96.

[49] A. Fujishima, K. Honda, Electrochemical photolysis of water at a semiconductor electrode, nature, 238 (1972) 37-38.

[50] H. Wang, L. Zhang, Z. Chen, J. Hu, S. Li, Z. Wang, J. Liu, X. Wang, Semiconductor

heterojunction photocatalysts: design, construction, and photocatalytic performances, Chemical Society Reviews, 43 (2014) 5234-5244.

[51] H. Chen, C.E. Nanayakkara, V.H. Grassian, Titanium dioxide photocatalysis in atmospheric chemistry, Chemical Reviews, 112 (2012) 5919-5948.

[52] M. Pelaez, N.T. Nolan, S.C. Pillai, M.K. Seery, P. Falaras, A.G. Kontos, P.S. Dunlop, J.W. Hamilton, J.A. Byrne, K. O'shea, A review on the visible light active titanium dioxide photocatalysts for environmental applications, Applied Catalysis B: Environmental, 125 (2012) 331-349.

[53] S. Kalathil, M.M. Khan, S.A. Ansari, J. Lee, M.H. Cho, Band gap narrowing of titanium dioxide (TiO 2) nanocrystals by electrochemically active biofilms and their visible light activity, Nanoscale, 5 (2013) 6323-6326.

[54] S.A. Ansari, M.M. Khan, S. Kalathil, A. Nisar, J. Lee, M.H. Cho, Oxygen vacancy induced band gap narrowing of ZnO nanostructures by an electrochemically active biofilm, Nanoscale, 5 (2013) 9238-9246.

[55] H. Wang, A.L. Rogach, Hierarchical SnO2 nanostructures: recent advances in design, synthesis, and applications, Chemistry of Materials, 26 (2013) 123-133.

[56] M.M. Khan, S.A. Ansari, D. Pradhan, D.H. Han, J. Lee, M.H. Cho, Defect-induced band gap narrowed CeO2 nanostructures for visible light activities, Industrial & Engineering Chemistry Research, 53 (2014) 9754-9763.

[57] J. Yu, J. Low, W. Xiao, P. Zhou, M. Jaroniec, Enhanced photocatalytic CO2-reduction activity of anatase TiO2 by coexposed {001} and {101} facets, Journal of the American Chemical Society, 136 (2014) 8839-8842.

[58] H. Kato, K. Asakura, A. Kudo, Highly efficient water splitting into H2 and O2 over lanthanum-doped NaTaO3 photocatalysts with high crystallinity and surface

nanostructure, Journal of the American Chemical Society, 125 (2003) 3082-3089.

[59] K. Tanaka, M.F. Capule, T. Hisanaga, Effect of crystallinity of TiO2 on its photocatalytic action, Chemical Physics Letters, 187 (1991) 73-76.

[60] L. Xu, Y. Guo, Q. Liao, J. Zhang, D. Xu, Morphological control of ZnO nanostructures by electrodeposition, The Journal of Physical Chemistry B, 109 (2005) 13519-13522.

[61] S. Jiao, K. Zhang, S. Bai, H. Li, S. Gao, H. Li, J. Wang, Q. Yu, F. Guo, L. Zhao, Controlled morphology evolution of ZnO nanostructures in the electrochemical deposition: From the point of view of chloride ions, Electrochimica Acta, 111 (2013) 64-70.

[62] K. Wippermann, J. Schultze, R. Kessel, J. Penninger, The inhibition of zinc corrosion by bisaminotriazole and other triazole derivatives, Corrosion Science, 32 (1991) 205225-223230.

[63] L. Benea, E. Danaila, J.-P. Celis, Influence of electro-co-deposition parameters on nano-TiO2 inclusion into nickel matrix and properties characterization of nanocomposite coatings obtained, Materials Science and Engineering: A, 610 (2014) 106-115.

[64] M. Momenzadeh, S. Sanjabi, The effect of TiO2 nanoparticle codeposition on microstructure and corrosion resistance of electroless Ni P coating, Materials and Corrosion, 63 (2012) 614-619.

[65] S.T. Aruna, M. Muniprakash, V.K. William Grips, Effect of titania particles preparation on the properties of Ni–TiO2 electrodeposited composite coatings, Journal of Applied Electrochemistry, 43 (2013) 805-815.

[66] M.F. Morks, N.F. Fahim, A. Kobayashi, Microstructure, corrosion behavior, and microhardness of plasma-sprayed W–Ni composite coatings, Journal of Manufacturing

Processes, 10 (2008) 6-11.

[67] J.P. Davim, F. Mata, Chemical vapour deposition (CVD) diamond coated tools performance in machining of PEEK composites, Materials & Design, 29 (2008) 1568-1574.

[68] W. Henderer, F. Xu, Hybrid TiSiN, CrC/C PVD coatings applied to cutting tools, Surface and Coatings Technology, 215 (2013) 381-385.

[69] D. Thiemig, A. Bund, Characterization of electrodeposited Ni–TiO2 nanocomposite coatings, Surface and Coatings Technology, 202 (2008) 2976-2984.

[70] B.P. Neville, A. Rabiei, Composite metal foams processed through powder metallurgy, Materials & Design, 29 (2008) 388-396.

[71] L. Luo, J. Yao, J. Li, J. Yu, Preparation and characterization of sol–gel Al2O3/Ni–P composite coatings on carbon steel, Ceramics International, 35 (2009) 2741-2745.

[72] G. Parida, D. Chaira, M. Chopkar, A. Basu, Synthesis and characterization of Ni-TiO2 composite coatings by electro-co-deposition, Surface and Coatings Technology, 205 (2011) 4871-4879.

[73] L. Benea, F. Wenger, P. Ponthiaux, J.P. Celis, Tribocorrosion behaviour of Ni–SiC nano-structured composite coatings obtained by electrodeposition, Wear, 266 (2009) 398-405.

[74] L. Benea, Electrodeposition and tribocorrosion behaviour of ZrO2–Ni composite coatings, Journal of applied electrochemistry, 39 (2009) 1671.

[75] Y.-J. Xue, X.-Z. Jia, Y.-W. Zhou, W. Ma, J.-S. Li, Tribological performance of Ni–CeO2 composite coatings by electrodeposition, Surface and Coatings Technology, 200 (2006) 5677-5681.

[76] R.K. Saha, T.I. Khan, Effect of applied current on the electrodeposited Ni–Al2O3

composite coatings, Surface and Coatings Technology, 205 (2010) 890-895.

[77] A.C. Ciubotariu, L. Benea, M. Lakatos–Varsanyi, V. Dragan, Electrochemical impedance spectroscopy and corrosion behaviour of Al2O3–Ni nano composite coatings, Electrochimica Acta, 53 (2008) 4557-4563.

[78] M.A. Eltoum, A. Baraka, M. Saber, E.A. Hassan, Electrodeposition and Characterization of Nickel-Titania Nanocomposite Coatings from Gluconate Baths, International Journal Of Multidisciplinary Sciences And Engineering, 2 (2011).

[79] J.C. Wataha, Biocompatibility of dental casting alloys: a review, The Journal of prosthetic dentistry, 83 (2000) 223-234.

[80] A. Oyane, H.M. Kim, T. Furuya, T. Kokubo, T. Miyazaki, T. Nakamura, Preparation and assessment of revised simulated body fluids, Journal of biomedical materials research Part A, 65 (2003) 188-195.

[81] Y. Song, D. Shan, E. Han, Corrosion behaviors of electroless plating Ni–P coatings deposited on magnesium alloys in artificial sweat solution, Electrochimica Acta, 53 (2007) 2009-2015.

[82] Y. Wang, H. Zheng, Z. Li, K. Xie, Investigation of the interaction between Cu (acac) 2 and NH 4 Y in the preparation of chlorine-free CuY catalysts for the oxidative carbonylation of methanol to a fuel additive, RSC Advances, 5 (2015) 102323-102331.

[83] D. Esken, X. Zhang, O.I. Lebedev, F. Schröder, R.A. Fischer, Pd@ MOF-5: limitations of gas-phase infiltration and solution impregnation of [Zn4O (bdc) 3](MOF-5) with metal–organic palladium precursors for loading with Pd nanoparticles, Journal of Materials Chemistry, 19 (2009) 1314-1319.

[84] B.-H. Woo, M. Sone, A. Shibata, C. Ishiyama, K. Masuda, M. Yamagata, Y. Higo, Effects of Sc-CO2 catalyzation in metallization on polymer by electroless plating, Surface

and Coatings Technology, 203 (2009) 1971-1978.

[85] W.-T. Chiu, Y. Tahara, C.-Y. Chen, T.-F.M. Chang, T. Hashimoto, H. Kurosu, M. Sone, Fundamental Property Assessments of Biocompatible Silk–Pt Composite Prepared by Supercritical Carbon Dioxide Promoted Electroless Plating, Industrial & Engineering Chemistry Research, 56 (2017) 8864-8871.

[86] Y. Cheng, K. Yeung, Effects of electroless plating chemistry on the synthesis of palladium membranes, Journal of Membrane Science, 182 (2001) 195-203.

[87] C.R. BHATTACHARJEE, M.K. CHAUDHURI, New developments in the chemistry of metal-acetylacetonate complexes, Advances in Organometallics: Proceedings of the First Indo-Soviet Symposium on" Organometallic Chemistry" Held at Jaipur, Rajasthan, India, During March 7-11, 1988, Indian National Science Academy, 1989, pp. 64.

[88] L. Abrantes, J. Correia, On the Mechanism of Electroless Ni‐P Plating, Journal of the electrochemical society, 141 (1994) 2356-2360.

[89] W. Tang, K. Xu, P. Wang, X. Li, Surface roughness and resistivity of Au film on Si-(111) substrate, Microelectronic Engineering, 66 (2003) 445-450.

[90] V. Timoshevskii, Y. Ke, H. Guo, D. Gall, The influence of surface roughness on electrical conductance of thin Cu films: an ab initio study, Journal of Applied Physics, 103 (2008) 113705.

[91] P.-H. Lo, W.-T. Tsai, J.-T. Lee, M.-P. Hung, Role of phosphorus in the electrochemical behavior of electroless Ni-P alloys in 3.5 wt.% NaCl solutions, Surface and coatings Technology, 67 (1994) 27-34.

[92] C.J. Lin, K.C. Chen, J.L. He, The cavitation erosion behavior of electroless Ni–P–SiC composite coating, Wear, 261 (2006) 1390-1396.

[93] J.N. Balaraju, Kalavati, K.S. Rajam, Influence of particle size on the microstructure, hardness and corrosion resistance of electroless Ni–P–Al2O3 composite coatings, Surface and Coatings Technology, 200 (2006) 3933-3941.

[94] A. Bai, P.-Y. Chuang, C.-C. Hu, The corrosion behavior of Ni–P deposits with high phosphorous contents in brine media, Materials Chemistry and Physics, 82 (2003) 93-100.

[95] G.T. Vaughan, T.M. Florence, Platinum in the human diet, blood, hair and excreta, Science of The Total Environment, 111 (1992) 47-58.

[96] C.M. van den Berg, G.S. Jacinto, The determination of platinum in sea water by adsorptive cathodic stripping voltammetry, Analytica chimica acta, 211 (1988) 129-139.

[97] E.D. Goldberg, V. Hodge, P. Kay, M. Stallard, M. Koide, Some comparative marine chemistries of platinum and iridium, Applied Geochemistry, 1 (1986) 227-232.

[98] E.D. Goldberg, M. Koide, Understanding the marine chemistries of the platinum group metals, Marine chemistry, 30 (1990) 249-257.

[99] H. Vrubel, V.H.C. Verzenhassi, S. Nakagaki, F.S. Nunes, Catalytic reduction of hydrazine to ammonia by a high-oxidation state molybdenum complex, Inorganic Chemistry Communications, 11 (2008) 1040-1043.

[100] D.A.P. Tanaka, M.A.L. Tanco, S.-i. Niwa, Y. Wakui, F. Mizukami, T. Namba, T.M. Suzuki, Preparation of palladium and silver alloy membrane on a porous α-alumina tube via simultaneous electroless plating, Journal of Membrane Science, 247 (2005) 21-27.

[101] J.C. Wataha, Principles of biocompatibility for dental practitioners, The Journal of prosthetic dentistry, 86 (2001) 203-209.

[102] W. Platinum, Environmental health criteria 125, International Program on Chemical Safety, (1991).

[103] I. Iavicoli, B. Bocca, L. Fontana, S. Caimi, A. Bergamaschi, A. Alimonti, Distribution and elimination of palladium in rats after 90-day oral administration, Toxicology and industrial health, 26 (2010) 183-189.

[104] H. Koubu, Y. Hayashi, J. Fukushima, H. Takizawa, I. Narita, S. Yoshioka, Synthesis of Noble Metal-Doped Cu Nanoparticles by Ultrasonication, Materials Transactions, 54 (2013) 1496-1501.

[105] M. Tanabe, T.-F.M. Chang, T. Nagoshi, S.-T. Chung, W.-T. Tsai, H. Hosoda, T. Sato, M. Sone, Mechanical properties of Sn electrodeposited in supercritical CO 2 emulsions using micro-compression test, Microelectronic Engineering, 141 (2015) 219-222.

[106] T.-F.M. Chang, M. Sone, A. Shibata, C. Ishiyama, Y. Higo, Bright nickel film deposited by supercritical carbon dioxide emulsion using additive-free Watts bath, Electrochimica Acta, 55 (2010) 6469-6475.

[107] T.-F.M. Chang, T. Shimizu, C. Ishiyama, M. Sone, Effects of pressure on electroplating of copper using supercritical carbon dioxide emulsified electrolyte, Thin Solid Films, 529 (2013) 25-28.

[108] T.-F.M. Chang, T. Tasaki, C. Ishiyama, M. Sone, Defect-Free Nickel Micropillars Fabricated at a High Current Density by Application of a Supercritical Carbon Dioxide Emulsion, Industrial & Engineering Chemistry Research, 50 (2011) 8080-8085.

[109] D. Chaverri, A. Saenz, V. Castano, Grain size and electrical resistivity measurements on aluminum polycrystalline thin films, Materials Letters, 12 (1991) 344-348.

[110] B.R. Sankapal, H.B. Gajare, S.S. Karade, R.R. Salunkhe, D.P. Dubal, Zinc oxide encapsulated carbon nanotube thin films for energy storage applications, Electrochimica Acta, 192 (2016) 377-384.

[111] A. El Hichou, N. Stein, C. Boulanger, L. Johann, Structural and spectroscopic ellipsometry characterization for electrodeposited ZnO growth at different hydrogen peroxide concentration, Thin Solid Films, 518 (2010) 4150-4155.

[112] W.-H. Lin, T.-F.M. Chang, Y.-H. Lu, T. Sato, M. Sone, K.-H. Wei, Y.-J. Hsu, Supercritical CO2-Assisted Electrochemical Deposition of ZnO Mesocrystals for Practical Photoelectrochemical Applications, The Journal of Physical Chemistry C, 117 (2013) 25596-25603.

[113] T. Pauporté, D. Lincot, Hydrogen peroxide oxygen precursor for zinc oxide electrodeposition II—mechanistic aspects, Journal of Electroanalytical Chemistry, 517 (2001) 54-62.

[114] S.-W. Bian, I.A. Mudunkotuwa, T. Rupasinghe, V.H. Grassian, Aggregation and dissolution of 4 nm ZnO nanoparticles in aqueous environments: influence of pH, ionic strength, size, and adsorption of humic acid, Langmuir, 27 (2011) 6059-6068.

[115] R. Tena-Zaera, J. Elias, G. Wang, C. Lévy-Clément, Role of chloride ions on electrochemical deposition of ZnO nanowire arrays from O2 reduction, The Journal of Physical Chemistry C, 111 (2007) 16706-16711.

[116] A.G. Tekerlekopoulou, S. Pavlou, D.V. Vayenas, Removal of ammonium, iron and manganese from potable water in biofiltration units: a review, Journal of Chemical Technology and Biotechnology, 88 (2013) 751-773.

[117] H. Zeng, W. Cai, P. Liu, X. Xu, H. Zhou, C. Klingshirn, H. Kalt, ZnO-based hollow nanoparticles by selective etching: elimination and reconstruction of metal− semiconductor interface, improvement of blue emission and photocatalysis, ACS nano, 2 (2008) 1661-1670.

[118] N.s. Baik, G. Sakai, N. Miura, N. Yamazoe, Preparation of stabilized nanosized tin

oxide particles by hydrothermal treatment, Journal of the American Ceramic Society, 83 (2000) 2983-2987.

[119] G. Korotcenkov, B. Cho, The role of the grain size on thermal stability of nanostructured SnO2 and In2O3 metal oxides films aimed for gas sensor application, Progress in Crystal Growth, 58 (2012) 167-208.

[120] Z. Abdel Hamid, I.M. Ghayad, Characteristics of electrodeposition of Ni-polyethylene composite coatings, Materials Letters, 53 (2002) 238-243.

[121] C. Müller, M. Sarret, M. Benballa, ZnNi/SiC composites obtained from an alkaline bath, Surface and Coatings Technology, 162 (2003) 49-53.

[122] K. Krishnaveni, T.S.N. Sankara Narayanan, S.K. Seshadri, Electrodeposited Ni–B–Si3N4 composite coating: Preparation and evaluation of its characteristic properties, Journal of Alloys and Compounds, 466 (2008) 412-420.

[123] C.-W. Liao, H.-B. Lee, K.-H. Hou, S.-Y. Jian, C.-E. Lu, M.-D. Ger, Characterization of the Cr-C/Si3N4 Composite Coatings Electroplated from a Trivalent Chromium Bath, Electrochimica Acta, 209 (2016) 244-253.

[124] N. Guglielmi, Kinetics of the deposition of inert particles from electrolytic baths, Journal of the Electrochemical Society, 119 (1972) 1009-1012.

[125] J. Zahavi, J. Hazan, Electrodeposited nickel composites containing diamond particles, Plat. Surf. Finish., 70 (1983) 57-61.

[126] W.-H. Lee, S.-C. Tang, K.-C. Chung, Effects of direct current and pulse-plating on the co-deposition of nickel and nanometer diamond powder, Surface and Coatings Technology, 120 (1999) 607-611.

[127] W.-T. Chiu, C.-Y. Chen, T.-F.M. Chang, Y. Tahara, T. Hashimoto, H. Kurosu, M. Sone, Fabrication and Photocatalytic Performance of Au/ZnO Layered Structure on Silk

Textile for Flexible Device Applications, Electrochimica Acta, 253 (2017) 39-46.

[128] D.J. Blackwood, K.H.W. Seah, Electrochemical cathodic deposition of hydroxyapatite: Improvements in adhesion and crystallinity, Materials Science and Engineering: C, 29 (2009) 1233-1238.